



**UNIVERSITY OF BERGEN**

---

An Analysis of CO<sub>2</sub>, CH<sub>4</sub> and Mixed CO<sub>2</sub>-CH<sub>4</sub> Gas Hydrates:  
Experimental Phase Equilibria Measurements and  
Simulations with State-of-the-Art Software

---

Author:

*Ole Gilje Avaldsnes*

Supervisors:

*Professor Tanja Barth*

*Professor Per Fotland*

Faculty of Mathematics and Natural Sciences

Department of Chemistry

June 2014



## Abstract

The enormous amount of CH<sub>4</sub> trapped in gas hydrates has led to a growing focus on gas hydrates as a potential future energy source. One of the proposed methods for the production of CH<sub>4</sub> from these deposits, is to exchange the CH<sub>4</sub> molecules with CO<sub>2</sub> molecules. In this context, the determination of the phase equilibria of mixed CO<sub>2</sub>-CH<sub>4</sub> hydrates is essential.

In this thesis, the phase equilibria of mixed CO<sub>2</sub>-CH<sub>4</sub> hydrates has been investigated through simulations in PVTsim. The capability of simulating these systems to a significant degree of accuracy is a vital factor in potentially securing the practical application of the CO<sub>2</sub>-CH<sub>4</sub> exchange process. The predictability and accuracy of PVTsim is hence evaluated by means of agreement with published –and experimental data. It has been found that PVTsim is accurate in its prediction of the dissociation conditions of mixed CO<sub>2</sub>-CH<sub>4</sub> hydrates, while compositional predictions has been found to be less accurate.

From analysis of the phase equilibria data predicted by PVTsim for mixed CO<sub>2</sub>-CH<sub>4</sub> hydrates, it was observed that a sI/sII structural transition occurred for a range of CO<sub>2</sub>/CH<sub>4</sub> ratios when utilizing the SRK equation of state. Based upon subsequent analysis and literary evidence, it has been concluded that this structural transition is incorrect. This error is not observed for simulations performed utilizing the PR equation of state, where sI hydrate is predicted for all CO<sub>2</sub>/CH<sub>4</sub> ratios.

Data regarding the phase equilibria of CO<sub>2</sub>-, CH<sub>4</sub>-, and mixed CO<sub>2</sub>-CH<sub>4</sub> hydrates has additionally been acquired from experiments performed with the hydrate cell at the Department of Chemistry at the University of Bergen. The experimental data indicates that the updated hydrate cell serves as an accurate apparatus for the intended experimental purposes – where PVTsim serves as the tool for validation.

Data regarding the phase equilibria of mixed CO<sub>2</sub>-CH<sub>4</sub> hydrates at high isobaric conditions ( $\geq 7$  MPa) has been acquired from experiments performed at the Statoil's research laboratory in Bergen. Predicted dissociation conditions from PVTsim with regards to the experimental data acquired indicates that PVTsim predicts these conditions less accurately. This has been attributed to the possibility of the hydrate former being in a liquid phase.

## Acknowledgments

I am very grateful for the advice and exceptional supervision by Professor Tanja Barth during my two years as her student. She has always had a solution or idea for whatever experimental problem I encountered during my work. I would furthermore thank Professor Per Fotland for his encouragement and interest in my work, and for answering any questions I had in regards to gas hydrates. I am additionally very thankful for the opportunity to visit the PVT laboratory at Statoil Sandsli, which enabled me to complete the experiments necessary to conclude my thesis work.

Chief Engineer Olav-Audun Bjørklund is appreciated for his help with the new DAQ setup for the hydrate cell, and for his expertise related to electrical engineering of which I initially had little knowledge of. I would furthermore thank Senior Engineer Georgi Genov for his help with the stirring component connected to the hydrate cell. Chief Engineer Rachid Maad is appreciated for supplying the latest version of LabVIEW, and for giving me a brief introduction to graphical programming. Steinar Vatne is also appreciated for all his help with the mechanical problems encountered with the hydrate cell, and for the countless times I have borrowed various tools from his workshop. The help from Senior Engineer Per Arne Ormehaug and Associate Professor Geir Ersland in relation to experimental problems associated with the hydrate cell is additionally appreciated.

I would like to thank all my friends at the University of Bergen, who has made my five years as a student truly eventful. I would like to thank PhD candidate Magnus Fairhurst for several good discussions over coffee, both chemistry related and not. I would furthermore like to thank Magnus, Henrik, and Stian for helping me disassembling the hydrate cell whenever I needed a extra pair of hands.

I would furthermore thank my family for all the support and advice during my thesis work.

Finally, I am eternally grateful to Tina for her encouragement, and patience. Without her this thesis would be incredibly harder to complete.



## List of Abbreviations and Symbols

UiB	University of Bergen
sI	Hydrate structure I
sII	Hydrate structure II
sH	Hydrate structure H
MPa	Megapascal
K	Kelvin
°C	Degrees Celsius
P	Pressure (or phase)
T	Temperature
STP	Standard temperature and pressure
Q1	Lower quadruple point
Q2	Upper quadruple point
EOS	Equation of state
SRK	Soave-Redlich-Kwong
PR	Peng-Robinson
D T	Deviation in temperature
AD T	Absolute deviation in temperature
RD% P	Percent relative deviation in pressure
ARD% P	Absolute percent relative deviation in pressure
PT RTD	Platinum resistance thermometer
DAQ	Data acquisition
Rpm	Rotations per minute
LSD	Least significant digit
VI	Virtual instrument
GC	Gas chromatography
TCD	Thermal conductivity detector
FID	Flame ionization detector
VLE	Vapor-liquid equilibrium
V	Vapor or Volume
G	Gas
L	Liquid
H	Hydrate
I	Ice
F	Degrees of freedom
C	Component(s)
P	Phase(s)
$\Delta_c H$	Heat of combustion
$\Delta_f H^\circ$	Standard heat of formation
n	Mole(s)
$\rho$	density
R	Gas constant

Z	Compressibility factor
M	Molar mass
y	Vapor phase
z	Hydrate phase
x	Aqueous phase
CH <sub>4</sub>	Methane
CO <sub>2</sub>	Carbon dioxide
H <sub>2</sub> O	Water
C <sub>2</sub> H <sub>6</sub>	Ethane
C <sub>3</sub> H <sub>8</sub>	Propane
C <sub>4</sub> H <sub>10</sub>	Butane
C <sub>5</sub> H <sub>12</sub>	Pentane
N <sub>2</sub>	Nitrogen
H <sub>2</sub> S	Hydrogen sulphide
N-	Nitrogen compounds
S-	Sulphur compounds
NaCl	Sodium chloride
MEG	Monoethylene glycol
MeOH	Methanol

<b>ABSTRACT</b>	<b>I</b>
<b>ACKNOWLEDGMENTS</b>	<b>II</b>
<b>LIST OF ABBREVIATIONS AND SYMBOLS</b>	<b>III</b>
<b>CHAPTER 1: INTRODUCTION</b>	<b>1</b>
<b>1.1 Background and objective</b>	<b>1</b>
<b>1.2 Gas hydrates</b>	<b>3</b>
1.2.1 Molecular structure of hydrates	3
1.2.2 The guest molecule	4
1.2.3 Hydrate phase equilibria	6
1.2.4 Hydrate nucleation, growth and dissociation	8
<b>1.3 Gas hydrates in the petroleum industry</b>	<b>10</b>
1.3.1 Future energy outlook	10
1.3.2 In situ hydrates	12
1.3.3 Recovery methods	13
<b>1.4 Mixed hydrates of CH<sub>4</sub> and CO<sub>2</sub></b>	<b>14</b>
1.4.1 Previous research on mixed CO <sub>2</sub> -CH <sub>4</sub> hydrates	15
<b>1.5 Approach and overview</b>	<b>21</b>
<b>CHAPTER 2: METHODS</b>	<b>22</b>
<b>2.1 PVTsim</b>	<b>22</b>
2.1.1 Equations of state and hydrate modelling	22
2.1.2 Flash calculations in PVTsim	23
2.2.3 Hydrate flash calculations in PVTsim	24
2.2.4 Accuracy of PVTsim predictions	25
2.2.5 Compositional predictions by PVTsim	27
<b>2.2 Ternary plots</b>	<b>29</b>
2.2.1 Ternary phase diagrams	30
2.2.1 PVTsim open structure and ternary phase diagrams	32
<b>CHAPTER 3: EXPERIMENTAL</b>	<b>33</b>

<b>3.1 Chemicals and fluids</b>	<b>33</b>
<b>3.2 Experimental setup</b>	<b>33</b>
3.2.1 The cooling incubator	34
3.2.2 Hydrate cell	35
3.2.3 The rotating stirrer	36
3.2.4 Pressure and temperature sensors	38
<b>3.3 Data acquisition and LabVIEW</b>	<b>39</b>
<b>3.4 Gas chromatography</b>	<b>42</b>
<b>3.5 Experimental procedures for the hydrate cell at UiB</b>	<b>44</b>
<b>3.6 Description of experiments performed at Statoil</b>	<b>47</b>
<b>CHAPTER 4: RESULTS</b>	<b>48</b>
<b>4.1. PVTsim simulations of the CO<sub>2</sub>-CH<sub>4</sub>-H<sub>2</sub>O system</b>	<b>48</b>
4.1.1 Ternary phase diagrams	48
4.1.2 PVTsim predictions compared with data from Belandria et al. (2011).	55
<b>4.2 Accuracy of PVTsim predictions</b>	<b>60</b>
4.2.1 Simple CO <sub>2</sub> and CH <sub>4</sub> hydrates	60
4.2.2 Mixed CO <sub>2</sub> -CH <sub>4</sub> hydrates	61
<b>4.3 Experiments performed at the University of Bergen</b>	<b>63</b>
4.3.1 Simple CO <sub>2</sub> hydrate experiments	65
4.3.2 Simple CH <sub>4</sub> hydrate experiments	68
4.3.3 Mixed CO <sub>2</sub> -CH <sub>4</sub> hydrate experiments	72
<b>4.4. Experiments performed at Statoil</b>	<b>77</b>
<b>CHAPTER 5: DISCUSSION</b>	<b>81</b>
<b>5.1 PVTsim simulations of the CO<sub>2</sub>-CH<sub>4</sub>-H<sub>2</sub>O system</b>	<b>81</b>
5.1.1 Previous research on mixed CO <sub>2</sub> -CH <sub>4</sub> hydrate structures	81
5.1.2 Ternary phase diagrams	82
5.1.3 PVTsim predictions compared with data from Belandria et al. (2011).	84
<b>5.2 Accuracy of PVTsim predictions</b>	<b>86</b>

5.3 Experiments performed at the University of Bergen	90
5.4 Experiments performed at Statoil	96
<b>CHAPTER 6: CONCLUSION AND SUGGESTIONS FOR FURTHER WORK</b>	<b>98</b>
6.1 Conclusion	98
6.2: Suggestions for further work	99
<b>APPENDIX A: RESULTS</b>	<b>101</b>
Appendix A.1: PVTsim simulations	102
Appendix A.2: Accuracy of PVTsim predictions	112
Appendix A.3: Unsucessful hydrate experiments	116
<b>APPENDIX B: EXPERIMENTAL PROCEDURES</b>	<b>119</b>
<b>B.1 The cooling incubator</b>	<b>120</b>
B.1.1 Basic operations	121
B.1.2 Cooling and heating	122
<b>B.2 The stirring device.</b>	<b>123</b>
B.2.1 Troubleshooting	125
<b>B.3 LabVIEW VIs</b>	<b>127</b>
B.3.1 The calibration VI	128
B.3.1 The logging VI	129
B.3.3 Summarized procedure	132
<b>REFERENCES</b>	<b>133</b>

# CHAPTER 1: INTRODUCTION

## 1.1 Background and objective

There is an immense amount of gas trapped in gas hydrate deposits globally. The estimates vary but it is hypothesized that the amount of carbon in hydrates is twice the size of the carbon equivalent of all conventional fossil fuel deposits in the world [1]. The global energy demand is expected to increase by one-third from 2011 to 2035 – with an expected 48% increase in natural gas consumption [2]. Due to the predicted increase in global energy consumption, gas hydrates have attained increased attention in the last decade with respect to being a potential future energy source [3].

Several methods have been proposed in regards to gas recovery from hydrates. This includes thermal stimulation, chemical/inhibitor injection and depressurization, where the latter is the most promising [4]. A more recent recovery method is based on exchanging the CH<sub>4</sub> molecules in hydrates with CO<sub>2</sub> molecules, which was initially proposed and patented by Ebinuma (1993) [5]. This recovery method has subsequently gained increased attention in the last decade where the recovery of CH<sub>4</sub> and the following CO<sub>2</sub> sequestration may ultimately result in a carbon neutral energy source. There has been extensive research on the CO<sub>2</sub>-CH<sub>4</sub> exchange process at the Department of Physics and Technology at the University of Bergen. This research led to a cooperation with ConocoPhillips, where the method was field tested at the Ignik Sikuma field in Alaska, USA [3, 6].

Gas hydrates have additionally been extensively researched at the Department of Chemistry at the University of Bergen in regards to flow assurance problems related to their formation. This includes the HYPERION project (2005-2009), which was an interdisciplinary research project that included the Department of Chemistry, the Department of Physics and Technology and StatoilHydro ASA [7]. As a part of the project, StatoilHydro ASA donated a hydrate cell for examining thermodynamic and kinetic properties of gas hydrates. The thesis by Talatori (2009) submitted as a part of the research project included experiments performed with the hydrate cell [8]. Two additional PhD theses, submitted by Vaular (2011) and Corak (2011), also included experiments performed with the same hydrate cell [9, 10].

In this work, the hydrate cell has been extensively updated by incorporating a new data acquisition system, new components and parts. New procedures for hydrate experiments based on this setup have also been proposed.

The concept and mechanism of the CO<sub>2</sub>-CH<sub>4</sub> exchange process have been extensively researched at the University of Bergen, and globally by various research groups [3]. The phase equilibria of hydrates formed from a CO<sub>2</sub>-CH<sub>4</sub> gas mixture have however received less attention. A quantitative understanding of the phase equilibria of mixed CO<sub>2</sub>-CH<sub>4</sub> hydrates is necessary as the hydrates formed in the exchange process essentially are mixed CO<sub>2</sub>-CH<sub>4</sub> hydrates.

The experimental objective for this thesis is consequently an analysis of the phase equilibria of mixed CO<sub>2</sub>-CH<sub>4</sub> hydrates. Phase equilibria data for simple CO<sub>2</sub>-, CH<sub>4</sub>-, and mixed CO<sub>2</sub>-CH<sub>4</sub> hydrates acquired from experiments performed with the hydrate cell at UiB are presented in this thesis. Results from experiments performed at the PVT laboratory at Statoil is additionally presented. Previous published experimental data on mixed CO<sub>2</sub>-CH<sub>4</sub> hydrates have been thoroughly reviewed, and is discussed.

The phase equilibria of mixed CO<sub>2</sub>-CH<sub>4</sub> hydrates have additionally been investigated by means of thermodynamic simulations performed in modelling software PVTsim, developed by Calsep [11]. The accuracy of PVTsim predictions has been thoroughly investigated through simulations with respect to experimental dissociation conditions from the literature, and determined dissociation conditions for the experiments performed at UiB and Statoil.

## 1.2 Gas hydrates

Gas hydrates are clathrate compounds where the host lattice is composed of hydrogen bonded H<sub>2</sub>O molecules. The host lattice encloses molecules, generally referred to as “guest molecules”, during formation. Clathrate hydrates visually resemble the solid form of water - ice, although they form at higher temperatures and have different physiological properties. Gas hydrates form where water and specific gases are present at low-temperature and high-pressure conditions [4].

### 1.2.1 Molecular structure of hydrates

The polyhedral structures that constitute the hydrate crystal structure are composed of pentagonal, hexagonal and square face structures of H<sub>2</sub>O molecules. These faces connect through side sharing, and enclose a suitable guest molecule. The space in which the guest molecules are trapped is called a cavity, which is designated by  $n_i m_i$ .  $n_i$  refers to the number of edges in face type  $i$ , whereas  $m_i$  refers to the number of faces [4].

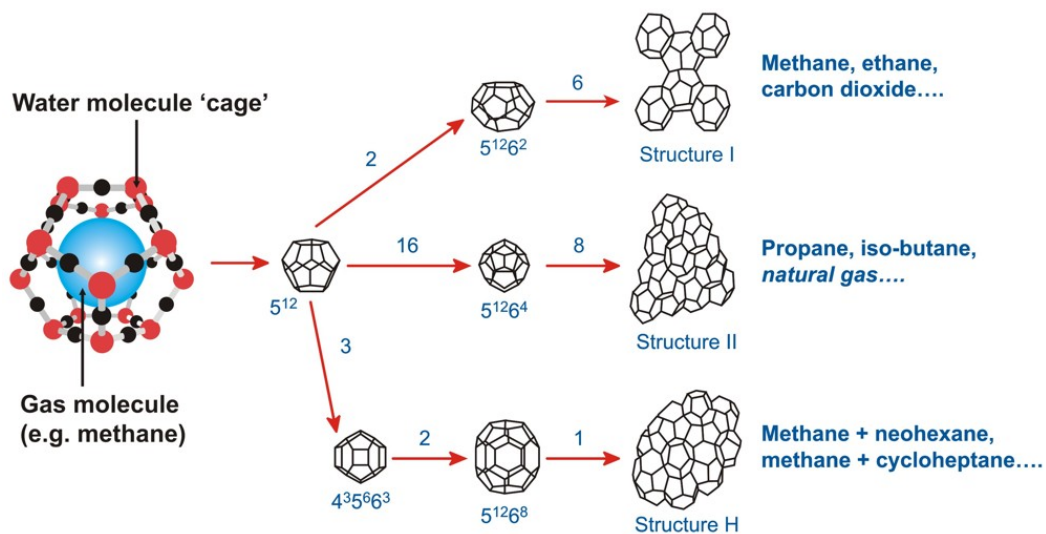


Figure 1.1: The three common hydrate structures that form with natural gas components as guest molecules. Example: Two  $5^{12}$  and six  $5^{12}6^2$  cavities form a unit cell whose repetition in three dimensions constitutes structure I. The other structures follow the same procedure, although with different cavities as constituents. Figure from [12].



All three structures in Fig. 1.1 are found in nature, with structure I (sI) and structure II (sII) being most abundant [13]. At normal to high pressures each hydrate cage is generally limited to one guest molecule, at very high pressures (1000 MPa) multiple guest molecules may however occupy the hydrate cages [4]. Table 1.1 lists the geometrical properties of the three common hydrate structures.

Table 1.1: The geometrical properties of the three common hydrate structures. The average cavity radius is the distance from the centre of a cavity to the enclosing H<sub>2</sub>O molecules. From [4].

Hydrate crystal structure: Cavity:	<u>I</u>		<u>II</u>		<u>H</u>		
	Small	Large	Small	Large	Small	Medium	Large
Description	5 <sup>12</sup>	5 <sup>12</sup> 6 <sup>2</sup>	5 <sup>12</sup>	5 <sup>12</sup> 6 <sup>4</sup>	5 <sup>12</sup>	4 <sup>3</sup> 5 <sup>6</sup> 6 <sup>3</sup>	5 <sup>12</sup> 6 <sup>8</sup>
# Cavities per unit cell	2	6	16	8	3	2	1
Average cavity radius (Å)	3.95	4.33	3.91	4.73	3.94	4.04	5.79
# of H <sub>2</sub> O molecules per cavity	20	24	20	28	20	20	36

### 1.2.2 The guest molecule

The sum of the repulsive and attractive interactions between the guest molecule and the hydrogen bonded H<sub>2</sub>O molecules stabilizes the hydrate cavities, i.e., the hydrate cavities are essentially stabilized by Van der Waals forces, and there are no chemical bonds between the guest molecule and the surrounding H<sub>2</sub>O molecules [4].

The chemical nature, size and shape are the main factors which influences hydrate properties. Guest molecule size will influence both structure and equilibrium pressure [4]. The shape of the guest molecule is primarily important for structure H hydrate (sH) due to the larger asymmetric cage, while it is less important for sI and sII hydrates [4].

Table 1.2: Ratio of molecular diameter to cavity diameter (guest molecule/cavity) for CH<sub>4</sub>- and CO<sub>2</sub> molecules. From [4].

Molecule	Diameter* (Å)	Structure I		Structure II	
		5 <sup>12</sup>	5 <sup>12</sup> 6 <sup>2</sup>	5 <sup>12</sup>	5 <sup>12</sup> 6 <sup>4</sup>
CH <sub>4</sub>	4.36	0.855ζ	0.744ζ	0.868	0.655
CO <sub>2</sub>	5.12	1.00ζ	0.834ζ	1.02	0.769

ζ Cavity occupied by simple hydrate former.

\*The cavity diameter is calculated from the average cavity radius in Table 1.1 by initially subtracting the van der Waals diameter of the H<sub>2</sub>O molecule, which is 2.8 Å [4, 14].

$\text{CO}_2$  and  $\text{CH}_4$  are both simple hydrate formers – meaning that they may form hydrates where they alone appear as the guest specie. As a simple hydrate former,  $\text{CH}_4$  molecules occupies and stabilizes both the small and large cavities of sI [4].  $\text{CO}_2$  molecules occupies all the large cavities in sI as a simple hydrate former, while the smaller cavities have a variable cavity-filling dependent on the synthesis conditions [15]. Natural gas mixtures generally form sII hydrates due to the presence of larger molecules such as  $\text{C}_2\text{H}_6$  and  $\text{C}_3\text{H}_8$ , which only fit into the large cavity in sII [4].

The ideal hydration number is the theoretically minimum number of  $\text{H}_2\text{O}$  molecules per guest molecule. For simple hydrates assuming full occupation of all cavities in sI, the ideal hydration number is  $G \cdot 5.75\text{H}_2\text{O}$ . For sII the hydration number is  $G \cdot 5.67\text{H}_2\text{O}$  assuming full occupation of all cavities. In reality it is impossible to obtain full occupation of the cavities, and clathrate hydrates are consequently nonstoichiometric [4]. Circone et al. (2003) examined the dissociation behaviour of simple sI  $\text{CO}_2$  hydrates. Three stoichiometric values of 5.59, 5.64, and 5.74  $\text{H}_2\text{O}$  molecules per  $\text{CO}_2$  molecule were reported, with an uncertainty of  $\pm 0.15$ . Two additional stoichiometric values of 5.7 and 5.6 were reported, based on a mass uptake method [15]. Circone et al. (2005) additionally examined the stoichiometry of sI  $\text{CH}_4$  hydrates and reported a hydration number of  $G \cdot (5.81 - 6.10) \text{H}_2\text{O}$ , with an average of  $G \cdot 5.99 \text{H}_2\text{O}$  [16].

Mixed hydrates are hydrates that consist of more than one guest molecule component. Gas hydrates found in nature are usually mixed hydrates, this is due to various amounts of other hydrate formers existing in addition to  $\text{CH}_4$  in natural gas [4]. Figure 1.2 illustrates some of the cavities of the binary  $\text{CH}_4\text{-C}_3\text{H}_8$  sII hydrate. In this case the  $\text{CH}_4$  molecules occupies the smaller cavities, while the  $\text{C}_3\text{H}_8$  molecules occupies the large.

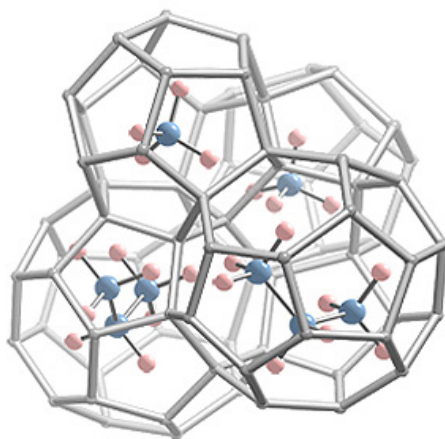


Figure 1.2:  $\text{CH}_4\text{-C}_3\text{H}_8$  cavities. From [17].

### 1.2.3 Hydrate phase equilibria

Hydrate phase diagrams differ considerably from typical hydrocarbon phase diagrams due to the amount of hydrogen bonding, and the additional hydrate phase present. As with conventional phase diagrams, Gibbs' phase rule also applies to hydrate phase diagrams [4]:

$$F = C - P + 2 \quad (1.1)$$

Where  $F$  is the degrees of freedom, i.e., the number of intensive variables that defines the system.  $C$  is the number of components in the system, and  $P$  is the number of phases in the system. 2 degrees of freedom are additionally included in the expression for pressure and temperature [4, 18]. For a PT (pressure-temperature) diagram of a two-component system, e.g.  $\text{CH}_4\text{-H}_2\text{O}$  or  $\text{CO}_2\text{-H}_2\text{O}$ , two phases are represented as an area, three phases are represented as a line, and four phases are represented as a point. This is illustrated in the phase diagram below.

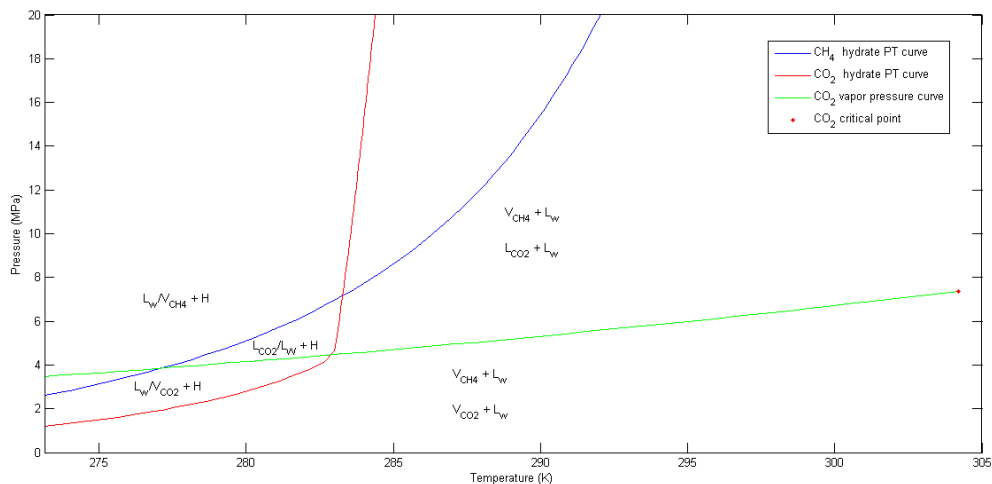


Figure 1.3: Hydrate PT curves for  $\text{CO}_2$  (red) and  $\text{CH}_4$  (blue) predicted by PVTsim [11]. The green curve is the vapor pressure curve for  $\text{CO}_2$ , where the red point is the critical point.  $V$  = vapor,  $L$  = liquid and  $H$  = hydrate. The “excess” phase in addition to hydrates inside the hydrate stability region is dependent on the amount of water present, hence the backslash between  $L$  and  $V$  phases.

The hydrate-forming region is to the left of the hydrate PT curves in Fig. 1.3. The blue and red lines are three-phase lines where liquid water, vapor and hydrates are in equilibrium ( $L_w\text{-H-V}$  line). By crossing the  $L_w\text{-H-V}$  line, hydrates may form from vapor and water. At pressures higher than the conditions where the  $\text{CO}_2$  vapor pressure curve intersects with the  $\text{CO}_2$  hydrate PT curve,  $\text{CO}_2$  hydrates may however form from liquid  $\text{CO}_2$ .

The almost vertical red line is consequently a three-phase line where liquid water, hydrates and liquid CO<sub>2</sub> are in equilibrium (L<sub>w</sub>-H-L<sub>CO2</sub>). At the point where the CO<sub>2</sub> vapor pressure curve intersects with the CO<sub>2</sub> hydrate PT curve, there are four phases in equilibrium (L<sub>w</sub>-H-V-L<sub>CO2</sub>). This is the upper quadruple point (Q<sub>2</sub>) for CO<sub>2</sub> hydrate. The CH<sub>4</sub> hydrate PT curve does not have an upper quadruple point, as the temperature at the critical point for CH<sub>4</sub> is below the hydrate forming region [4] - at 190.6 K and 4.6 MPa [11]. Lower quadruple points (Q<sub>1</sub>) where again four phases are in equilibrium (I-L<sub>w</sub>-H-V, where I = Ice), are not included in Fig. 1.3 as the experiments performed in this thesis are at temperatures above the freezing point of water.

The PT curves in Fig. 1.3 are products of simulations with pure water, consistent with the experiments performed in this thesis. If ionic compounds were dissolved in the water phase the PT curves would be displaced to the left in Fig. 1.3, i.e., lower temperatures would be required to form hydrates. This is due to the columbic force existing between water and salt ions, which competes with potential hydrogen bonds in the hydrate structure, and hinders hydrate formation. Electrolytes, alcohols and glycols are examples of so called thermodynamic inhibitors. Alcohols and glycols interact in hydrogen bonding with H<sub>2</sub>O molecules, which hinders the ordering of hydrogen bonded H<sub>2</sub>O molecules in hydrate structures. These inhibitors are utilized to prevent hydrate formation in oil and gas pipelines, i.e., flow assurance problems [19, 20].

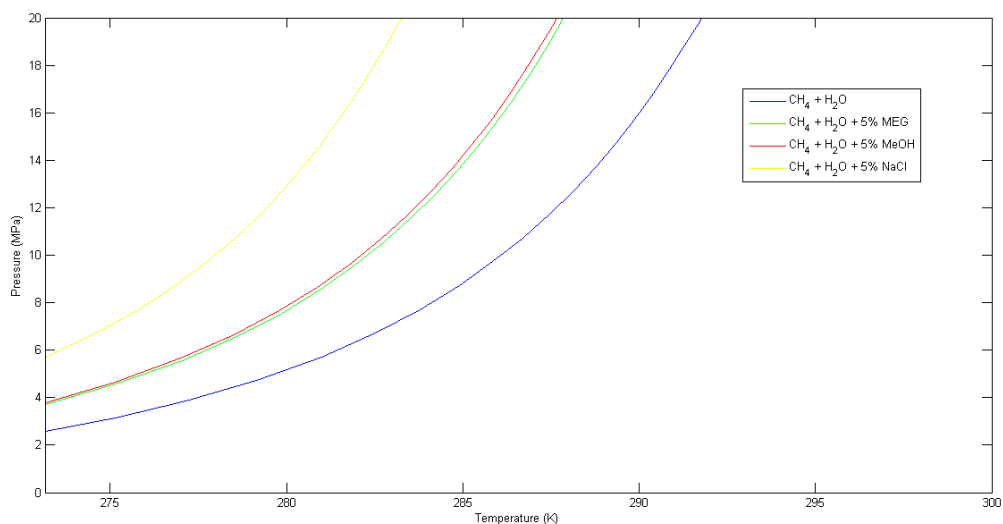


Figure 1.4: Hydrate PT curves for CH<sub>4</sub> with pure water and various thermodynamic inhibitors. Predicted by PVTsim [11]. The thermodynamic inhibitors essentially displace the PT curve of CH<sub>4</sub> with pure water to the left in the figure.

### 1.2.4 Hydrate nucleation, growth and dissociation

The time-dependent phenomena of hydrate nucleation, growth and dissociation are considerably harder to determine than the time-independent phenomena related to hydrate structures and phase behaviour [4].

A brief explanation of the kinetic phenomena related to hydrates is provided below with an example. For an in-depth explanation of the main theories proposed regarding hydrate nucleation the reader is referred to the collective works by Sloan and Koh (2008) [4].

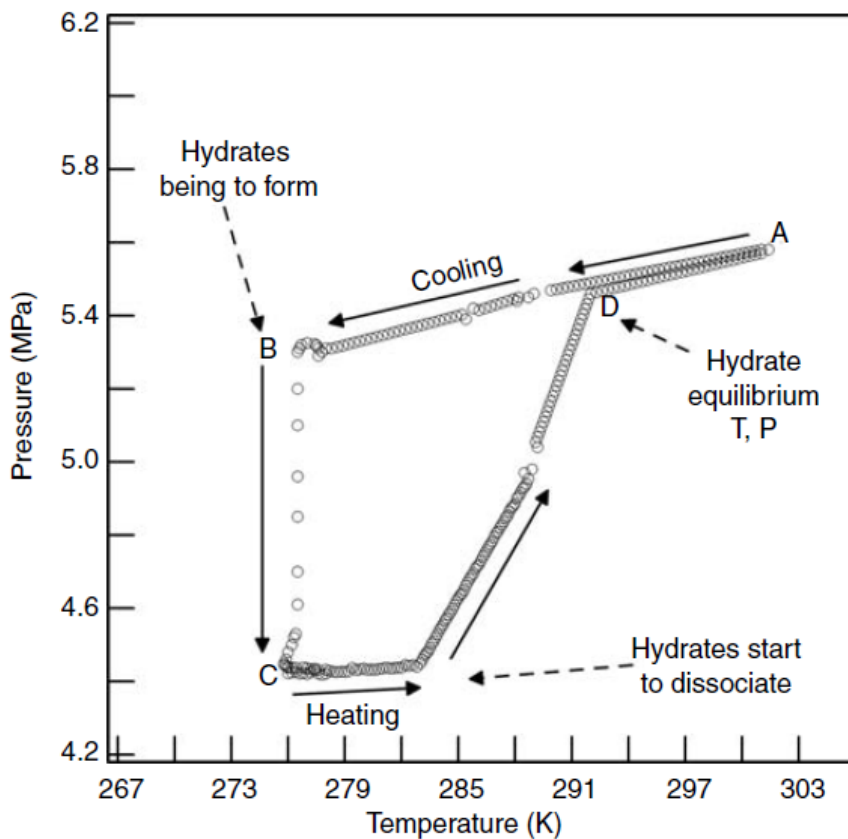


Figure 1.5: A PT-trace of a hydrate experiment cycle. The experiment is performed in an agitated autoclave cell with a constant inner volume. From [4].

In Figure 1.5 the system initially consists of water and gas (A). The pressure decreases during cooling due to gas contraction and increased gas solubility. Due to metastability hydrates do not instantaneously form at equilibrium conditions (D). Metastability refers to a semi-stable state that is less stable than the systems most stable state. Metastability is observed in hydrate systems during the induction period, which is the time period from A to B [4].

The induction period is the period before a detectable amount of gas is consumed. The induction time is characterized by hydrate nucleation, and hydrate nucleation is thought to be a stochastic phenomenon. Nucleation refers to the phenomena where hydrate nuclei develop and disperse in an effort to achieve critical size. Spontaneous growth then follows [4]. A system which has agitation, e.g. through mechanical stirring, has a shorter induction time as agitation induces nucleation in metastable solutions [21]. Previous experiments with simple hydrates formed from CH<sub>4</sub> and CO<sub>2</sub> indicate that nucleation and successive growth commonly occurs at the water-vapor interface for these hydrate formers. This consequently implies that hydrate nucleation is a heterogeneous nucleation process [4].

The following acute steepness in the curve after nucleation, i.e. stable hydrate growth observed in Fig. 1.5 from B to C, is an exothermic process that is primarily controlled by heat- and mass-transfer effects [4]. Hydrate dissociation is however endothermic, i.e., heat has to be supplied to break the hydrogen bonds in the hydrate structures, and the van der Waals forces between gas and water molecules [4]. Hydrate dissociation is illustrated in Fig 1.5 as the period from C to D. Dissociation is rapid compared to hydrate nucleation as entropy favours gas and liquid phases over solid hydrate [4].

The point marked as D in Fig. 1.5 is referred to as the hydrate equilibrium temperature and pressure by Sloan and Koh (2008) [4]. The temperature and pressure at this point are the values reported as the equilibrium conditions for a specific hydrate former. It may however be more appropriately referred to as the hydrate dissociation temperature and pressure, as the temperature and pressure conditions reported corresponds to where the last hydrate crystal melts [4].

### **1.3 Gas hydrates in the petroleum industry**

In 1934 Hammerschmidt discovered that gas hydrates formed plugs in gas transmission pipelines [19]. The discovery prompted an increase in gas hydrate research, specifically on how to prevent their formation. The research led to the development of the thermodynamic inhibitors previously mentioned, and various calculation methods to determine the hydrate formation conditions of oil and natural gas mixtures. This is particularly important for oil and natural gas fields in harsh environments at low temperature and high pressure conditions, where hydrates are stable. Subsequent research has led to the discovery of low-dosage-hydrate-inhibitors (LDHIs), such as antiagglomerants (AA) and kinetic inhibitors (KI) [4, 19].

#### **1.3.1 Future energy outlook**

Fossil fuels are a finite energy source, and production of conventional fossil fuels will eventually reach a peak. New methods to increase recovery, technological breakthroughs with shale gas and heavy oil/bitumen, as well as the significant volumes of conventional fossil fuels still in place, implies that fossil fuels will remain a dominant energy source for years to come. The global demand for energy is predicted to increase in the future as a consequence of population growth and a higher standard of living energy [2]. As a result of increased demand the petroleum industry and researchers are turning their attention to unconventional fossil fuels, where shale gas production in the US during the last decade is a prime example. Gas hydrates is another unconventional fossil fuel, which in recent years have gained increased attention as a potential future energy source [3].

Combustion of coal is the largest source for electricity production globally, with natural gas in second place [2]. Concerns regarding the environmental impact of emissions from coal combustion are frequently used as an argument for increased electricity production from natural gas. A discussion on the global energy future however needs to consider several factors, with economical and environmental factors being equally considered.

Natural gas contains mostly  $\text{CH}_4$ , with a lesser amount of other hydrocarbons ( $\text{C}_2\text{H}_6$ ,  $\text{C}_3\text{H}_8$ ,  $\text{C}_4\text{H}_{10}$ ,  $\text{C}_5\text{H}_{12}$ ), and trace amounts of  $\text{N}_2$ ,  $\text{CO}_2$  and  $\text{H}_2\text{S}$  [22]. The composition of coal varies widely, but it generally has high carbon content. Coal also contains various N- and S-containing compounds, which results in the release of  $\text{NO}_x$ , and  $\text{SO}_x$  during combustion. Coal combustion additionally generates particulates that can result in smog, or layers of smoke over densely populated areas [23].

The combustion reactions of coal and CH<sub>4</sub> is discussed in the following paragraph for comparisons purposes, as CH<sub>4</sub> is the most frequent guest molecule found in gas hydrates. Coal is here modelled as a pure carbon compound.

The combustion of CH<sub>4</sub> is illustrated with Eq.(1.6), and the combustion of coal is illustrated with Eq.(1.7). The heat of combustion ( $\Delta_c H$ ) value for CH<sub>4</sub> is from Ellis (1984) at 298 K and 0.53 MPa [24]. The heat of combustion ( $\Delta_c H$ ) value for coal (C (s)) has been calculated from the standard heat of formation value ( $\Delta_f H^\circ$ ) for CO<sub>2</sub> (g) at -393.5 kJ/mol [24], with the assumption that  $\Delta_f H^\circ = 0$  for C(s).



From Eq.(1.6) and Eq.(1.7) it is evident that CH<sub>4</sub> is essentially a much more effective fuel as it produces significantly less CO<sub>2</sub> per unit of energy compared to coal.



### 1.3.2 In situ hydrates

Gas hydrates have a high probability of occurrence in locations where natural gas and water are present in low temperature and high pressure conditions. Most hydrate deposits are found in oceanic environments at depths between 300-800 m, while a lesser amount is located in permafrost areas [4]. Hydrates formed from thermogenic gas are relatively rare compared to hydrates formed from biogenic gas [25].

The geometry of the clathrate hydrate structures limits the amount of gas that the structure can accommodate. By considering only CH<sub>4</sub> as the guest molecule, 1 m<sup>3</sup> saturated sI hydrate may contain as much as 164 m<sup>3</sup> CH<sub>4</sub> at STP conditions [26]. In addition to the high energy density, the energy required to dissociate hydrates is less than 15% of the possible recovered energy [4]. Estimates of total amount of hydrated gas in global deposits have decreased during the years due to increased insight into the field. All estimates to date are however significantly higher than the estimate of the conventional gas reserve by Radler (2000) at  $0.15 \cdot 10^{15} \text{ m}^3 \text{ CH}_4$  (STP) [4]. The most comprehensive estimate to date is from Klauda and Sandler (2005) at  $120 \cdot 10^{16} \text{ m}^3 \text{ CH}_4$  (STP), which includes very dispersed and deep hydrate deposits. This is reduced to  $4.4 \cdot 10^{16} \text{ m}^3 \text{ CH}_4$  if only continental hydrates are assessed [4].

The gas hydrates resource pyramid below illustrates the magnitude of hydrated gas separated into their depositional environments. The peak of the pyramid (artic hydrates) illustrates the amount of hydrated gas that is least difficult to potentially recover as a resource, whereas the base section is the most technically challenging to recover. The gas hydrates resource pyramid may also be compared to the non-gas-hydrate resource pyramid (conventional resources) to the right in the figure.

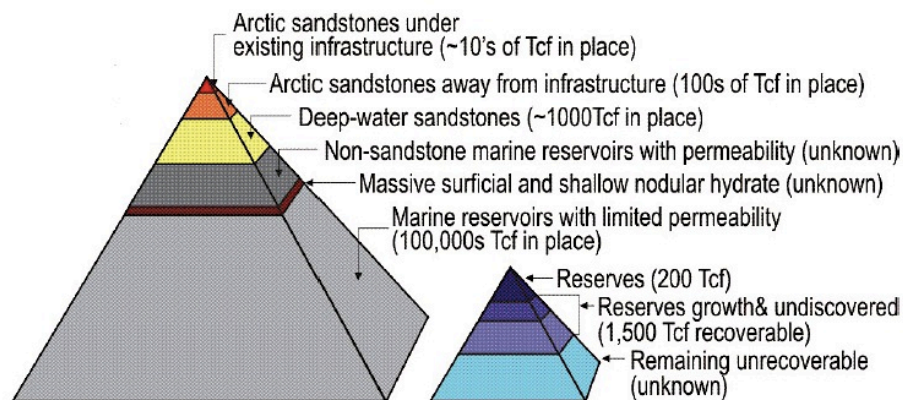


Figure 1.6: The gas hydrate resource pyramid. Tcf = trillion cubic feet, where  $1 \text{ Tcf} \approx 28 \cdot 10^{12} \text{ m}^3$ . From [27].

### 1.3.3 Recovery methods

The three primary gas recovery methods for hydrates are depressurization, inhibitor injection, and thermal injection [4]. The thermal injection method in combination with depressurization was successfully utilized in a 3-day field test at the Mallik field in Alaska, USA [25]. The Messoyakha natural gas field in Siberia is additionally often cited as an example of natural gas production from hydrates. There is however questionable evidence in regards to the contribution of gas from hydrates during production [25]. The first and only offshore hydrate production test was performed in March 2013 in the eastern Nankai Trough off Japan, where the recovery method was depressurization. 120.000 m<sup>3</sup> CH<sub>4</sub> was successfully produced from the subsurface during 6 days [28]. Concerns regarding these three recovery methods are water and sand production, and loss of subsurface stability due to the dissociation of solid hydrates [3, 29, 30].

A more recent method designed for CH<sub>4</sub> recovery from hydrates is based on a CO<sub>2</sub>-CH<sub>4</sub> exchange process [3]. CH<sub>4</sub> and CO<sub>2</sub> both form sl hydrates, but with different formation conditions. In the phase diagram in Fig. 1.3 there is a zone between the two three-phase lines where CO<sub>2</sub> hydrates are stable and CH<sub>4</sub> hydrates consequently dissociates [31]. Additionally, the enthalpy of formation for CO<sub>2</sub> hydrates at -57.98 kJ/mol is larger in magnitude than the enthalpy of dissociation for CH<sub>4</sub> hydrates at 54.49 kJ/mol [31]. The exothermic heat released during CO<sub>2</sub> hydrate formation is thus thought to be sufficient to dissociate CH<sub>4</sub> hydrates. Finally, it has been established through experiments that CO<sub>2</sub> is the preferential guest molecule in the hydrate phase [31]. The concerns associated with the “traditional” recovery methods is circumvented with this exchange process, as solid hydrates remains after the exchange process [30].

The exchange process is well documented in the literature, where several research groups have studied the process both in bulk and in porous media [3]. In 2012 the method was tested in the Ignik Sikumi field in Alaska, in a joint cooperative project with U.S. Department of Energy, ConocoPhillips, JOGMEC, and UiB. A mixture of CO<sub>2</sub> and N<sub>2</sub> was injected into the hydrate reservoir, and depressurization was subsequently utilized to extract dissociated CH<sub>4</sub> from the formation [3, 6]. A limitation with this method is that natural hydrate reservoirs generally contains excess water in addition to hydrates. There is consequently a risk of CO<sub>2</sub> hydrates being formed during injection, which may reduce reservoir permeability [3]. The rate of the CO<sub>2</sub>-CH<sub>4</sub> exchange has additionally been stated as very slow [32].

It should be noted that due to the difference in molecular diameter, and cavity preference of the  $\text{CH}_4$  and  $\text{CO}_2$  molecule, it is impossible for a full replacement scenario with an injection of pure  $\text{CO}_2$ : Lee et al. (2003) reported a  $\text{CH}_4$  recovery of 64% with a concentration of approximately 100%  $\text{CO}_2$  in the injection gas [33]. Ota et al. (2005) reported a similar number, with  $\text{CO}_2$  being injected in liquid form [34].

#### 1.4 Mixed hydrates of $\text{CH}_4$ and $\text{CO}_2$

There is a limited amount of research on mixed  $\text{CH}_4$ - $\text{CO}_2$  hydrates compared to the  $\text{CO}_2$ - $\text{CH}_4$  exchange phenomena. In a potential continuous  $\text{CH}_4$ - $\text{CO}_2$  exchange process, an insight on the phase equilibria for mixed  $\text{CH}_4$ - $\text{CO}_2$  hydrates is invaluable.

Considering a recovery situation such as the Ignik Sikumi field,  $\text{CO}_2$  is injected into the hydrate formation through the wellbore. As Fig. 1.7 illustrates, the  $\text{CO}_2$  concentration is highest near the wellbore (injection point), while further inwards in the reservoir the  $\text{CO}_2$  concentrations decreases. The exchange process may consequently be thought of as a gradient where recovery is highest near the wellbore, while the exchange diminishes further inwards in the reservoir as a function of factors such as permeability and porosity.

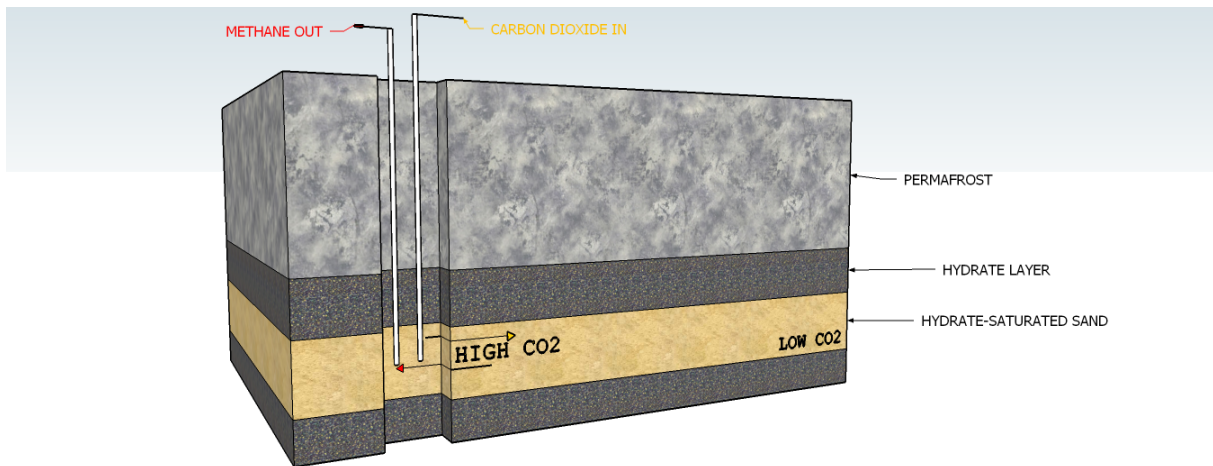


Figure 1.7:  $\text{CH}_4$  hydrate recovery from a permafrost reservoir. Made in SketchUp [35].

By simplifying the process as a function of H<sub>2</sub>O, CH<sub>4</sub> and CO<sub>2</sub>, the exchange process may be visualized in a ternary plot as displayed in Fig. 1.8. In a hydrate reservoir that is assumed to only consist of CH<sub>4</sub> hydrates, the composition is locked at the leftmost side of the ternary plot. By visualizing a process where CO<sub>2</sub> is pumped into the reservoir the concentration of CO<sub>2</sub> in the reservoir increases, and the overall composition consequently moves from the CH<sub>4</sub> vertex to the CO<sub>2</sub> vertex. The entire compositional range one might envision is possible during a CO<sub>2</sub>-CH<sub>4</sub> exchange process is thus located inside such a ternary plot. Accounting for possible phase transitions at specific concentrations, temperature and pressures, the ternary plot may be transformed into a ternary phase diagram. This is further discussed in Section 2.2.

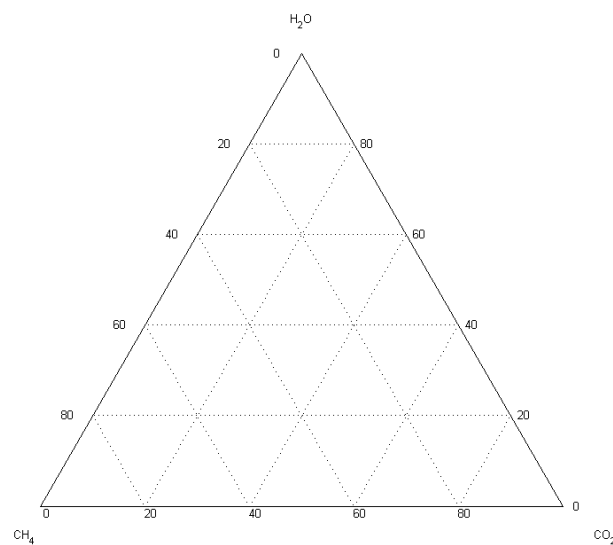


Figure 1.8: Ternary plot with H<sub>2</sub>O, CO<sub>2</sub>, and CH<sub>4</sub>. Plotted in MATLAB with the Ternplot script [36].

#### 1.4.1 Previous research on mixed CO<sub>2</sub>-CH<sub>4</sub> hydrates

An effort has been made to review previous research on mixed CO<sub>2</sub>-CH<sub>4</sub> hydrates, where Table 1.3 lists all the relevant articles. A discussion of the publications listed in the table is also provided in the subsequent pages. As the CO<sub>2</sub>/CH<sub>4</sub> mole ratio of the feed gas is generally varied over the entire range, an effort has been made to represent situations where several dissociation conditions are measured for a constant composition gas mixture. Selected L<sub>w</sub>-H-V equilibrium data from the literature with a constant CO<sub>2</sub>-CH<sub>4</sub> gas mixture composition is represented in Fig.1.9.

It should be noted that in the graphical representation it is assumed that the water amount and experimental procedure does not influence any of the measurements, and that the dissociation conditions listed in the reference are only a function of the feed gas composition. Only cases where  $\geq 3$  measurements are made for the constant composition are represented. The lines through the data are only to express them more explicitly.

The solid green lines in Fig. 1.9 are dissociation measurements for simple CO<sub>2</sub> or CH<sub>4</sub> hydrates. It may be observed in the figure that gas mixtures with compositions between the two extremes fall between the pure components experimental PT curves. A CO<sub>2</sub>-CH<sub>4</sub> gas mixture additionally has a different upper quadruple point than pure CO<sub>2</sub>, which varies depending on the fraction of CH<sub>4</sub> in the feed gas, L<sub>w</sub>-H-L<sub>CO2</sub> measurements are however not represented in Fig. 1.9.

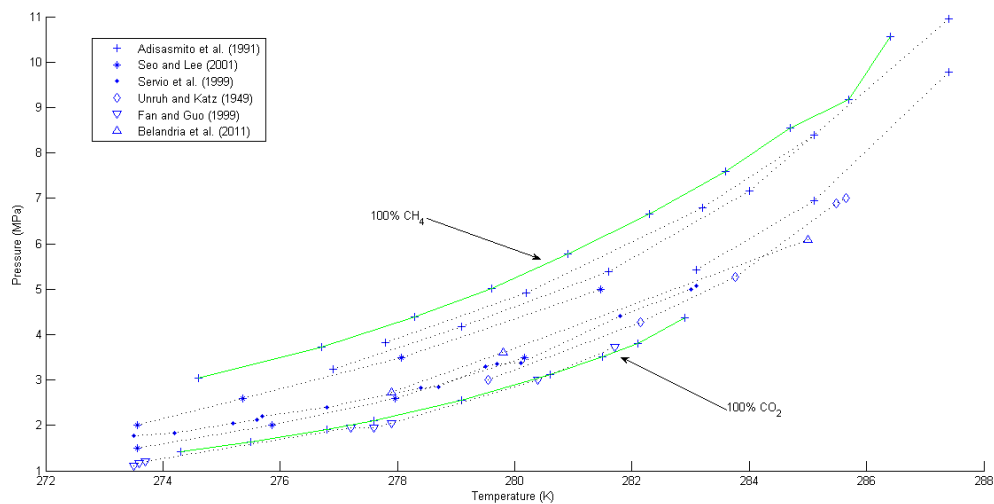


Figure 1.9: Previous constant composition L<sub>w</sub>-H-V measurements for mixed CO<sub>2</sub>-CH<sub>4</sub> hydrates.

Table 1.3: Previous studies on bulk hydrate equilibrium conditions formed from a CO<sub>2</sub>-CH<sub>4</sub> gas mixture with pure H<sub>2</sub>O.

Reference	Equilibria	Dissociation range (Temperature and Pressure)	Fraction CO <sub>2</sub> in feed gas	Data and information listed or deduced	# of exp. points
Unruh and Katz (1949) [37]	L <sub>w</sub> -H-V <sup>c</sup>	275.5 – 285.7 K and 1.99 – 7.00 MPa	0.055 – 0.71	V <sub>v</sub> , V <sub>water</sub> , y <sub>feed</sub> , y <sub>eq</sub>	17
Adisasmito et al. (1991) [38]	L <sub>w</sub> -H-V	273.7 – 287.6 K and 2.52 – 10.95 MPa	0.08 – 0.85	V <sub>v</sub> , V <sub>water</sub> , y <sub>feed</sub>	42
Dholabhai and Bishnoi (1994) [39]	L <sub>w</sub> -H-V	277.56 – 284.44 and 3.41 – 7.53 MPa	0.2	V <sub>v</sub> , V <sub>water</sub> , y <sub>feed</sub>	4
Ohgaki et al. (1996) [40]	L <sub>w</sub> -H-V	280.3 K and 3.04 – 5.46 MPa	–	y <sub>eq</sub> , x <sub>eq</sub> , z <sub>eq</sub>	31
Servio et al. (1999) [41]	L <sub>w</sub> -H-V	273.5 – 283.1 K and 1.78 – 5.07 MPa	0.2 and 0.5	V <sub>water</sub> , y <sub>feed</sub> , y <sub>eq</sub>	18
Fan and Guo (1999) [42]	L <sub>w</sub> -H-V <sup>c</sup>	273.5 – 282.3 K and 1.10 – 4.80 bar	0.9652	V <sub>v</sub> , V <sub>water</sub> , y <sub>feed</sub>	9
Seo et al. (2001) [43]	L <sub>w</sub> -H-V	273.56 – 283.26 K and 1.50 – 5.00 MPa – <sup>d</sup>	0.2 and 0.6	V <sub>v</sub> , V <sub>water</sub> , y <sub>feed</sub> , y <sub>eq</sub>	8
	H-V			y <sub>eq</sub> , z <sub>eq</sub>	14
	L <sub>w</sub> -H-V-L <sub>CO2</sub>	283.32 – 285.56 K and 4.53 – 6.72 MPa	y <sub>feed</sub>	3	
Seo and Lee (2001) [44]	L <sub>w</sub> -H-V	272.66 – 283.56 K and 1.50 – 5.00 MPa	–	V <sub>water</sub> , y <sub>eq</sub>	19 <sup>a</sup>
	L <sub>w</sub> -H-V-L <sub>CO2</sub>	283.32 – 285.76 and 4.412 – 7.251 MPa			4 <sup>b</sup>
Beltrán and Servio (2008) [45]	L <sub>w</sub> -H-V	275.14 – 285.34 K and 1.92 – 7.47 MPa	0.2 and 0.5	V <sub>v</sub> , V <sub>water</sub> , y <sub>feed</sub> , y <sub>eq</sub>	23
Bruusgaard et al. (2010) [46]	L <sub>w</sub> -H-V	274.02 – 280.05 K and 1.66 – 4.03 MPa	–	V <sub>water</sub> , y <sub>eq</sub> , x <sub>eq</sub>	12
Belandria et al. (2010) [47]	L <sub>w</sub> -H-V	279.1-289.9 K and 2.96 – 13.06 MPa	0.264 – 0.730	V <sub>water</sub> , y <sub>feed</sub>	11
Belandria et al. (2011) [48]	L <sub>w</sub> -H-V	277.9 – 285.5 K and 2.72 – 8.27 MPa	0.206 – 0.744	Total composition	9
	L <sub>w</sub> -H-V	273.6 – 284.2 and 1.51 – 7.19 MPa	–	Total composition, y <sub>feed</sub> , y <sub>eq</sub> , x <sub>eq</sub> , z <sub>eq</sub>	40
Herri et al. (2011) [49]	L <sub>w</sub> -H-V	277.15 K and 2.04 – 3.90 MPa	–	V <sub>water</sub> , y <sub>eq</sub> , z <sub>eq</sub>	6
Bi et al. (2013) [50]	L <sub>w</sub> -H-V-L <sub>CO2</sub>	283.09 – 287.04 and 4.46 – 8.37 MPa	0.780 – 1.00	V <sub>water</sub> , y <sub>feed</sub> , y <sub>eq</sub> , x <sub>eq</sub>	10

Where V<sub>v</sub> = vapor volume, V<sub>water</sub> = water volume, y<sub>feed</sub> = feed gas composition, y<sub>eq</sub> = vapor phase composition at equilibrium, z<sub>eq</sub> = hydrate phase composition at equilibrium, and x<sub>eq</sub> = aqueous phase composition at equilibrium.

<sup>a</sup>8 of the 19 measurements are listed in [43]. <sup>b</sup>1 of the 4 measurements are listed in [43]. <sup>c</sup>Some of the measurements might be in the liquid region for the CO<sub>2</sub>-CH<sub>4</sub> gas mixture (Appendix A.2). <sup>d</sup>Lists “sampling” temperature and pressure.

The study by Unruh and Katz (1949) was done in a time where gas chromatography was not available, and thus the initial vapor phase composition was calculated [37]. The following publications generally analyze the feed gas mixture and the vapor phase at equilibrium conditions by gas chromatography.

The study by Berecz and Balla-Achs (1974) who proposed that CO<sub>2</sub>-CH<sub>4</sub> hydrates exhibited instability at feed gas concentrations above 50% CO<sub>2</sub>, is not included in Table 1.3 [51]. Their measurements have been questioned by both Adisasmito et al. (1991) and Sloan and Koh (2008), where a hypothesis is that there was a presence of N<sub>2</sub> in their feed gas [4, 38].

Adisasmito et al. (1991) measured the L<sub>w</sub>-H-V equilibrium conditions for simple CO<sub>2</sub>- and CH<sub>4</sub> hydrates in addition to hydrates formed from a CO<sub>2</sub>-CH<sub>4</sub> gas mixture. A polynomial equation is proposed in their study that predicts the L<sub>w</sub>-H-V equilibrium pressure for mixed CO<sub>2</sub>-CH<sub>4</sub> hydrates based on the feed gas composition and the equilibrium temperature [38].

Dholabhai et al. (1994) examined the L<sub>w</sub>-H-V equilibrium conditions of mixed CO<sub>2</sub>-CH<sub>4</sub> hydrates formed with pure water and with various electrolyte solutions. The experiments performed with electrolyte solutions had lower equilibrium temperatures than the experiments performed with pure water [39], due to the competing ionic interactions previously mentioned (Section 1.2.3).

Ohgaki et al. (1996) examined the L<sub>w</sub>-H-V phase equilibria of mixed CO<sub>2</sub>-CH<sub>4</sub> hydrates at isothermal conditions (280 K). The aqueous phase composition and hydrate phase composition at equilibrium was determined by material balance. The distribution coefficient of CH<sub>4</sub>, which is the ratio of CH<sub>4</sub> in the vapor phase to CH<sub>4</sub> in the hydrate phase at equilibrium, was determined to be approximately 2.5. It is stated that CO<sub>2</sub> is the preferable guest molecule in the hydrate phase in the mixed system, and a possible CO<sub>2</sub>-CH<sub>4</sub> exchange scenario is discussed [40].

Fan and Guo (1999) examined the L<sub>w</sub>-H-V phase equilibria for a constant composition CO<sub>2</sub>-CH<sub>4</sub> gas mixture. The equilibrium pressure was measured to be only slightly higher than that of simple CO<sub>2</sub> hydrates due to the high CO<sub>2</sub> concentration in the feed gas. The phase equilibrium conditions for a 94.98% CO<sub>2</sub> + 5.02% CH<sub>4</sub> mixture forming hydrates with a 9.45 mass% NaCl aqueous solution was additionally examined [42].

Servio et al. (1999) examined the  $L_w$ -H-V phase equilibria for both the  $\text{CO}_2$ - $\text{CH}_4$ - $\text{H}_2\text{O}$  and the  $\text{CO}_2$ - $\text{CH}_4$ - $\text{H}_2\text{O}$ -neohexane system with a feed gas composition of 20% and 50%  $\text{CO}_2$  [41]. These systems were re-examined by Beltrán and Servio (2008) with additional feed gas compositions [45]. Only equilibrium conditions for the 20 and 50  $\text{CO}_2\%$  feed gas mixture are however represented with certainty in the latter study, and are consequently the only measurements listed in Table 1.3. For both studies sH hydrates were formed at various compositions and thermodynamic conditions for the  $\text{CO}_2$ - $\text{CH}_4$ - $\text{H}_2\text{O}$ -neohexane system, where a lower hydrate formation pressure was observed than for the  $\text{CO}_2$ - $\text{CH}_4$ - $\text{H}_2\text{O}$  system which formed sI [41, 45].

Seo et al. (2001) examined the  $L_w$ -H-V and H-V equilibria for hydrates formed from a  $\text{CO}_2$ - $\text{CH}_4$  gas mixture with pure water at various isobaric conditions. Four  $L_w$ -H- $L_{\text{CO}_2}$ -V equilibrium conditions were additionally measured, however not at isobaric conditions. For the two-phase H-V equilibrium measurements the authors determined both the vapor phase composition and the composition of the hydrated vapor phase. The hydrated vapor phase composition was determined by decomposing an isolated hydrate sample [43]. The composition of the gas initially charged to the cell is only listed for  $L_w$ -H-V measurements.

Seo and Lee (2001) reinvestigated the  $L_w$ -H-V equilibrium conditions for mixed  $\text{CO}_2$ - $\text{CH}_4$  hydrates, with an additional 10 measurements listed in addition to data from the previous study. 4 measurements of  $L_w$ -H-V- $L_{\text{CO}_2}$  equilibrium conditions are additionally listed [44]. The phase compositions of four  $L_w$ -H-V experiments are represented in ternary phase diagrams, and this is the only study discovered where the three-component system is represented in such a way. The composition of the phases is however not listed. The composition of the four phase  $L_w$ -H-V- $L_{\text{CO}_2}$  upper quadruple point is also represented in a ternary phase diagram at 5.0 MPa and 283.86 K [44]. However, such a four-phase representation in a ternary phase diagram is a violation of Gibb's phase rule (see Section 2.2.1), and is therefore a questionable representation of data.

Bruusgaard et al. (2010) measured the vapor phase- and aqueous phase composition for the  $\text{CO}_2$ - $\text{CH}_4$ - $\text{H}_2\text{O}$  system at  $L_w$ -H-V conditions. It was observed that the solubility of  $\text{CH}_4$  increased with increased pressure and decreased temperature, while the solubility of  $\text{CO}_2$  increased with decreased pressure and increased temperature [46].



Belandria et al. (2010) compared their experimental  $L_w$ -H-V equilibrium conditions for the  $CO_2$ - $CH_4$ - $H_2O$  system with predicted equilibrium conditions from the equation proposed by Adisasmito et al. (1991), and from hydrate simulation software HWHYD [47]. The subsequent re-examination study of the  $CO_2$ - $CH_4$ - $H_2O$  system by Belandria et al. (2011) is the only discovered study that have listed the full system composition for their experiments (49 pts. in total). The composition of the vapor phase at  $L_w$ -H-V equilibrium was determined by GC analysis, while the hydrate and aqueous phase composition was determined by material balance. The experimental dissociation data, and the compositional data were additionally compared with equilibrium predictions, and compositional phase predictions from hydrate software CSMGem and HWHYD [48].

Herri et al. (2011) examined the  $L_w$ -H-V equilibrium conditions for mixed  $CO_2$ - $CH_4$  hydrates, where the vapor phase composition was determined through GC analysis, and a material balance was utilized to determine the composition of the other phases. An accurate water composition of the hydrate phase was determined by utilizing  $LiNO_3$  as a tracer. The concentration difference of  $LiNO_3$  species in the aqueous phase at start conditions vs. equilibrium conditions was utilized to determine the moles of water in the hydrate structure as  $LiNO_3$  is not incorporated into the hydrate [49].

Bi et al. (2013) determined the upper quadruple point of mixed  $CO_2$ - $CH_4$  hydrates, with relatively high concentrations of  $CO_2$  in the feed gas. Two sets of experiments are represented; one with low water content and one with high water content. The “width” of the upper quadruple phase region is presented, and the critical point for the upper quadruple region is listed as 287.9 K and 8.4 MPa with a feed gas mole fraction of 0.755  $CO_2$  [50].

Seo and Lee (2002) examined the  $L_w$ -H-V equilibrium conditions for mixed  $CO_2$ - $CH_4$  hydrates in silica gel pores [52]. As the measurements were done in a porous medium the measured equilibrium conditions are not directly comparable to  $L_w$ -H-V measurements in bulk, and are consequently not listed in Table 1.3. Higher pressures and lower temperatures were required to form hydrates in the silica pores, which was attributed to geometrical constraints [52].

Akihiro et al. (2004) examined the I-H-V phase equilibria for mixed  $CO_2$ - $CH_4$  hydrates with a feed gas  $CO_2$  fraction of 0.25, 0.50, and 0.75. A limited amount of quantitative data is listed in the study as their main objective was to examine the kinetics of hydrate formation and dissociation from ice [53]. The study is consequently not listed in Table 1.3.

## 1.5 Approach and overview

The primary objective of this thesis was to examine the thermodynamic phase equilibria of mixed CO<sub>2</sub>-CH<sub>4</sub> hydrates. This was a response to the proposed CO<sub>2</sub>-CH<sub>4</sub> recovery method which has been extensively researched throughout the last decade [3]. It is hereby hypothesized that the thermodynamic phase equilibria of the CO<sub>2</sub>-CH<sub>4</sub> exchange process may be analyzed from another perspective by investigating the phase equilibria of mixed CO<sub>2</sub>-CH<sub>4</sub> hydrates in ternary phase diagrams. With the exception of the study by Seo and Lee (2001), this approach to the CO<sub>2</sub>-CH<sub>4</sub> exchange process have not been observed anywhere else.

In the studies by Belandria et al. (2010), and Belandria et al. (2011) the hydrate prediction software HWHYD and CSMGem was utilized to examine measured equilibrium conditions [47, 48]. PVTsim has not to our knowledge been used to investigate the phase behavior of mixed CO<sub>2</sub>-CH<sub>4</sub> hydrates.

PVTsim with Open Structure has been utilized to simulate the three-component CO<sub>2</sub>-CH<sub>4</sub>-H<sub>2</sub>O system in this thesis. In the context of reviewing the CO<sub>2</sub>-CH<sub>4</sub> recovery method as a function of the three-component system through PVTsim simulations, the simulations performed has to be accurate, reliable, and ultimately be comparable to real-world phenomena's. The accuracy of PVTsim predictions in regards to the equilibrium conditions of mixed CO<sub>2</sub>-CH<sub>4</sub> hydrates have consequently been extensively examined. A detailed description of PVTsim and ternary phase diagrams is provided in Chapter 2.

## CHAPTER 2: METHODS

### 2.1 PVTsim

PVTsim is a software program that allows the user to model and simulate fluid properties as a function of pressure, volume, temperature, and composition. It includes various cubic equations of state (EOS) and powerful algorithms that results in reliable and robust flash calculations and simulations [54]. The software is developed by Calsep, and is used by several petroleum companies and researchers worldwide [55].

#### 2.1.1 Equations of state and hydrate modelling

The physical state of a substance is determined by its physical properties. The simplest form of an equation of state is the ideal gas equation, which relates three properties of a gas to a fourth ( $P$ ,  $V$ ,  $n$ ,  $T$ ) [18].

Cubic equations of state are utilized for the majority of oil and gas mixture PVT calculations in the petroleum and research industry. The first was derived by van der Waal in 1873 and relates the properties of real gases from one attractive and one repulsive parameter. These parameters are generally determined from the critical temperature and pressure of the substance. Subsequent equations have improved predictions on vapor pressure- and phase properties, and additionally allowed for calculations of mixtures. The Soave-Redlich-Kwong (SRK) and the Peng-Robinson (PR) equation of state are most frequently used. The imperfect liquid density predictions for both equations were in 1982 improved by the Peneloux volume correction parameter [56]. For derivation of these cubic equations of state the reader is referred to the work of Pedersen and Christensen [56].

Hydrate formation conditions and phase properties in PVTsim are calculated by the method by Munck et al. (1988), where the reader is referred to for an in-depth explanation [56, 57]. It is based upon the classical van der Waals' and Platteeuw adsorption model where the possibility of a gas molecule occupying a cavity in the hydrate structure is calculated by the Langmuir adsorption theory. The fugacity parameter in the Langmuir expression is calculated by the selected cubic equation of state. Essentially, the model is based upon the fact that hydrates form when the hydrate state is the energetically preferable state compared to the other states in the system, e.g. gas and liquid [56, 57].

### 2.1.2 Flash calculations in PVTsim

PVTsim features a fluid database where the user may define various mixtures with different components and adjustable total composition; hereby referred to as fluids. These fluids are subsequently used as inputs for the various algorithms available in PVTsim. A brief explanation of the algorithms utilized are subsequently presented.

#### Flash calculations

Figure 2.1 illustrates a simple flash calculation. A flash calculation can be applied to a fluid to predict the number of phases, various properties of each phase, and the composition of each phase at specific pressure and temperature (PT flash). Other variables such as H, S, or V (enthalpy, entropy, volume) may also be used as dependent variables in flash calculations [54].

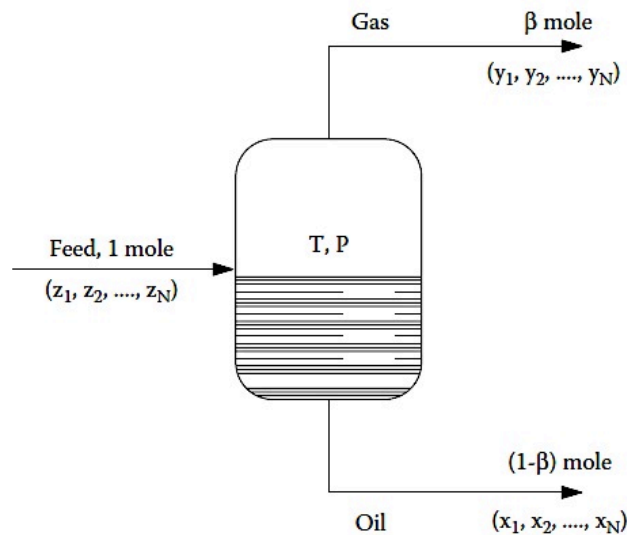


Figure 2.1: Flash calculation applied to a conventional reservoir fluid. Where  $z_1, z_2, \dots, z_N$  are component mole fractions in the feed. T and P are temperature and pressure,  $\beta$  is the vapor mole fraction,  $(y_1, y_2, \dots, y_N)$  are the component mole fractions in the vapor phase and  $(x_1, x_2, \dots, x_N)$  are the component mole fractions in the liquid (oil) phase. From [56].

#### Phase envelope estimations

The phase envelope module in PVTsim predicts vapor pressure curves for pure components and mixtures, including the critical point of the fluid [54]. It has mainly been utilized in this thesis to determine the phase envelope of pure  $\text{CO}_2$ , and to determine the phase envelope of the gas mixture utilized for the experiments at Statoil.

### 2.2.3 Hydrate flash calculations in PVTsim

#### Hydrate PT flash

The Hydrate PT flash predicts the same properties and phases as an ordinary PT flash, but it also accounts for the possibility of a solid phase. A PT hydrate flash may thus predict the following phases: hydrate, aqueous, ice, vapor and non-aqueous liquid, depending on the fluid composition and flash conditions. The properties and the composition of the phases are also predicted. PVTsim allows for the prediction of sI, sII and sH hydrate [54].

#### Hydrate PT Curve

The Hydrate PT Curve algorithm in the hydrate module predicts the equilibrium conditions for hydrate onset for a given fluid. The hydrate temperature predicted is thus the temperature one might expect the first hydrate crystal to appear during system cooling [54, 58]. This does not mean that hydrate formation instantaneously occurs at these conditions.

As briefly explained in Section 1.2.4, hydrate formation is characterized by kinetic effects such as metastability, growth and heat transport [4], which are factors that PVTsim does not account for. PVTsim predicts only the thermodynamic equilibrium conditions for hydrate onset. The equilibrium conditions predicted by PVTsim is consequently also the conditions where one might expect the first hydrate crystal to disappear during dissociation, i.e., the dissociation conditions [54, 58]. Hydrate PT curves for CH<sub>4</sub> (blue) and CO<sub>2</sub> (red) were previously presented in Fig. 1.3 (Section 1.2.3).

Predicted PT curves have been superimposed on all PT traces of experiments performed at UiB in this thesis to determine the accuracy of the measurements.

#### Hydrate Pressure and Hydrate Temp

In this context, Hydrate Temp predicts the dissociation temperature for a specific fluid composition and dissociation pressure, while Hydrate Pressure predicts the dissociation pressure for a specific fluid composition and dissociation pressure.

The Hydrate Temp and the Hydrate Pressure algorithm has been utilized to examine the accuracy of PVTsim predictions. Measured dissociation conditions from the literature have been used as input values. The accuracy of PVTsim have subsequently been measured as the deviation and relative deviation between measured dissociation conditions and predicted dissociation conditions by PVTsim.

## 2.2.4 Accuracy of PVTsim predictions

In all previous studies on the three-component CO<sub>2</sub>-CH<sub>4</sub>-H<sub>2</sub>O system there is a lack of reporting the total system composition for the experiments performed. Of all studies, only Belandria et al. (2011) reports the total system composition for each experiment (9 + 40 pts.) [48]. Dissociation conditions from the literature are consequently difficult to model.

For some of the studies listed in Table 1.3 the total system composition has been calculated to a reasonable accuracy. To examine previous experimental data with PVTsim the following variables have to be known: water amount/volume, vessel volume, feed gas composition and equilibrium conditions. By assuming that the listed conditions are the conditions where the last hydrate crystal melts, the system may be modeled as a vapor and aqueous two-phase system. The solubility of the hydrate formers in water is neglected, and it is assumed that the vapor composition is the same at dissociation conditions as it is at initial conditions, i.e., the feed gas composition.

As the water volume is listed, the number of moles of water is calculated by:

$$n_{\text{water}} = \frac{V_{\text{water}} \cdot \rho_{\text{water}}}{M_{\text{water}}} \quad (2.1)$$

Where  $V_{\text{water}}$  is the water volume in cm<sup>3</sup>,  $\rho_{\text{water}}$  is the density of water in g/cm<sup>3</sup>, and  $M_{\text{water}}$  is the molar mass of water at 18.015 g/mol. The density of water is calculated by the water package algorithm in the property generator module in PVTsim at dissociation conditions [11].

The total moles of vapor are calculated by:

$$n_{\text{vapor}} = \frac{P_{\text{exp}} \cdot V_{\text{vapor}}}{Z_{\text{vapor}} \cdot R \cdot T_{\text{exp}}} \quad (2.2)$$

$P_{\text{exp}}$  and  $T_{\text{exp}}$  are the listed experimental dissociation pressure and temperature, respectively.  $Z_{\text{vapor}}$  is the compressibility factor of the CO<sub>2</sub>-CH<sub>4</sub> gas mixture, determined by flashing the gas mixture composition in PVTsim at listed dissociation conditions [11].  $R$  is the gas constant at 8.314 cm<sup>3</sup> MPa K<sup>-1</sup> mol<sup>-1</sup>.  $V_{\text{vapor}}$  is the vapor volume in cm<sup>3</sup>, determined by:

$$V_{\text{vapor}} = V_{\text{cell}} - V_{\text{water}} \quad (2.3)$$

Where  $V_{\text{cell}}$  is the volume of the experimental vessel in  $\text{cm}^3$ , and  $V_{\text{water}}$  is the volume of water in  $\text{cm}^3$ .

The total number of moles in the vapor is then:

$$n_i = y_i \cdot n_{\text{vapor}} \quad (2.4)$$

Where  $y_i$  is the mole fraction of component  $i$  in the feed gas mixture, where  $i = \text{CO}_2$  or  $\text{CH}_4$ .

The total number of moles is then:

$$n_{\text{tot}} = n_{\text{H}_2\text{O}} + n_{\text{CO}_2} + n_{\text{CH}_4} \quad (2.5)$$

The mole fraction of each component is subsequently calculated and used as the fluid composition in PVTsim. The fluid is flashed using the Hydrate Temp algorithm by using the dissociation pressure listed in the study to predict the dissociation temperature, and the Hydrate Pressure algorithm by using the dissociation temperature listed in the study to predict the dissociation pressure. The accuracy of PVTsim is measured as the deviation in temperature (D T) and relative deviation in pressure (RD% P):

$$D T = T_{\text{exp}} - T_{\text{pred}} \quad (2.6)$$

$$RD\% P = \frac{P_{\text{exp}} - P_{\text{pred}}}{P_{\text{exp}}} \cdot 100\% \quad (2.7)$$

Where  $P_{\text{exp}}$  and  $T_{\text{exp}}$  are the listed experimental dissociation pressure and temperature, respectively.  $P_{\text{pred}}$  and  $T_{\text{pred}}$  are the predicted dissociation pressure and temperature, respectively. The absolute values are additionally calculated for the deviations above, by Eq.(2.8) and Eq.(2.9):

$$AD T = |T_{\text{exp}} - T_{\text{pred}}| \quad (2.8)$$

$$ARD\% P = \frac{|P_{\text{exp}} - P_{\text{pred}}|}{P_{\text{exp}}} \cdot 100\% \quad (2.9)$$

### 2.2.5 Compositional predictions by PVTsim

The sum of the components in a phase predicted by PVTsim equals 100%, illustrated with Eq.(2.10) for the three-component CO<sub>2</sub>-CH<sub>4</sub>-H<sub>2</sub>O system.

$$\%H_2O + \%CO_2 + \%CH_4 = 100\% \quad (2.10)$$

The CO<sub>2</sub> fraction in the vapor, hydrate and aqueous phase is then respectively calculated as:

$$y_{CO_2} = \frac{Y_{CO_2}}{Y_{H_2O} + Y_{CO_2} + Y_{CH_4}} \quad (2.11)$$

$$z_{CO_2} = \frac{Z_{CO_2}}{Z_{H_2O} + Z_{CO_2} + Z_{CH_4}} \quad (2.12)$$

$$x_{CO_2} = \frac{X_{CO_2}}{X_{H_2O} + X_{CO_2} + X_{CH_4}} \quad (2.13)$$

Predictions by PVTsim has additionally been compared with compositional data listed by Belandria et al. (2011) [48] in Section 4.1.2.  $y_{CO_2}$  and  $z_{CO_2}$  presented in Section 4.1.2 are however calculated by Eq.(2.14) and Eq.(2.15). The H<sub>2</sub>O term in the previous equations is essentially removed from the denominator, and the fraction of CO<sub>2</sub> in the vapor- and the hydrate phase is determined by:

$$y_{CO_2} = \frac{Y_{CO_2}}{Y_{CO_2} + Y_{CH_4}} \quad (2.14)$$

$$z_{CO_2} = \frac{Z_{CO_2}}{Z_{CO_2} + Z_{CH_4}} \quad (2.15)$$

The amount of H<sub>2</sub>O in the vapor is considered as negligible, and the fraction of CO<sub>2</sub> in the hydrate phase is essentially the fraction of CO<sub>2</sub> in the “hydrated vapor phase”. This method was employed as this was the same method employed by Belandria et. al (2011), to present their compositional findings for mixed CO<sub>2</sub>-CH<sub>4</sub> hydrates [48]. Compositional predictions by PVTsim based upon listed system composition and dissociation conditions, could then be compared to the listed phase composition in the study.



The relative deviation and absolute relative deviation with regards to listed compositional values by Belandria et al. (2011) [48], and predicted compositional values by PVTsim has been calculated by Eq.(2.16) and Eq.(2.17) respectively.

$$RD\% = \frac{C_{\text{exp}} - C_{\text{pred}}}{C_{\text{exp}}} \cdot 100\% \quad (2.16)$$

$$ARD\% = \frac{|C_{\text{exp}} - C_{\text{pred}}|}{C_{\text{exp}}} \cdot 100\% \quad (2.17)$$

Where  $C$  is  $y_{\text{CO}_2}$ ,  $z_{\text{CO}_2}$ ,  $x_{\text{H}_2\text{O}}$ ,  $x_{\text{CH}_4}$  or  $x_{\text{CO}_2}$ .  $C_{\text{exp}}$  refer to the compositional values listed by Belandria et al. (2011) [48], while  $C_{\text{pred}}$  refer to compositional values calculated from the phase compositions predicted by PVTsim.

## 2.2 Ternary plots

A ternary plot is a triangular graphical representation of data. Ternary plots are frequently utilized to display the composition of a three-component mixture. Each apex of a ternary plot corresponds to 100 mole percent (or 1.0 mole fraction) of a single component. The outer borders represent a two-component mixture while a point within represents a three-component mixture. The composition is generally plotted in mole percent or mole fraction; weight percent and weight fraction is however also possible [59-62].

As the sum of the proportions of the components in a three-component mixture equals 100% (or 1) only the proportions of two components are required to define the last [59-62]:

$$A + B + C = 100\% \quad (2.18)$$

The easiest way to read the composition of a mixture from a ternary diagram is to draw lines through the point for each vertex, here with dashed red lines. The concentration of each component may subsequently be read from the base label for each component. The point in Fig. 2.2 has a composition of 40% A, 20% B, and 40% C.

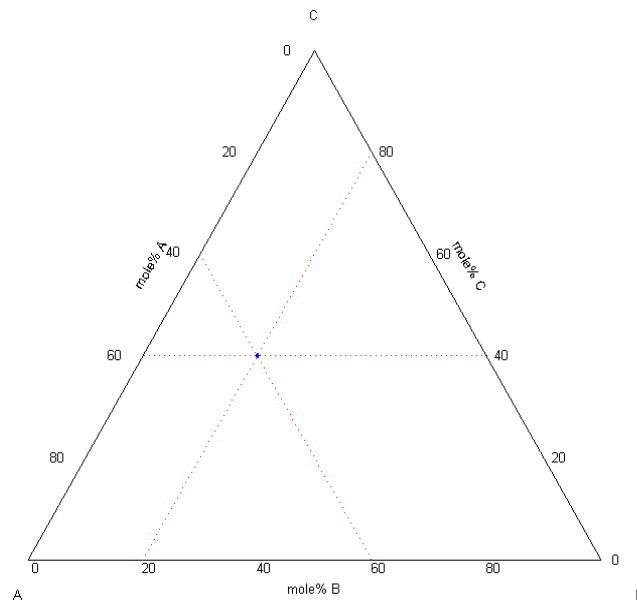


Figure 2.2: Illustrative example of a ternary A-B-C system. Plotted in MATLAB with the Ternplot script [36].

### 2.2.1 Ternary phase diagrams

A ternary plot can be utilized to display the phase behavior of a three-component mixture; consequently referred to as a ternary phase diagram. As with all phase diagrams, ternary phase diagrams follows Gibbs' phase rule (Equation 1.5). For a three-component mixture with at least one phase, the system has four degrees of freedom (pressure, temperature, and the composition of two of the components) [59-62].

$$F = 3 - 1 + 2 \quad (2.19)$$

As a four variable system is rather difficult to represent graphically, temperature and pressure is usually kept constant. The compositional relationship of the three components and their phase behavior may thus be evaluated in a ternary plot. At constant pressure and temperature the phase rule reduces to [59-62]:

$$F = 3 - P \quad (2.20)$$

The maximum number of possible phases is thus three ( $F = 0$ ), which is represented in a ternary diagram as an area. Two phases ( $F = 1$ ) are represented as a line, and one phase ( $F = 2$ ) is represented as a point [59-62].

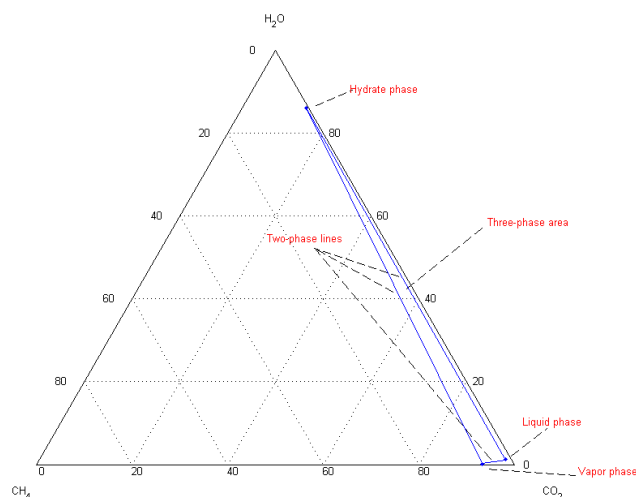


Figure 2.3: Example of a ternary phase diagram that illustrates each phase (point/line/area). Plotted in MATLAB with the Ternplot script [36].

Tie lines connect phases that are in equilibrium with each other, where two end-points of a tie line represent two separate phases [59-62]. Tie lines are probably best expressed with an example. Consider the CO<sub>2</sub>-CH<sub>4</sub>-H<sub>2</sub>O system in the foundational ternary phase diagram in Fig. 2.4. A mixture with a composition of 40% H<sub>2</sub>O, 30% CO<sub>2</sub> and 30% CH<sub>4</sub> is represented with the red dot in the figure. A hydrate flash calculation in PVTsim with the aforementioned fluid results in a hydrate phase and a vapor phase prediction. These phases are plotted as blue points in the figure.

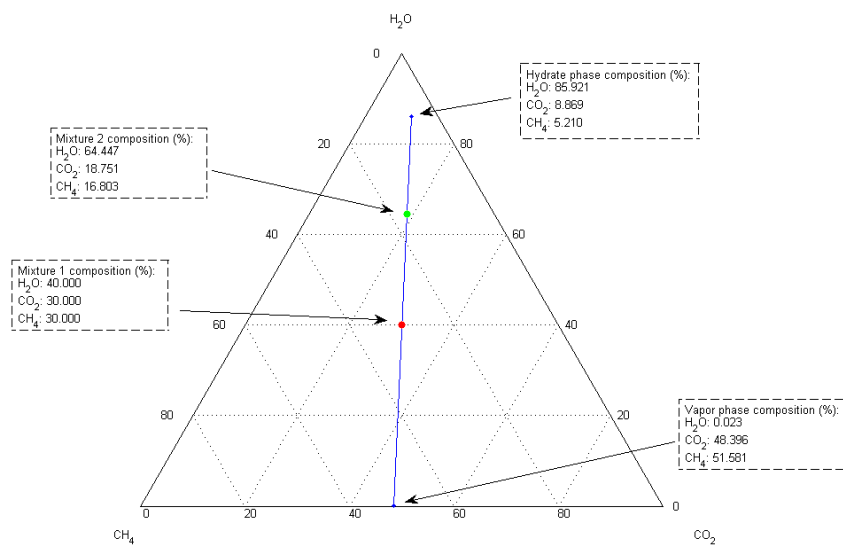


Figure 2.4: Ternary phase diagram with a single tie line. Flash conditions: 4.0 MPa and 275.15 K.

By applying Gibbs' phase rule to the tie line where two phases are in equilibrium ( $P = 2$ ) and there are three components ( $C = 3$ ), there is consequently one degree of freedom ( $F = 1$ ). Thus by only determining one component, the other two are instantaneously fixed.

A second mixture is plotted on the tie line as a green point, with a composition of 64.447% H<sub>2</sub>O, 18.751% CO<sub>2</sub> and 16.803% CH<sub>4</sub>. A hydrate flash calculation in PVTsim predicts the same phases for this fluid as for the first, with the exact same phase composition. The only difference is the amount of each phase formed. If the fluid composition is located near the hydrate point of the tie line more hydrate will form, which is the case for the second fluid. The same principle applies for a 3-phase area. The 3-phase area is fixed as the degrees of freedom are 0. By moving inside the 3-phase triangle, the amount of the three phases changes, while the composition of the different phases remains constant. The amount of each phase formed can be calculated with the lever rule [62].

### 2.2.1 PVTsim open structure and ternary phase diagrams

It is possible to write a MATLAB script that can utilize several of the modules and algorithms available in PVTsim through the Open Structure package. Instead of manually flashing several fluids in the PVTsim interface a MATLAB script may perform the desired procedures automatically. The data predicted by PVTsim may subsequently be represented graphically. A script that flashes the three-component CO<sub>2</sub>-CH<sub>4</sub>-H<sub>2</sub>O system and represents the predicted phase compositions in a ternary phase diagram has been utilized in this thesis, courtesy of Per Fotland.

The fluid which is selected in the script is defined in PVTsim with a composition of 50.000% H<sub>2</sub>O, 0.001% CO<sub>2</sub> and 49.999% CH<sub>4</sub>. The MATLAB script flashes this fluid at a temperature and pressure that is defined in the script. The subsequent fluid to be flashed has another composition determined by the script, e.g. 50.000% H<sub>2</sub>O, 0.006% CO<sub>2</sub>, and 49.994% CH<sub>4</sub>. In this case, 0.005% is added to CO<sub>2</sub> for each flash, and consequently 0.005% is subtracted from CH<sub>4</sub> for each flash. The numbers of flashes are also determined through the script in MATLAB. The water amount does not change for each flash. The water amount may however be changed inside the PVTsim software, and a system with a higher or lower water content may consequently be modeled.

For each hydrate flash, PVTsim calculates phases formed and the composition of the phases; these phases are subsequently plotted in a ternary phase diagram. As the amount of CO<sub>2</sub> in the system increases, the entire phase behavior of the CO<sub>2</sub>-CH<sub>4</sub>-H<sub>2</sub>O system at constant pressure and temperature can be predicted.

Chapter 4 presents nine ternary phase diagrams modeled through PVTsim with the Open Structure MATLAB script. A significant difference in phase predictions was observed between the SRK- and the PR equation of state.

# CHAPTER 3: EXPERIMENTAL

## 3.1 Chemicals and fluids

Table 3.1 lists the chemical compounds utilized for the experiments at UiB and Statoil.

Table 3.1: The chemical compounds used in the experiments, with purity listed.

Compound	Supplier	Purity
H <sub>2</sub> O utilized at UiB	-	Distilled
H <sub>2</sub> O utilized at Statoil	-	Deionized
CH <sub>4</sub> utilized at UiB	Yara Praxair	99.9995%
CH <sub>4</sub> utilized at Statoil	Airliquid	99.995
CO <sub>2</sub> utilized at UiB	Yara Praxair	99.999%
CO <sub>2</sub> utilized at Statoil	-	99.99999%

## 3.2 Experimental setup

StatoilHydro ASA donated the hydrate cell and its associated parts to the University of Bergen some years ago. A significant amount of work has been performed to update the equipment, and to fit the equipment to the experiments that are desired. All parts of the setup have been subjected to maintenance and modifications.

Figure 3.1 presents a technical sketch of the experimental setup. The main part is a cooling incubator with temperature control that encloses the hydrate cell. The gas cylinder is connected to the cell with Swagelok tubing. Agitation of the cell volume is possible with the stirrer that goes through the top cap of the cell. An electric motor transfers torque to the stirrer through a belt transmission.

The Dynisco  $\mu$ PR700 indicator and the West 8100 controller measures pressure and temperature. These are connected to the pressure transducer and the PT RTD (Platinum resistance thermometer) respectively. The PT data is collected by the NI USB-6341 data acquisition (DAQ) hardware, where it is subsequently converted and stored on a computer hard drive by the LabVIEW software.

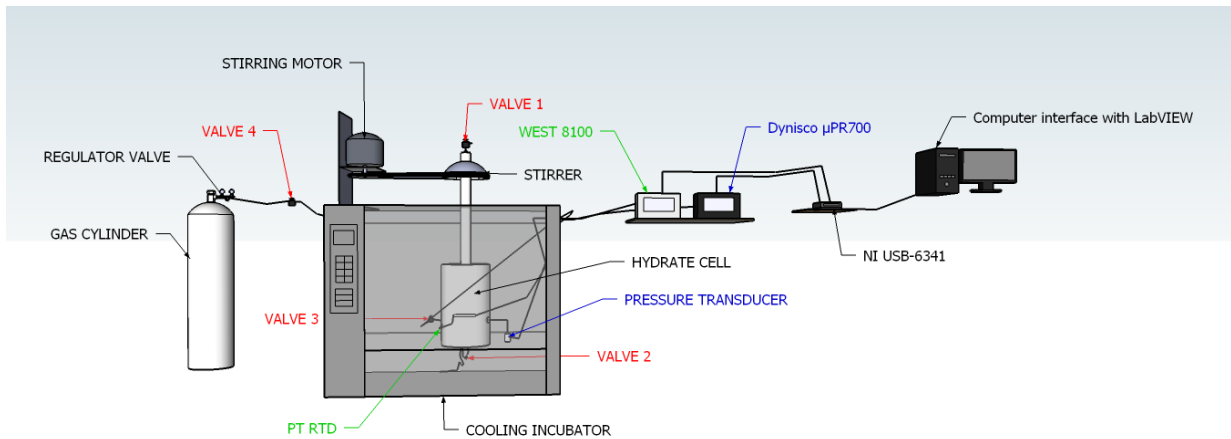


Figure 3.1: Technical sketch of the experimental setup and equipment utilized in this thesis. Made in SketchUp [35].

### 3.2.1 The cooling incubator

The cooling incubator is a Termaks KBP 6087 with a temperature range of 0 – 70 °C. The front panel of the incubator has a LCD display where the desired temperature and rate is set. The time dependent temperature fluctuations is  $\pm 0.1$  °C. The interior temperature of the cabinet has a variation of  $\pm 0.2$  °C (the temperature sensor incorporated in the interior of the cabinet, not the one used to measure the temperature.) [63].



Figure 3.2: The Termaks KBP 6087 cooling incubator.

The incubator reaches the set temperature in a few hours. The hydrate cell that has a large mass takes a longer time to reach the set temperature, due to the stainless steel heat capacity. All experiments were cooled down without a set cooling rate. The rate was set at zero so that the incubator would cool down as fast as possible. The heating rate was however controlled, and was varied between some of the experiments as needed. A procedure for the incubator is provided in Appendix B.1.

### 3.2.2 Hydrate cell

The stainless steel hydrate cell has a diameter of 6.61 cm, a height of 14.2 cm and an internal volume of 468 cm<sup>3</sup> [8-10].

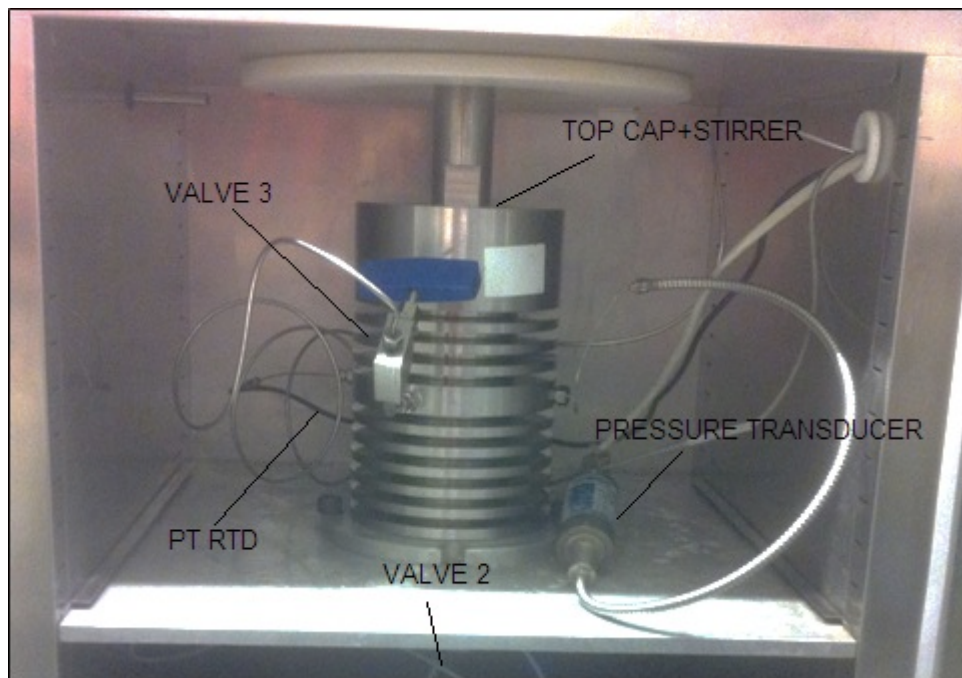


Figure 3.3: The stainless steel hydrate cell.

Valve 3 is visible in Fig. 3.3, which is where the gas is injected through the Swagelok tubing. Valve 2 is located below the bracket that the hydrate cell is connected to, which is the valve used to introduce water into the cell by vacuum.



Several gas leaks were observed during an initial pressure test of the system. Each valve was consequently refurbished, where rust was removed by a steel brush and WD-40. The grooves in the hydrate cell that connects the top cap and the stirring shaft to the cell have also been extensively refurbished as it was difficult to tighten the top cap to the cell. The interior of the volume was isolated during this to avoid contamination. The cell was additionally thoroughly cleaned.

The Swagelok nuts connected to the valves, and the grooves of the hydrate top cap were all lubricated with high quality vacuum grease to prevent any subsequent gas leaks from the system.

### 3.2.3 The rotating stirrer

The stirring shaft which is joined to the hydrate cell through the top cap is connected to the VEM GmbH electric motor through a belt transmission. The small rotating plate connected to the motor transfers torque to the rotating stirrer via belt transmission. This rotating plate experienced a significant amount of strain during experiments, where the bolt connecting the plate to the motor consequently disconnected several times. This was finally solved by drilling three screws into the safety disk which holds the rotating plate in place.



Figure 3.4: The VEM GmbH electric motor to the left is controlled by the Siemens MICROMASTER inverter to the right.

The electrical frequency (Hz) input parameter of the inverter that can be accessed through the LCD display on the inverter determines the motor speed. A higher input frequency value results in a higher rotating speed. The rpm value displayed by the inverter was however incorrect. A stroboscope was consequently utilized to measure the frequency of the rotating stirrer, which allowed for the true rpm value to be determined.

A stroboscope is an instrument that repetitively flashes a light with an adjustable frequency. The stroboscope was pointed at a marked line at the top of the stirrer. When the marked line appeared stationary the frequency of the stroboscope matched the frequency of the stirrer. A number of points at various electrical frequency input values were measured, which resulted in the linear graph in Fig. 3.5.

The relationship between rpm (revolutions per minute) and hertz (revolutions per second) is:

$$1 \text{ rpm} = \frac{1}{60} \text{ Hz} \quad (3.1)$$

The measured frequencies by the stroboscope were consequently converted to rpm values. To determine the required input electrical frequency corresponding to a desired rpm value the calibration curve in Fig. 3.5 was constructed.

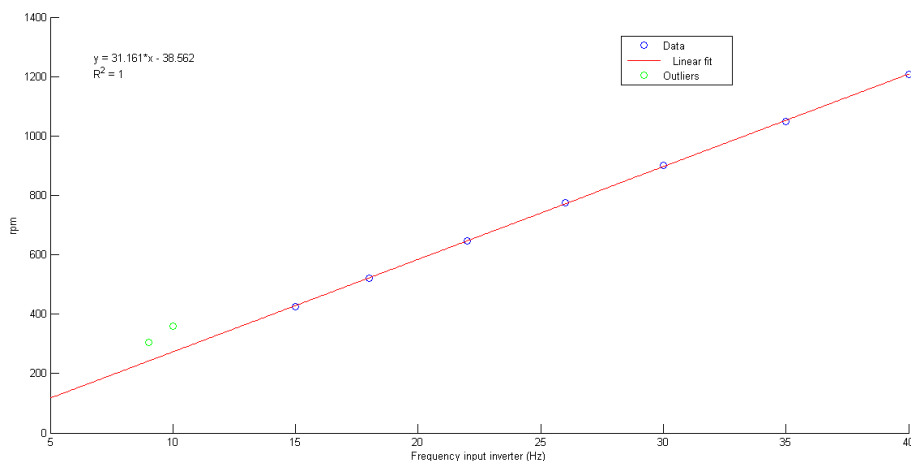


Figure 3.5: The linear relationship established to determine input electrical frequency values for desired rotational motor speed.  $y = 31.161x - 38.562$ , where  $y$  is the rpm value and  $x$  is the frequency input in the inverter (Hz).

The two points deviating from the linear fit is due to problems stabilizing the image when measuring the frequency of the rotating stirrer. This is again due to the low torque from the motor, thus the stirrer cannot achieve a constant speed. For this reason it is not recommended to run the motor at low speeds [64].

A rotational speed of 600 rpm was utilized for all experiments in this thesis as this was generally the rotational speed used in previous work on the system [8-10]. The electrical input frequency required to rotate the stirrer at approximately 600 rpm was calculated to 20.5 Hz.

### 3.2.4 Pressure and temperature sensors

The PT RTD (Platinum resistance thermometer) is connected to the West 8100 controller, which displays the temperature in °C. The pressure transducer is connected to the Dynisco  $\mu$ PR700 pressure indicator, which displays pressure in bar.



Figure 3.6: The Dynisco  $\mu$ PR700 pressure indicator to the left, and the West 8100 temperature controller to the right.

The measurement accuracy of the West 8000 controller is listed in the user manual as  $\pm 0.1\%$   $\pm 1$  LSD (least significant digit) [65]. The temperature is displayed as XX.X on the WEST 8100 controller. As the temperature range of the experiments performed in this thesis are within the range of 1.0 - 30.0 °C, the percent uncertainty is generally insignificant as it is less than the measured LSD (0.001 – 0.003).

The uncertainty in the LSD is however significant. The LSD additionally varied during the calibration procedure, e.g.  $XX.\underline{X}$ , where the underlined digit varied. An additional 1 LSD uncertainty is consequently added. The total uncertainty in temperature is thus determined to be  $\pm 0.2$  °C.

The measurement accuracy of the  $\mu$ PR700 pressure indicator is listed in the manual as  $\pm 0.1\%$  of output [66]. An additional  $\pm 1$  LSD is added as the last significant digit varied during calibration procedures. The total uncertainty in recorded pressure is thus determined to be  $\pm 0.1\% \pm 0.1$  (in bar), as the pressure is displayed as  $XX.X$  on the Dynisco  $\mu$ PR700 pressure indicator.

### **3.3 Data acquisition and LabVIEW**

LabVIEW [67] is a graphical programming language, i.e., a program is constructed graphically rather than textually. LabVIEW is short for “Laboratory Virtual Instrumentation Engineering Workbench”, and the programming language in LabVIEW is referred to as ‘G’. It was originally developed to simplify the collection of data from laboratory instruments and processes through DAQ systems. Development has however increased its applications to include data processing/analysis, and process/instrument control. A LabVIEW program is called a virtual instrument (VI) [68, 69].

Data acquisition refers to the collection of data from a process to a computer interface. The data may further be analyzed, interpreted and stored [68, 69]. The data is gathered from sensors that are devices with the ability to convert physical properties into electrical signals [70].

A new DAQ system was implemented as the hardware in the previous setup failed to work. A new computer has been installed with the latest version of LabVIEW along with new DAQ hardware with a USB connection (NI USB-6341). A new program for data logging has additionally been programmed. The programmed VIs are presented in Appendix B.3 along with a user procedure and an explanation.

The West 8100 controller and the Dynisco  $\mu$ PR700 pressure indicator are connected to the DAQ hardware (NI-USB6341). The DAQ device serves as a bridge between the sensors and the computer interface. The DAQ device receives voltage signals that represent the physical phenomena's that are monitored during the experiments. These voltage values are converted through the programmed VI, where they subsequently are stored.

Converting the voltage values to sensible units were done by measuring the sensor output to several constant values of the physical phenomena's displayed on the indicators (temperature and pressure). The temperature was controlled through the cooling cabinet by selecting a temperature, and the sensor output was subsequently measured after the temperature of the hydrate cell had stabilized for a number of hours. Similarly, the pressure values were measured by adding gas to the hydrate cell, where a set of stabilized pressure values was selected as calibration points.

The sensor output values were logged through LabVIEW where a simple VI was constructed with a sampling frequency of 1 Hz (1 sample every second). The VI ran for approximately 30 minutes for each calibration point. The average of the voltage measurements was set as the voltage value for that particular calibration point. Calibration curves for pressure and temperature is displayed in Fig. 3.7 and Fig. 3.8 respectively.

These measurements were additionally incorporated into the programmed logging VI for hydrate experiments, and as such convert measured voltages for pressure and temperature in real time, to sensible units in bar and  $^{\circ}\text{C}$ .

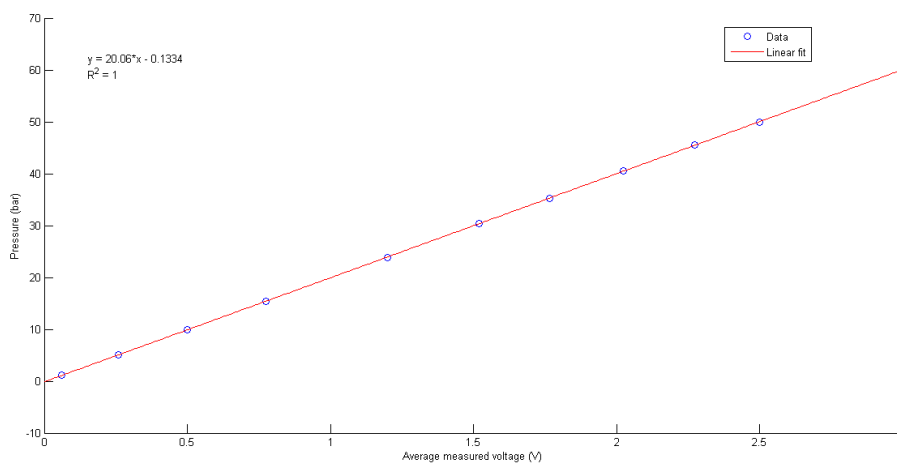


Figure 3.7: The linear relationship between average measured voltage and pressure established to convert voltage data from the pressure sensor to bar.  $y = 20.06x - 0.1334$ , where  $y$  is the pressure in bar, and  $x$  is the average measured voltage (V).

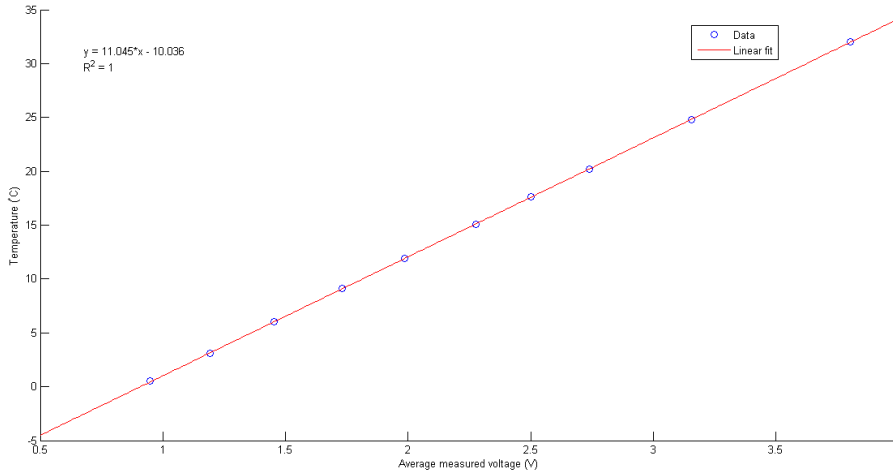


Figure 3.8: The linear relationship between average measured voltage and temperature established to convert voltage data from the temperature sensor to °C.  $y = 10.045x - 10.036$ , where  $y$  is the temperature in °C, and  $x$  is the average measured voltage (V).

It should specifically be noted that the pressure of some of the experiments exceeds the range of the calibration curve. The pressure has been calibrated to a maximum of 50.0 bar. This is due to the CO<sub>2</sub> regulator valve that has a limit of approximately 50.0 bar. However, as pressure transducers almost always produce an output that is linear to the pressure applied, an argument could be made that additional calibration points would not change the calibration curve. The 10 calibration points measured additionally have a correlation which approximately equals 1. It can also be stated that the pressure and temperature conditions for hydrate formation/dissociation falls within the calibration curve range.

The pressure and temperature data that is recorded through the LabVIEW VI is saved to the computer hard drive as an .lvm file. This file may subsequently be converted to a .txt file which can be read by software such as Excel or MATLAB. The software of choice for data analysis in this thesis is MATLAB. The pressure and temperature units of choice are MPa and Kelvin. The recorded values in bars and Celsius have consequently been converted through MATLAB.

### 3.4 Gas chromatography

Gas chromatography (GC) was the analytical method utilized to determine the composition of the binary CO<sub>2</sub>-CH<sub>4</sub> feed gas mixture. The gas samples were analyzed with a Gasphase GC HP 6890 apparatus.

There are two columns in the GC, with the dimensions listed in parenthesis (length/diameter/inner diameter): A Molsieve Plot (30 m/0.53 mm/50 μm) and a Plot Q (30 m/0.53 mm/40 μm). It additionally has a TCD detector (detects H<sub>2</sub> and O<sub>2</sub>) and a FID detector with a nickel catalyst (detects CO<sub>2</sub>, CO, CH<sub>4</sub>, C<sub>2</sub>H<sub>6</sub>, C<sub>3</sub>H<sub>8</sub> and C<sub>3</sub>H<sub>10</sub>). The gas sample is injected through a sampling loop at the back, where the volume introduced into the column through the gas-sampling loop is 250 μl [71].

The following temperature program was utilized: Initial temperature at 50 °C for 9 minutes. Heating at 5 °C per minute to 85 °C. Heating at 20 °C per minute to 180 °C, where 180 °C were employed for 5 minutes. The FID detector temperature was 300 °C and the TCD detector temperature was 200 °C. The injector temperature (back inlet) was 200 °C [71]. Retention times and peak areas were registered by the Chromeleon software [72].

To determine the unknown composition a calibration curve for each component was prepared from a calibration gas mixture. The calibration gas mixture had a composition of 2.00% CO<sub>2</sub>, 2.50% CH<sub>4</sub>, 15% O<sub>2</sub>, with the rest as balanced N<sub>2</sub>. N<sub>2</sub> is the carrier gas in the GC apparatus and is consequently not detected. O<sub>2</sub> does not influence the retention times of CO<sub>2</sub> and CH<sub>4</sub>.

A gas syringe (60 ml) was utilized to extract accurate samples for each calibration point. Calibration points were determined for volumes 50, 40, 30, 20 and 10 ml. A 50 ml calibration volume only contained calibration gas, whereas the other volumes were diluted to a total of 50 ml with N<sub>2</sub>. At least two parallels were analyzed for each composition where the average was set as the calibration point for that composition. The RD% was less than 5% between two parallels.

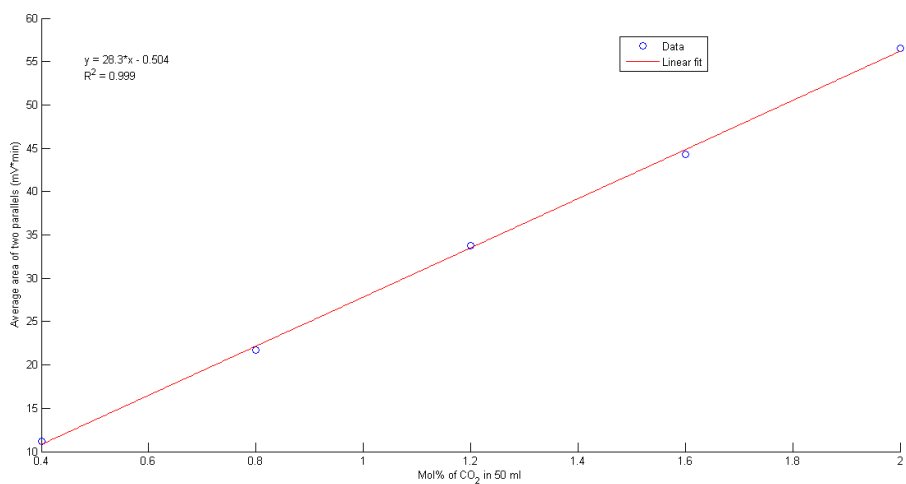


Figure 3.9: GC calibration curve for CO<sub>2</sub>.  $y = 28.3x - 0.504$ , where y is the average area registered for two parallels (mV\*min), and x is the mol% of CO<sub>2</sub> in 50 ml.

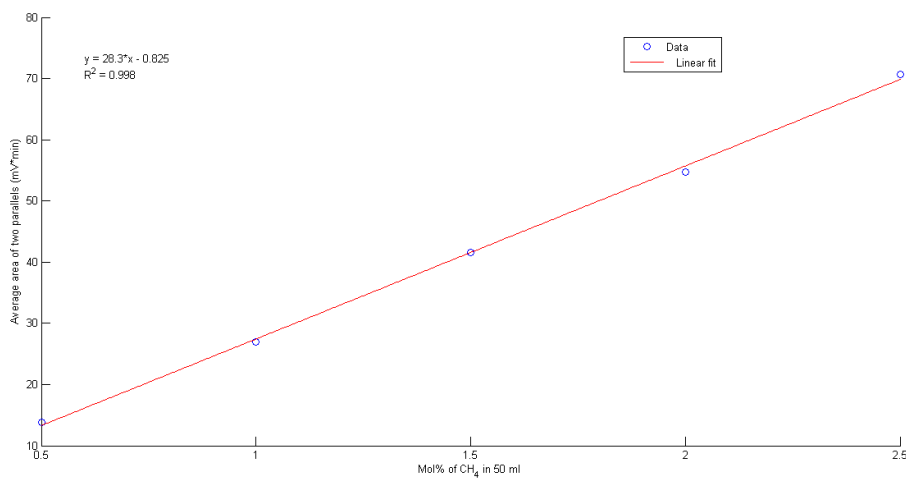


Figure 3.10: GC calibration curve for CH<sub>4</sub>.  $y = 28.3x - 0.825$ , where y is the average area registered for two parallels (mV\*min), and x is the mol% of CH<sub>4</sub> in 50 ml.



### 3.5 Experimental procedures for the hydrate cell at UiB

After each hydrate experiment, water was released through valve 2 by coupling an air compressor to valve 1 (Fig 3.1). After the cell had been emptied, all valves were closed for at least 30 minutes. The compressor was then utilized to flush any residual water left in the system, using the same procedure.

The compressor was also utilized to create vacuum in the hydrate cell before each experiment, which subsequently was utilized to introduce water in the system. The amount of distilled water for each experiment was measured in an appropriate volumetric flask. The mass was determined with a measurement error of  $\pm 0.001$  g.

#### Gas injection – simple hydrate experiments (See Fig. 3.1):

- When introducing gas into the cell, valve 1, 2, and 4 were closed.
- The stop valve on top of the gas flask was opened, and the regulator valve was opened.
- After the desired pressure was reached, valve 3 was closed.

#### Gas injection – mixed hydrate experiments (See Fig. 3.1):

- The procedure for gas injection for the mixed hydrate experiments was more comprehensive. CO<sub>2</sub> was initially injected into the cell, with the same procedure as described for the simple hydrate experiments. The pressure of the gas introduced into the cell was controlled by the regulator valve.
- Valve 3 was subsequently closed to contain the gas in the hydrate cell. The residual gas in the Swagelok tubing was released through valve 4 into the fume cabinet.
- The tubing was thereafter coupled to the CH<sub>4</sub> gas cylinder. The stop valve and the regulator valve were subsequently opened, letting the Swagelok tubing fill with CH<sub>4</sub>.
- As the pressure outside is larger than the interior of the cell. Valve 3 could then be opened, with CH<sub>4</sub> subsequently flowing into the cell.
- After injecting both components, the cell was closed and the stirring motor ran for approximately 1 minute. It was then assumed that the components was thoroughly mixed. The mixing was limited to 1 minute to minimize any error when sampling the gas mixture, as a large amount of dissolved CO<sub>2</sub> species would result in a less accurate determination of the vapor composition, and ultimately the system composition.

The mixed gas was sampled by coupling a 60 ml syringe to valve 1 by using suitable tubing. The syringe was initially flushed with N<sub>2</sub>. A 60 ml sample was withdrawn from the hydrate cell, which was subsequently diluted to a 1:60 ml ratio with N<sub>2</sub>. Any larger ratio of mixed gas to solvent gas resulted in cutoffs of the chromatogram peaks due to the sensitivity of the GC apparatus. This is again due to the high concentration of the gas components (Table 3.1).

For the mixed CO<sub>2</sub>-CH<sub>4</sub> hydrate experiments, the analyzed gas samples displayed only peaks for the first gas introduced into the cell in the resulting chromatogram. The GC apparatus was rechecked with several calibration samples and pure gas samples. Peaks for both gases were observed in the chromatograms. It was subsequently assumed that there was “dead-volume” in the stirring part of the cell. The first gas that is introduced into the cell occupies this volume and consequently does not mix with the rest of the gas in cell. There was gradual diffusion over time, as gas samples analyzed several hours later (+24h) indicated the presence of the second gas introduced.

To determine the magnitude of the “dead-volume”, gas samples were extracted and analyzed until a peak for the second gas introduced into the hydrate cell was observed in the chromatogram. 60 ml samples were withdrawn from the cell. The pressure of the hydrate cell was known; the magnitude of the “dead-volume” could then be approximately quantified. For example, if the pressure in the hydrate cell was 60.0 bar, a 60 ml sample at 1.0 bar is the equivalent of 1 ml in the pressurized system. As feared, the “dead-volume” was of a significant magnitude, where the presence of the second gas was not discovered until several samples had been analyzed.

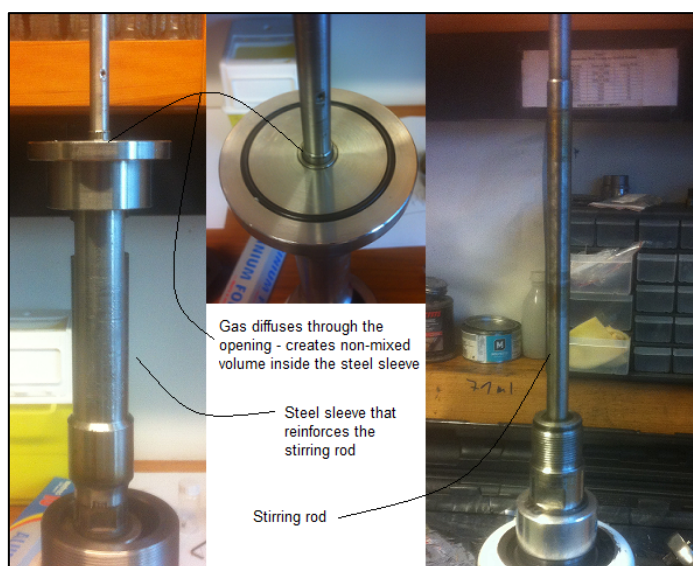


Figure 3.11: Location of the “dead-volume”.

The hydrate cell was subsequently disassembled, where it was discovered that the “dead-volume” was located between the stirring rod that goes through the hydrate cell top cap, and the sleeve that reinforces the stirring rod and connects the top cap to the hydrate cell. Gas escapes up the sleeve through the small opening in which the stirrer goes through (Fig. 3.11).

A gas and oil resistant O-ring was placed between the stirrer and the sleeve, but with no observable effect. The O-ring was removed, and the stirrer was again reassembled. A large gas leak was subsequently observed from the joint where the two components are connected.

Several unsuccessful efforts were put into disconnecting the two components. An effort to seal the gas leak was additionally performed. High-grade epoxy was injected into the opening, which worked at low pressures, but could not withstand high pressures. The joint was finally welded, gas however escaped from small pores in the weld. Further welding did not improve its condition, and additional experiments could consequently not be performed.

### 3.6 Description of experiments performed at Statoil

The experimental setup utilized for the hydrate experiments at Statoil has been extensively described elsewhere [73, 74].

The main part of the setup is a cylindrical cell connected to an adjustable piston. A section of the cell is made of sapphire which allows for a visual observation of the system during experiments. The maximum volume of the cell is approximately  $100 \text{ cm}^3$ , which can be reduced by adjusting the piston. A stirrer connected to the piston allows for thorough agitation of the system. A computer controls the entire setup and records data during experiments. The uncertainty in relevant variables are as follows:  $\pm 0.1 \text{ K}$  in temperature,  $\pm 0.05 \text{ MPa}$  in pressure, and  $\pm 0.005 \text{ cm}^3$  in volume [73].

A gas mixture was prepared in a sample gas cylinder by injecting high purity  $\text{CO}_2$ - and  $\text{CH}_4$  separately. The volume of each gas introduced could be accurately determined by measuring the amount of water displaced from the sample cylinder. The composition of the gas mixture was calculated to 90%  $\text{CO}_2$  and 10%  $\text{CH}_4$ , which was additionally confirmed by GC analysis.

14 ml deionized  $\text{H}_2\text{O}$  was injected into the sapphire cell by means of a vacuum. The gas mixture was subsequently injected by utilizing a pump. Gas injection was stopped when the desired system volume was reached, and the cell was subsequently closed. The same fluid was utilized for the three experiments performed – nothing was added or removed from the cell in-between experiments. All experiments consequently have the same system composition.

The three experiments were performed at isobaric conditions, at approximately 7.7- and 7.0 MPa respectively. Experiment B is a parallel experiment of experiment A (both at approximately 7.7 MPa). Results from the experiments are presented in Section 4.4, with a subsequent discussion in Section 5.4.

# CHAPTER 4: RESULTS

## 4.1. PVTsim simulations of the CO<sub>2</sub>-CH<sub>4</sub>-H<sub>2</sub>O system

### 4.1.1 Ternary phase diagrams

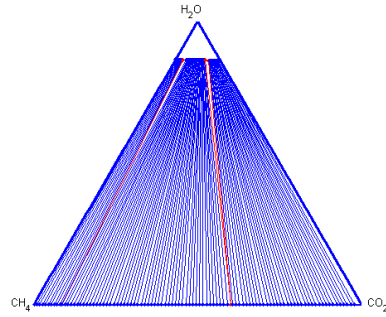
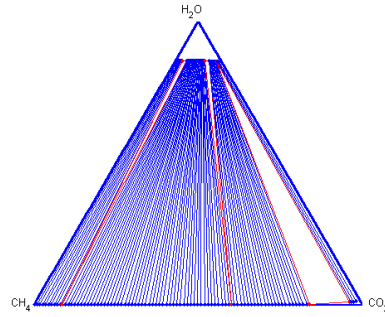
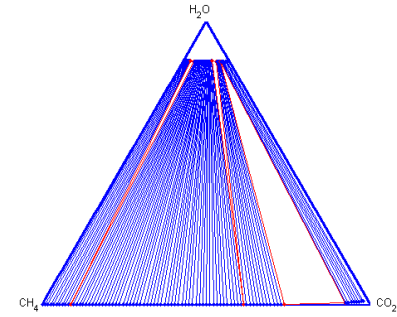
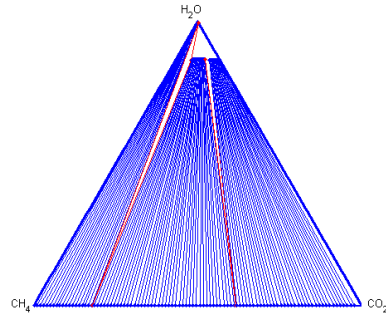
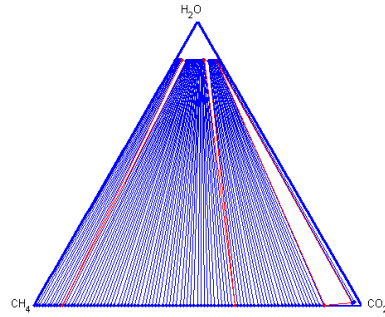
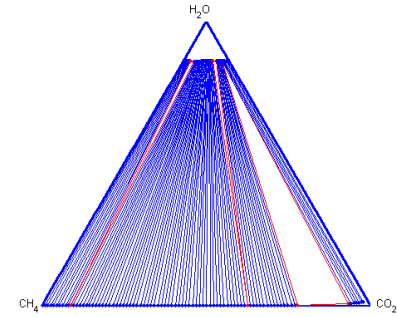
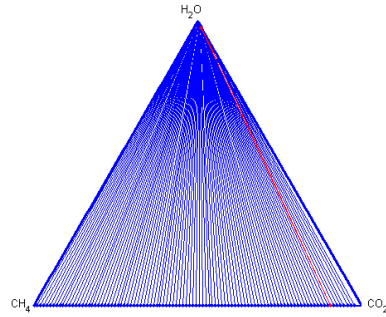
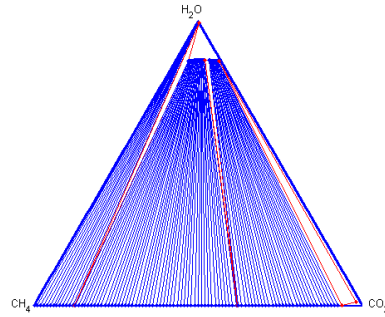
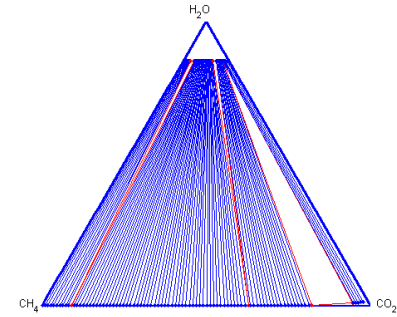
Figure 4.1 and 4.2 presents several ternary phase diagrams for the CO<sub>2</sub>-CH<sub>4</sub>-H<sub>2</sub>O system at various isothermal and isobaric conditions.

The previously mentioned Open Structure MATLAB script was utilized to simulate the ternary phase diagrams. Results from both the SRK EOS and the PR EOS are presented as a significant difference in phase predictions was observed between them.

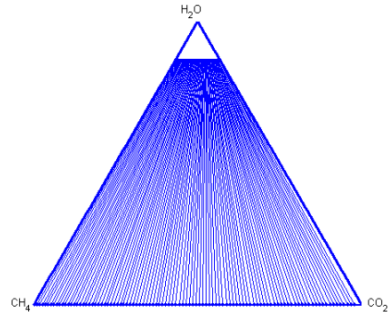
Blue tie lines connect two-phases in equilibrium, and red tie lines connect a three-phase equilibrium area. Aqueous phases ( $L_w$ ) that are located at the top of the ternary phase diagrams (H<sub>2</sub>O vertex) are usually not predicted due to the high gas content (CO<sub>2</sub>/CH<sub>4</sub>) in the original fluid used for the simulations (50% of total). A fluid with a higher H<sub>2</sub>O content would however predict the upper part of the ternary phase diagram. Three phase  $L_w$ -H-V equilibria are however observable in d), g) and h) in both figures.

The SRK EOS predicts a structural transition from sI to sII hydrate. This structural transition may be observed in Fig. 4.1 as the three-phase areas where two hydrate phases are in equilibrium with a vapor phase (sI-sII-V equilibria). SRK subsequently predicts sII hydrates at various CO<sub>2</sub>/CH<sub>4</sub> ratios following this area. The structure shifts back to sI again at high CO<sub>2</sub> concentrations, and sI hydrates are subsequently predicted. The structural transitions are also observed for systems modeled with a high H<sub>2</sub>O content, although with an aqueous phase ( $L_w$ ) instead of a vapor phase. This structural transition is not observed in predictions from the PR EOS, which predicts sI hydrates for all CO<sub>2</sub>/CH<sub>4</sub> ratios, which is evident in Fig. 4.2.

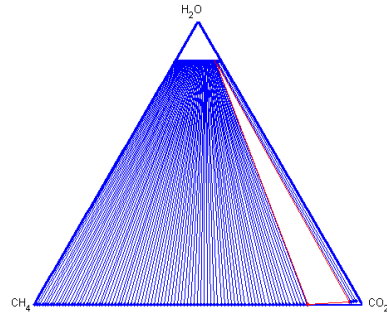
A third three-phase area is additionally observed in some of the ternary phase diagrams predicted in Fig. 4.1. at high CO<sub>2</sub> concentrations. These three-phase areas represent a hydrate-vapor-liquid equilibria, where the liquid phase mainly consist of CO<sub>2</sub>. These three-phase areas are also observed in the ternary diagrams predicted by the PR EOS in Fig. 4.2.

a)  $T = 274 \text{ K}$  and  $P = 3.0 \text{ MPa}$ b)  $T = 274 \text{ K}$  and  $P = 4.5 \text{ MPa}$ c)  $T = 274 \text{ K}$  and  $P = 5.5 \text{ MPa}$ d)  $T = 277 \text{ K}$  and  $P = 3.0 \text{ MPa}$ e)  $T = 277 \text{ K}$  and  $P = 4.5 \text{ MPa}$ f)  $T = 277 \text{ K}$  and  $P = 5.5 \text{ MPa}$ g)  $T = 280 \text{ K}$  and  $P = 3.0 \text{ MPa}$ h)  $T = 280 \text{ K}$  and  $P = 4.5 \text{ MPa}$ i)  $T = 280 \text{ K}$  and  $P = 5.5 \text{ MPa}$ Figure 4.1: Ternary phase diagrams for the  $\text{CO}_2\text{-CH}_4\text{-H}_2\text{O}$  system. SRK EOS utilized for the simulations in PVTsim.

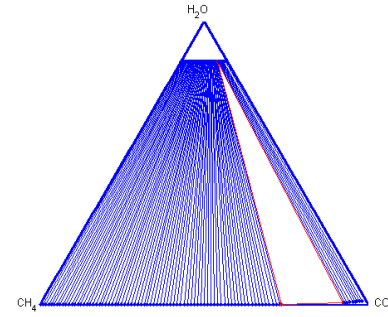
a)  $T = 274 \text{ K}$  and  $P = 3.0 \text{ MPa}$



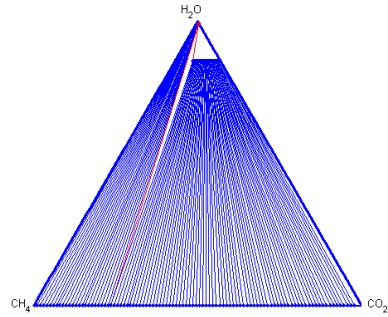
b)  $T = 274 \text{ K}$  and  $P = 4.5 \text{ MPa}$



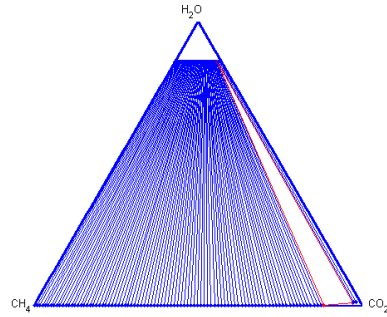
c)  $T = 274 \text{ K}$  and  $P = 5.5 \text{ MPa}$



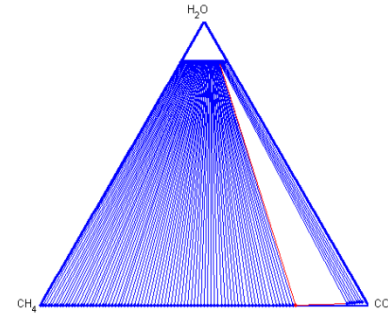
d)  $T = 277 \text{ K}$  and  $P = 3.0 \text{ MPa}$



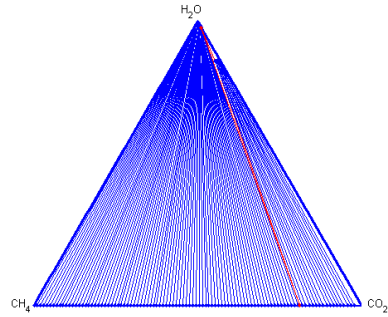
e)  $T = 277 \text{ K}$  and  $P = 4.5 \text{ MPa}$



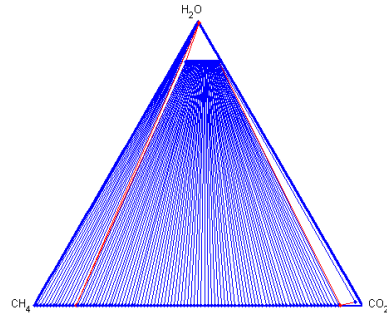
f)  $T = 277 \text{ K}$  and  $P = 5.5 \text{ MPa}$



g)  $T = 280 \text{ K}$  and  $P = 3.0 \text{ MPa}$



h)  $T = 280 \text{ K}$  and  $P = 4.5 \text{ MPa}$



i)  $T = 280 \text{ K}$  and  $P = 5.5 \text{ MPa}$

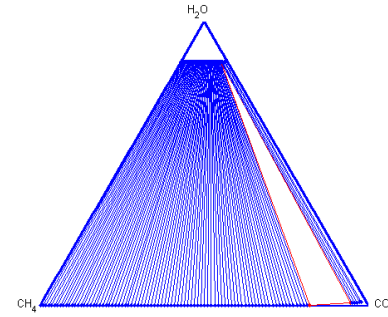


Figure 4.2: Ternary phase diagrams for the  $\text{CO}_2\text{-CH}_4\text{-H}_2\text{O}$  system. PR EOS utilized for the simulations performed in PVTsim.

A series of manual hydrate flashes are presented based upon the same pressure and temperature conditions, and within the same compositional range as in Fig. 4.1 and Fig. 4.2. The fluid compositions utilized for the simulations are listed in Table A.1.1 in Appendix A. The same fluid compositions utilized for SRK simulations were also utilized for PR simulations to examine the compositional phase predictions difference between them. The H<sub>2</sub>O content is not listed in Table A.1.1 as it is fixed at 50% for all fluids.

For the SRK EOS the fluid composition where the first sign of a sI/sII structural transition was observed, was determined to three decimal places for the various isothermal and isobaric conditions chosen. This was to determine if the pressure and temperature conditions had any influence on the structural transition observed, or if it was mainly a result of the composition. These are presented in Table 4.1 below.

Table 4.1: Determined fluid composition that yields structural transitions in the ternary CO<sub>2</sub>-CH<sub>4</sub>-H<sub>2</sub>O system simulated in PVTsim with the SRK EOS. Water content fixed at 50%.

<b>274 K and 3.0 MPa</b>		<b>274 K and 4.5 MPa</b>		<b>274 K and 5.5 MPa</b>		<b>Transition</b>
<u>CO<sub>2</sub></u>	<u>CH<sub>4</sub></u>	<u>CO<sub>2</sub></u>	<u>CH<sub>4</sub></u>	<u>CO<sub>2</sub></u>	<u>CH<sub>4</sub></u>	
4.842	45.158	4.877	45.123	4.894	45.106	sI to sII
30.559	19.441	30.393	19.607	30.865	19.135	sII to sI
<b>277 K and 3.0 MPa</b>		<b>277 K and P = 4.5 MPa</b>		<b>277 K and 5.5 MPa</b>		
<u>CO<sub>2</sub></u>	<u>CH<sub>4</sub></u>	<u>CO<sub>2</sub></u>	<u>CH<sub>4</sub></u>	<u>CO<sub>2</sub></u>	<u>CH<sub>4</sub></u>	
First hydrate is sII		4.924	45.076	4.957	45.043	sI to sII
31.274	18.726	30.982	19.018	31.388	18.612	sII to sI
<b>280 K and 3.0 MPa</b>		<b>280 K and 4.5 MPa</b>		<b>280 K and 5.5 MPa</b>		
<u>CO<sub>2</sub></u>	<u>CH<sub>4</sub></u>	<u>CO<sub>2</sub></u>	<u>CH<sub>4</sub></u>	<u>CO<sub>2</sub></u>	<u>CH<sub>4</sub></u>	
Last hydrate is sI		First hydrate is sII		5.066	44.934	sI to sII
		31.160	18.840	31.494	18.506	sII to sI

Figure 4.3 presents the mole fraction of CO<sub>2</sub> in the vapor phase ( $y_{CO_2}$ ) calculated by Eq.(2.11) from the compositional vapor phase predictions by PVTsim. Figure 4.4 presents the mole fraction of CO<sub>2</sub> in the hydrate phase ( $z_{CO_2}$ ) calculated by Eq.(2.12) from the compositional hydrate phase predictions by PVTsim. Predictions from both the PR EOS and the SRK EOS are presented in the figures. Figure 4.5 and 4.6 presents an example of the simulated CO<sub>2</sub>-CH<sub>4</sub>-H<sub>2</sub>O system at 274 K and 3.0 MPa, with phase compositions predicted from PVTsim plotted.



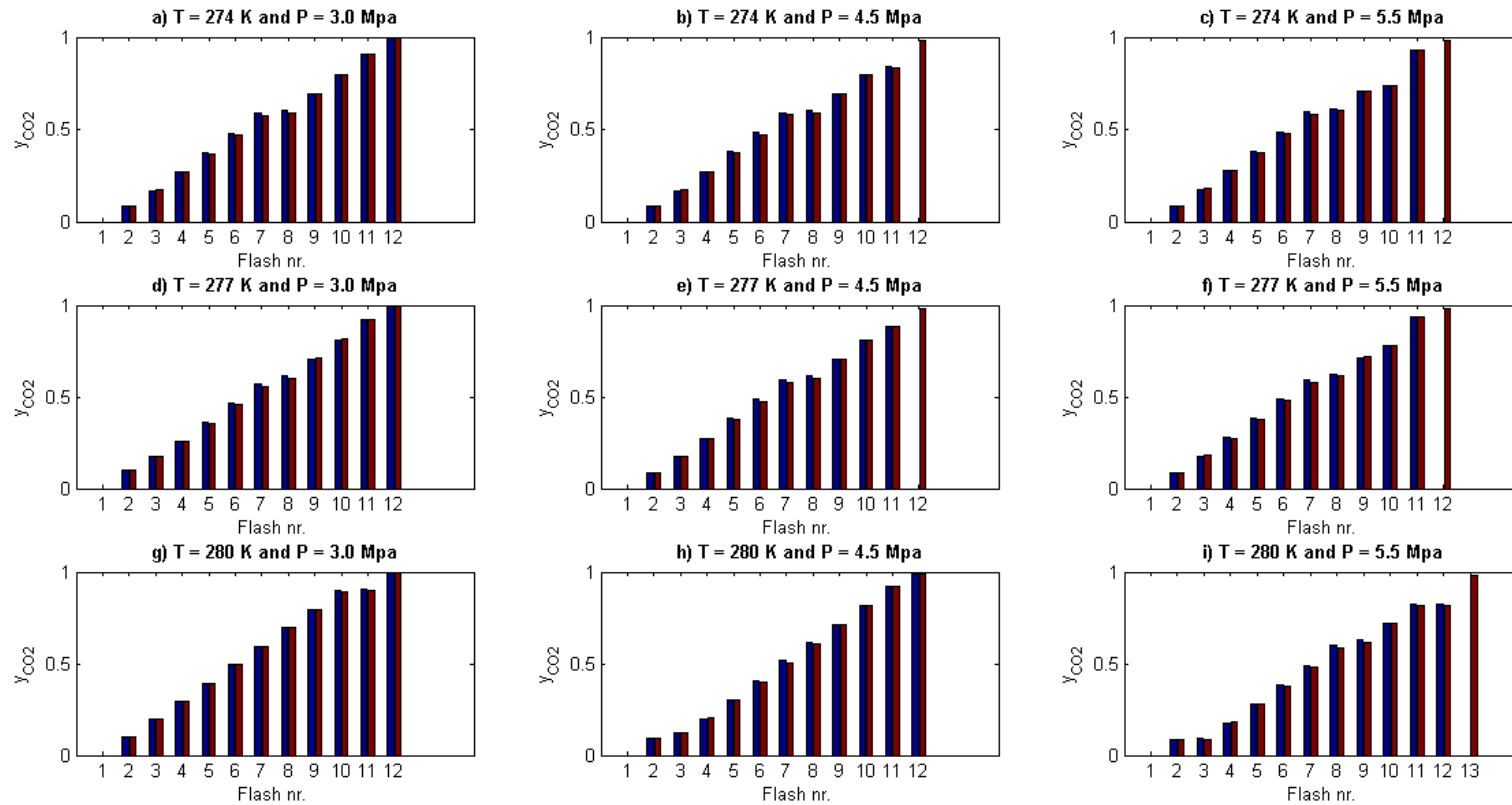


Figure 4.3: Fraction of CO<sub>2</sub> in the vapor phase ( $y_{CO_2}$ ), calculated from vapor phase predictions by PVTsim by Eq.(2.11). The blue bars represent predictions with the SRK EOS, and the red bars represent predictions with the PR EOS. The x-axis ticks on the bar graphs is the sequence number of the fluids listed in Table A.1.1. Tick number 1 on the x-axis in Figure 4.3 a) is correspondingly the first fluid composition listed in Table A.1.1 under sub-table a). The gradual increase of CO<sub>2</sub> in the vapor phase is due to more CO<sub>2</sub> being “added” for each flash in the sequence. Calculated and plotted values for  $y_{CO_2}$  is listed in table A.1.2.

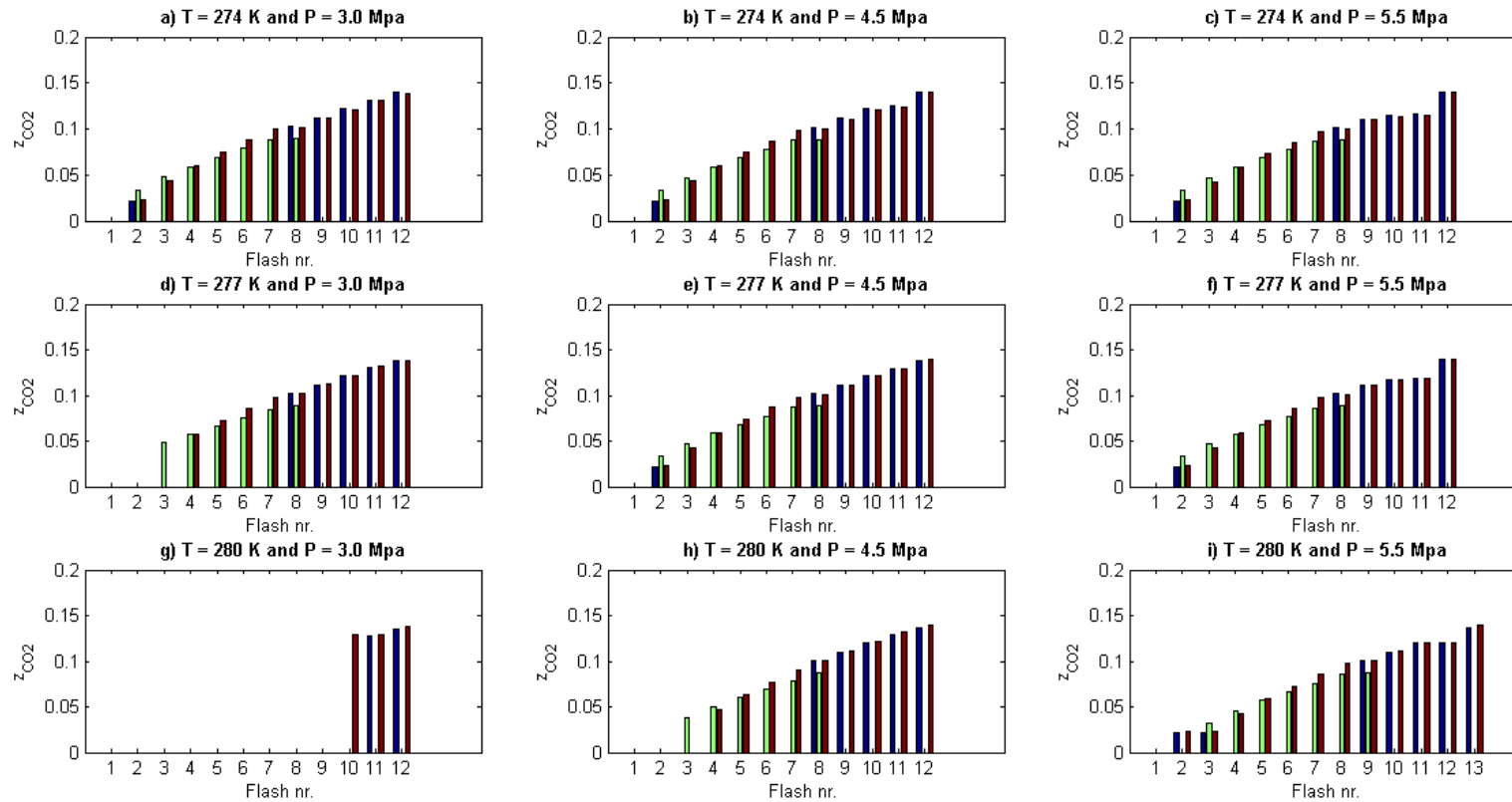


Figure 4.4: Fraction of CO<sub>2</sub> in the hydrate phase ( $z_{CO_2}$ ), calculated from hydrate phase predictions by PVTsim by Eq.(2.12). The blue bars represent structure I compositional predictions with the SRK EOS, the green bars represent structure II compositional predictions with the SRK EOS, and the red bars represent sI compositional predictions with the PR EOS. The x-axis ticks on the bar graphs is the sequence number of the fluids listed in Table A.1.1. Tick number 1 on the x-axis in Figure 4.4 a) is correspondingly the first fluid composition listed in Table A.1.1 under sub-table a). The gradual increase of CO<sub>2</sub> in the hydrate phase is due to more CO<sub>2</sub> being “added” for each flash in the sequence. Calculated and plotted values for  $z_{CO_2}$  are listed in Table A.1.3.

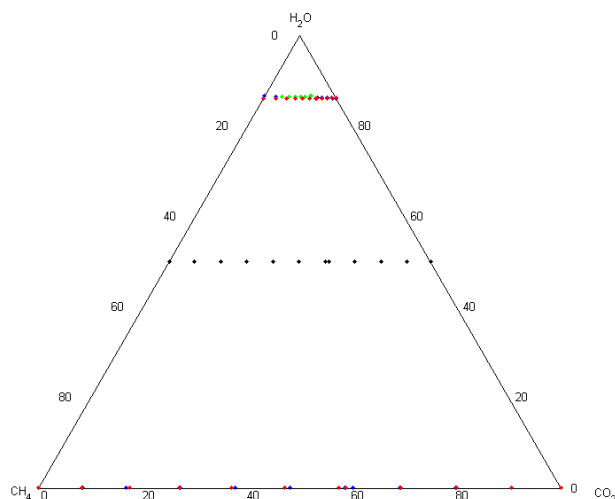


Figure 4.5: The ternary  $\text{CO}_2\text{-CH}_4\text{-H}_2\text{O}$  system simulated at 274 K and 3.0 MPa. The black dots represent the fluid compositions utilized for the Hydrate PT flash (listed in a) in Table A.1.1). Blue, green and red dots located near the  $\text{H}_2\text{O}$  apex are phase compositions predicted in PVTsim for sI hydrate (SRK), sII hydrate (SRK), and sI hydrate (PR) respectively. Blue and red dots located on the opposite end of the diagram are vapor phase compositions, predicted utilizing SRK and PR respectively. Tie lines have been omitted for simplicity.

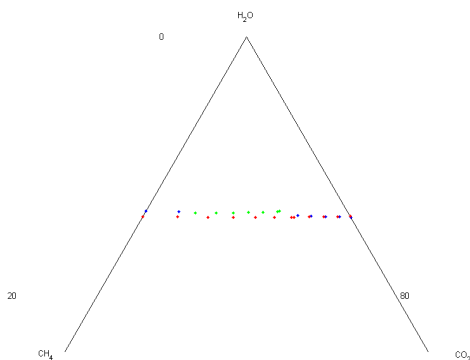


Figure 4.6: Zoomed in part of the  $\text{H}_2\text{O}$  apex in Fig. 4.5.

SRK predicted a higher water content in the hydrate phase than PR. The difference is somewhat higher when SRK predicts sII hydrate, which may be observed in Table 4.2 below.

Table 4.2: Average water content in predicted hydrate structure by PVTsim.

EOS	# predictions	Average $\text{H}_2\text{O}$ fraction in the hydrate phase
PR	94	0.859
SRK <sup>sI</sup>	55	0.861
SKR <sup>sII</sup>	54	0.862

<sup>sI</sup> Structure I hydrate.

<sup>sII</sup> Structure II hydrate.

#### 4.1.2 PVTsim predictions compared with data from Belandria et al. (2011).

The study by Belandria et al. (2011) is the only discovered study that lists full system composition for all experiments [48]. This data have subsequently been used as a reference to examine the difference between the SRK EOS and the PR EOS, due to the observed difference between their respective structural predictions. The study lists 9 and 40 experimental points in two separate tables. The equilibrium conditions for the CO<sub>2</sub>-CH<sub>4</sub>-H<sub>2</sub>O system was determined by a pressure search method at isothermal conditions, which explains the several markers at constant temperature in Figure 4.7.

The deviation in temperature calculated by Eq.(2.6) is plotted against dissociation temperatures listed in the study in Fig. 4.7 to the left. The absolute deviation in temperature, calculated by Eq.(2.8) is plotted against the listed dissociation temperatures in Fig. 4.7 to the right.

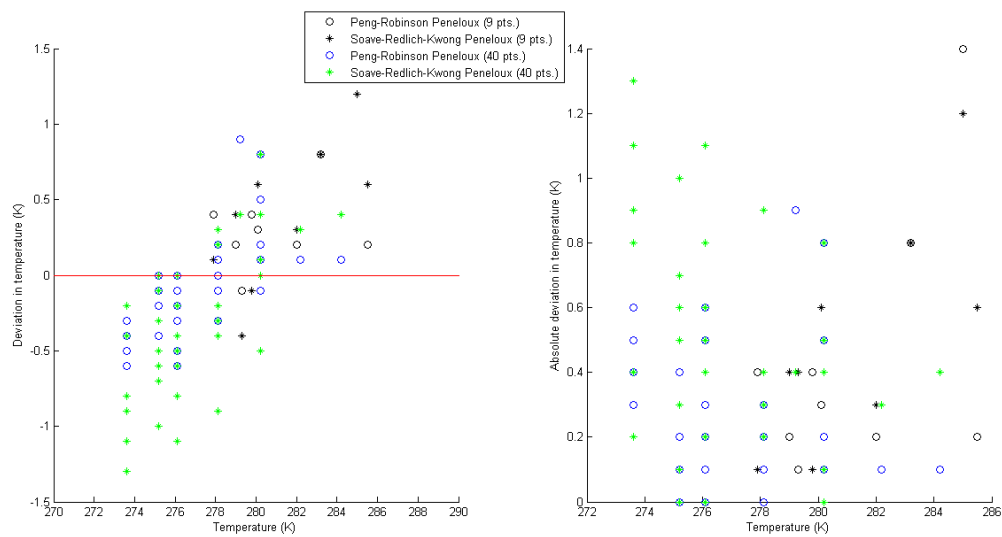


Figure 4.7: Deviation and absolute deviation in hydrate temperatures predicted by PVTsim utilizing the Hydrate Temp algorithm. Deviations are calculated with respect to listed dissociation temperatures in Belandria et al. (2011) [48]. Calculated deviations based upon predictions from PR are represented in the figure as circles, and calculated deviations based upon predictions from SRK are represented in the figure as asteriks.

The relative deviation in pressure calculated by Eq.(2.7) is plotted against dissociation pressures listed in the study to the left in Fig. 4.8. The absolute relative deviation in pressure calculated by Eq.(2.9) is plotted against the listed dissociation pressures to the right in Fig. 4.8.

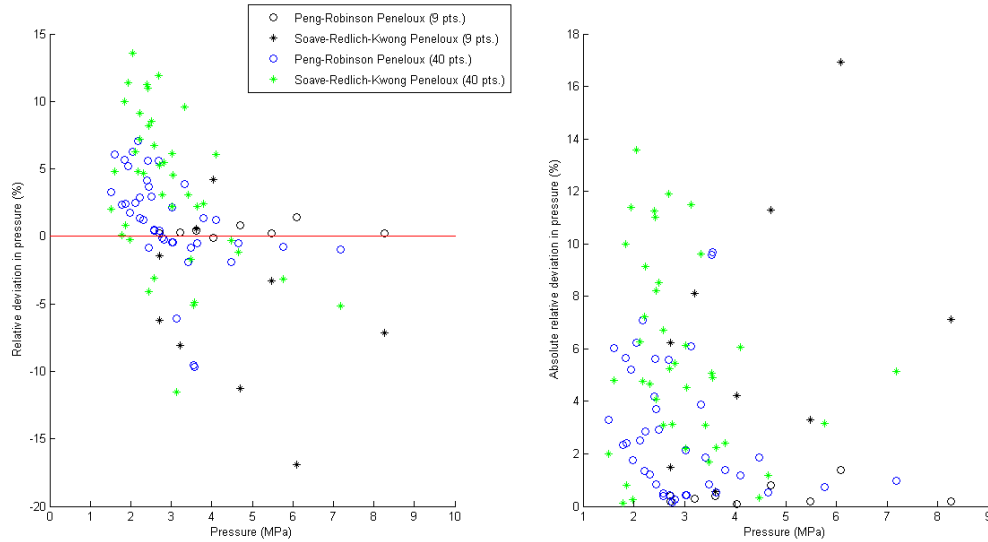


Figure 4.8: Relative deviation and absolute relative deviation in hydrate pressures predicted by PVTsim utilizing the Hydrate Pressure algorithm. Deviations are calculated with respect to listed dissociation pressures in Belandria et al. (2011) [48]. Calculated deviations based upon predictions from PR are represented in the figure as circles, and calculated deviations based upon predictions from SRK are represented in the figure as asteriks.

Table A.1.4 – A.1.7 lists the total system composition and dissociation conditions from the reference. Predicted temperature and pressure conditions from PVTsim utilizing both the PR EOS and the SRK EOS are also listed. Calculated deviations in temperature, absolute deviations in temperature, relative deviations in pressure, and absolute relative deviation in pressure is additionally listed.

Table 4.3 lists the average deviation in temperature ( $\bar{D} T$ ), the absolute average deviation in temperature ( $\bar{AD} T$ ), the average relative deviation in pressure ( $\bar{RD}\% P$ ), and the average absolute relative deviation in pressure ( $\bar{ARD}\% P$ ) for PVTsim predictions based upon listed dissociation conditions in the study by Belandria et al (2011) [48].

Table 4.3: Calculated average deviations in temperature and average relative deviations in pressure for PVTsim predictions with respect to listed dissociation conditions in Belandria et al. (2011) [48].

EOS	# of exp. pts.	$\bar{x}$ D T (K)	$\bar{x}$ AD T (K)	$\bar{x}$ RD% P	$\bar{x}$ ARD% P
PR	9	0.4	0.4	-5.53	5.64
SRK	9	0.4	0.5	-5.52	6.58
PR	40	-0.1	0.3	1.10	2.90
SRK	40	-0.3	0.5	3.55	5.57

$\bar{x}$  = average

The study by Belandria et al. (2011) additionally lists  $y_{CO_2}$ ,  $z_{CO_2}$ , and the full aqueous phase composition for 40 experiments [48]. The vapor phase composition was determined by GC analysis, while the hydrate and aqueous phase composition was determined through a material balance. The compositional data presented by Belandria et al. (2011) [48] has been compared with compositional predictions by PVTsim. Both PR and SRK have been utilized for predictions due to their difference in structural predictions. To compare the predicted phase composition with experimental values listed in the study, the Hydrate PT flash algorithm were utilized at listed dissociation conditions in the study (where the vapor phase was sampled).

The total system composition, PT conditions, and phase fractions listed by Belandria et al. (2011) is also listed in Table A.1.9. The authors lists  $y_{CO_2}$  and  $z_{CO_2}$ , on a “water free basis”, where they essentially exclude the  $H_2O$  content in the vapor and hydrate phase when determining the  $CO_2$  fractions in the respectable phases (Section 2.2.5). To compare the compositional phase predictions from PVTsim with listed compositional data in the reference, Eq.(2.14) and Eq.(2.15) has been utilized to determine fraction of  $CO_2$  in the hydrate and vapor phase respectively. The aqueous phase composition could however be compared directly as the reference lists the full aqueous phase composition.

There is a degree of uncertainty related to representing the fraction of  $CO_2$  in the hydrate phase by Eq.(2.15) as the  $H_2O$  content of the hydrate phase is not included in the calculations presented. It was established in the previous section that SRK generally predicts a higher  $H_2O$  content in the hydrate phase than PR (Table 4.2). A lower  $CO_2$  and  $CH_4$  content in the hydrate phase is consequently predicted, which has implications when comparing the two respective EOS's. The difference between the predicted  $H_2O$  content of the hydrate phase is however not very pronounced in regards to the two different EOS's. Even when accounting for the difference in the water content, a significant difference between sII compositional predictions for SRK, and sI compositional predictions for PR was observed.

Rows that contains (-) in Table A.1.9 is because of the reference not listing the value. Rows that contains (-) in Table A.1.10 is as a result of PVTsim not predicting the phase at the conditions listed in the reference.

Relative deviations (RD%) and absolute relative deviations (ARD%) with respect to experimental compositions listed in the reference, have been calculated by Eq.(2.16) and Eq.(2.17). These are presented in Table A.1.11 and Table A.1.12 in Appendix A.1, PR and SRK respectively. The deviations are plotted in Fig 4.9 against listed experimental values from Belandria et al. (2011) [48]. Table 4.4 additionally presents the averages of the absolute relative deviations.

Table 4.4: Average absolute deviations for compositional predictions from PVTsim with the PR EOS and the SRK EOS. The deviations are calculated with respect to compositional values listed in the study by Belandria et al. (2011) [48].

Row No.	EOS	ARD% Hydrate		ARD% Vapor		ARD% Aqueous			
		# points	$z_{CO_2}$	# points	$y_{CO_2}$	# points	$x_{H_2O}$	$x_{CO_2}$	$x_{CH_4}$
1	PR	22	18.2	39	11.4	36	0.2	30.9	44.9
2	SRK	26	28.1	30	10.2	36	0.3	37.4	43.6
3	PR	21 <sup>a</sup>	18.7	21 <sup>a</sup>	11.5	21 <sup>a</sup>	0.2	24.4	49.4
4	SRK	16 <sup>a</sup>	32.9	16 <sup>a</sup>	12	16 <sup>a</sup>	0.3	33.6	30.8
5	PR	7 <sup>b</sup>	20.1	7 <sup>b</sup>	12.5	7 <sup>b</sup>	0.2	26.6	22.6
6	SRK	7 <sup>b</sup>	47.1	7 <sup>b</sup>	9.2	7 <sup>b</sup>	0.3	38.8	32.2
7	PR	3 <sup>c</sup>	4	3 <sup>c</sup>	8.8	3 <sup>c</sup>	0.1	7.1	33.3
8	SRK	3 <sup>c</sup>	4.7	3 <sup>c</sup>	13.7	3 <sup>c</sup>	0.1	8.2	44.4

<sup>a</sup> L<sub>w</sub>-H-V equilibria predicted in PVTsim.

<sup>b</sup> L<sub>w</sub>-H-V equilibria where SRK predicts sII hydrate and PR predicts sI hydrate.

<sup>c</sup> L<sub>w</sub>-H-V equilibria where both PR and SRK predicts sI hydrate.

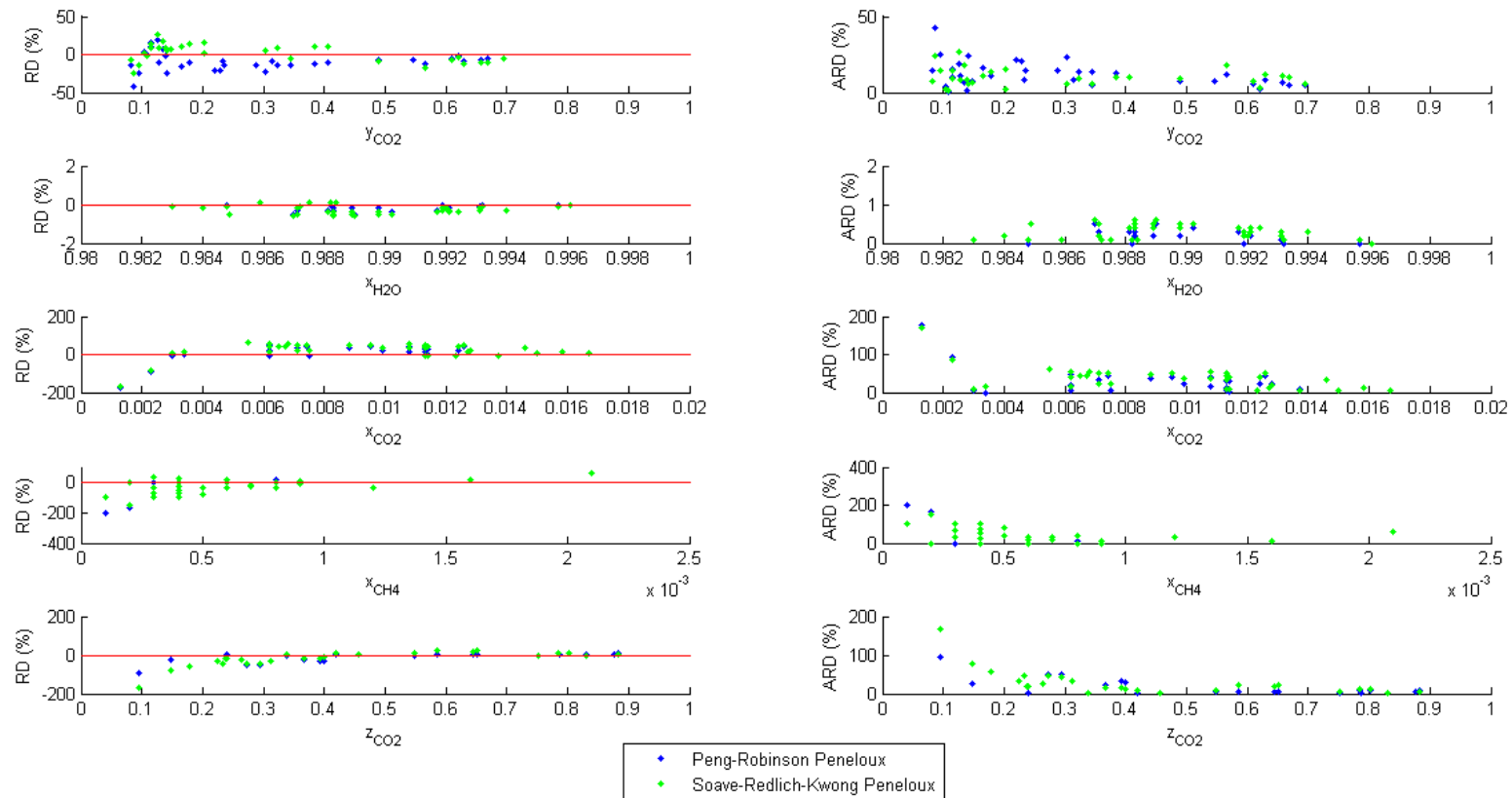


Figure 4.9: Calculated RD% and ARD% plotted against experimental compositional values listed in Belandria et al. (2011) [48].  $y_{CO_2}$  is the mole fraction of  $CO_2$  in the vapor phase determined by Eq.(2.14).  $x_{H_2O}$ ,  $x_{CO_2}$  and  $x_{CH_4}$  are mole fractions of each component in the aqueous phase.  $z_{CO_2}$  is the mole fraction of  $CO_2$  in the hydrate phase determined by Eq.(2.15). Blue points are deviations calculated from phase predictions utilizing the PR EOS, and green points are deviations calculated from predictions utilizing the SRK EOS.



## 4.2 Accuracy of PVTsim predictions

### 4.2.1 Simple CO<sub>2</sub> and CH<sub>4</sub> hydrates

For a visual comparison of the accuracy of PVTsim for simple CO<sub>2</sub> and CH<sub>4</sub> hydrates, experimental equilibrium data has been selected from Sloan and Koh (2008) [4], and plotted with predicted PT curves from PVTsim. The exact water to hydrate former ratio is approximated. PT curves predicted by PVTsim is generally the same regardless of the water amount in the system, except at extremely low or high water amounts (>97% or <3%).

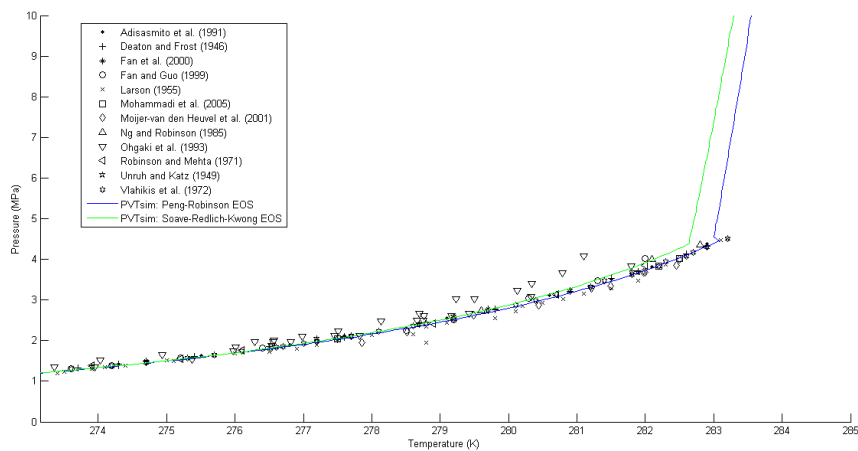


Figure 4.10: Comparison of predicted PT curves by PVTsim with measured L<sub>w</sub>-H-V equilibrium conditions for CO<sub>2</sub> hydrate. Selected data from Sloan and Koh (2008) below 10.0 MPa and above the freezing point of H<sub>2</sub>O. Original source is listed in the legend.

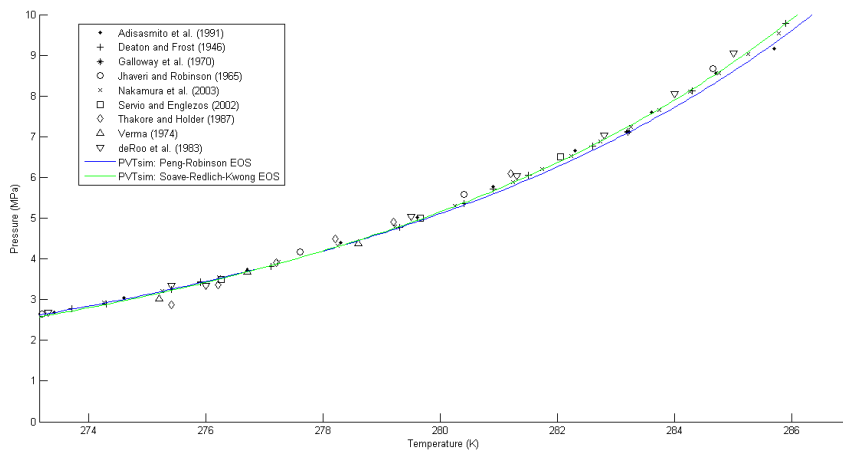


Figure 4.11: Comparison of predicted PT curves by PVTsim with measured L<sub>w</sub>-H-V equilibrium conditions for CH<sub>4</sub> hydrate. Selected data from Sloan and Koh (2008) below 10.0 MPa and above the freezing point of H<sub>2</sub>O. Original source is listed in the legend.

#### 4.2.2 Mixed CO<sub>2</sub>-CH<sub>4</sub> hydrates

Of the listed studies on hydrates formed from a binary CO<sub>2</sub>-CH<sub>4</sub> gas mixture, the following studies have been examined to determine the accuracy of PVTsim predictions: Adisasmito et al. (1991) [38], Belandria et al. (2010) [47], Belandria et al. (2011) [48], Beltran and Servio (2008) [45], Dholabhai et al. (1994) [39], Fan and Guo (1999) [42], Seo et al. (2001) [43], and Unruh and Katz (1949) [37].

Fluid inputs in PVTsim has been approximated based upon information listed in each study with the presence of dissolved species being neglected (Section 2.2.4). The PR EOS has been utilized for estimating both the total system composition and formation conditions.

Estimated system compositions and calculated deviations with respect to dissociation conditions from the respective studies are listed in Appendix A.2. Average deviations in temperature (D T), average absolute deviations in temperature (AD T), average relative deviations in pressure (RD% P), and average absolute deviations in pressure (ARD% P) for each study are presented in Table 4.5. The weighted average has additionally been determined for the deviations presented.

Table 4.5: Calculated deviations and relative deviations in temperature and pressure to determine the predictive ability of PVTsim. The deviations have been calculated with respect to measured dissociation conditions for the CO<sub>2</sub>-CH<sub>4</sub>-H<sub>2</sub>O system from the literature.

<b>Reference:</b>	<b># exp. pts.</b>	<b>D T (K)</b>	<b>AD T (K)</b>	<b>RD% P</b>	<b>ARD% P</b>
Adisasmito et al. (1991)	42	0.2	0.4	-2.19	4.59
Belandria et al. (2010)	11	0.6	0.6	-8.39	9.13
Belandria et al. (2011)*	9	0.4	0.4	-5.53	5.64
Belandria et al. (2011)*	40	-0.1	0.3	1.10	2.90
Beltran and Servio (2008)	12	0.78	0.78	-9.42	9.42
Fan and Guo (1999)	9	0.4	0.7	-4.20	8.97
Seo et al. (2001)	8	0.25	0.32	-4.80	4.80
Unruh and Katz (1949)	17	0.5	0.6	-6.70	7.72
Dholabhai and Bishnoi (1994)	4	0.20	0.22	-2.17	2.44
<b>Weighted average:</b>		<b>0.3</b>	<b>0.4</b>	<b>-3.31</b>	<b>5.49</b>

\* Two sets of equilibrium measurements are listed in the study.

Figure 4.12 and 4.13 presents deviations in temperature and relative deviations in pressure respectively, plotted against the respective dissociation conditions listed in the studies.

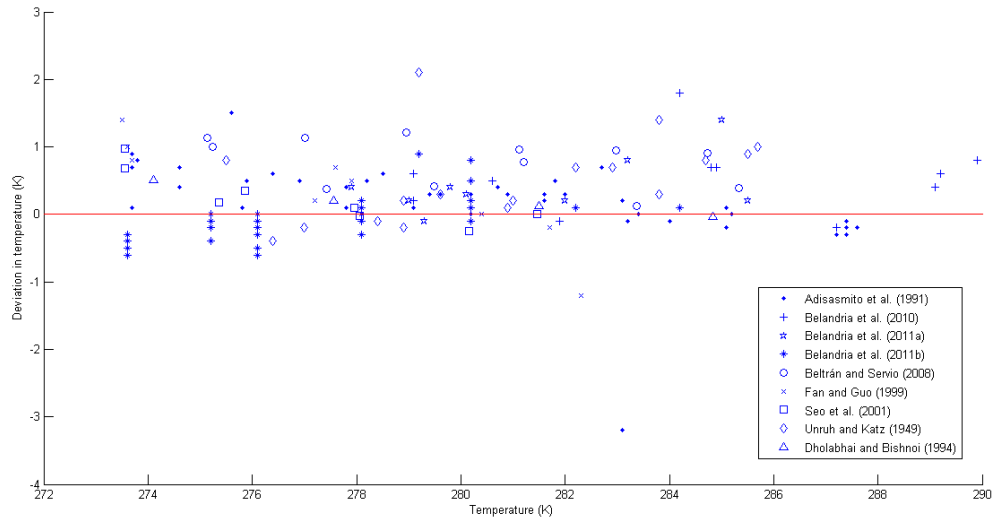


Figure 4.12: Estimate of deviation in temperature predictions for PVTsim with respect to measured dissociation temperatures for the CO<sub>2</sub>-CH<sub>4</sub>-H<sub>2</sub>O system from the literature. The legend lists the reference.

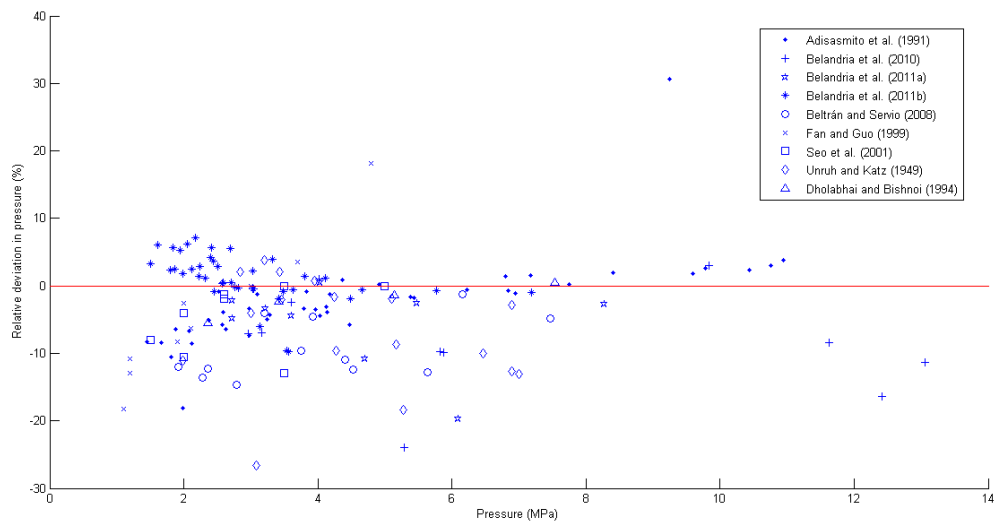


Figure 4.13: Estimate of relative deviation in pressure predictions for PVTsim with respect to measured dissociation pressures for the CO<sub>2</sub>-CH<sub>4</sub>-H<sub>2</sub>O system from the literature. The legend lists the reference.

### 4.3 Experiments performed at the University of Bergen

All experiments performed with the hydrate cell at UiB are listed in Table 4.6. The time- and PT traces constructed from data acquired for the experiments with confirmed hydrate formation are presented in Sections 4.3.2 – 4.3.4. Time- and PT traces without confirmed hydrate formation are presented in Appendix A.3 (Experiment 1, 3 and 4). Experiment 6, 7 and 14 were cancelled due to experimental problems, and are consequently not presented.

Table 4.6: List of experiments performed with the hydrate cell setup at UiB. Water volume ( $V_w$ ), initial temperature ( $T_{\text{initial}}$ ), set temperature ( $T_{\text{set}}$ ), initial pressure ( $P_{\text{initial}}$ ), and heating/dissociation rate are listed.

#	Hydrate former	$V_w$ (ml)	$T_{\text{initial}}$ (K)	$T_{\text{set}}$ (K)	$P_{\text{initial}}$ (MPa)	Heating rate (min/.1 K)	Hydrate formation?
1	CO <sub>2</sub>	200 <sup>a</sup>	296.4	276.0	5.92	-	No
2 <sup>1</sup>	CO <sub>2</sub>	200 <sup>a</sup>	326.8	276.0	5.96	6	Yes
3	CO <sub>2</sub>	200 <sup>a</sup>	302.1	276.0	3.75	6	No
4	CO <sub>2</sub>	200 <sup>a</sup>	294.2	276.0	3.94	6	No
5	CO <sub>2</sub>	200 <sup>a</sup>	295.4	276.0	4.84	6	Yes
8	CH <sub>4</sub>	50 <sup>c</sup>	296.0	274.0	6.18	6	Yes
9 <sup>2</sup>	CH <sub>4</sub>	50 <sup>c</sup>	297.2	274.0	5.73	6	Yes
10	CH <sub>4</sub>	100 <sup>b</sup>	295.6	274.0	6.59	12	Yes
11	CH <sub>4</sub>	200 <sup>a</sup>	295.6	274.0	7.03	6	Yes
12	CO <sub>2</sub> -CH <sub>4</sub>	200 <sup>a</sup>	296.1	276.0	6.05	12	Yes
13	CO <sub>2</sub> -CH <sub>4</sub>	200 <sup>a</sup>	292.0	276.0	6.06	6	Yes
15	CO <sub>2</sub> -CH <sub>4</sub>	200 <sup>a</sup>	295.6	276.0	6.07	6	Yes
16	CO <sub>2</sub> -CH <sub>4</sub>	200 <sup>a</sup>	294.8	276.0	6.89	6	Yes

<sup>a</sup> ± 0.15, <sup>b</sup> ± 0.10, <sup>c</sup> ± 0.05.

<sup>1</sup> Parallel of Experiment 1.

<sup>2</sup> Parallel of Experiment 8.

All experimental PT traces have been plotted with PT curves predicted by PVTsim (PR EOS). The fluid input in PVTsim has been predicted based upon the total system composition. The number of moles of H<sub>2</sub>O for each experiment was calculated directly via mass determination. The compressibility factor ( $Z$ ) was predicted by PVTsim by utilizing a PT flash at the initial pressure and temperature ( $P_{\text{initial}}$  and  $T_{\text{initial}}$ ). The same temperature and pressure was utilized when calculating the number of moles of vapor in the system (Equation 2.2). For the calculations it is assumed that the total system volume is 468 cm<sup>3</sup>, which is the volume used in calculations in previous publications [8-10]. The “dead-volume” is essentially neglected.

The vapor volume fraction is probably larger in reality than what is estimated. However, the hydrate equilibrium conditions predicted by PVTsim are generally the same for all water/hydrate former ratios, as previously mentioned. This was examined, and calculations which assumed a larger vapor volume did not yield a different PT curve in PVTsim.

The estimated system composition for the experiments with confirmed hydrate formation, performed at the University of Bergen is listed in Table 4.7. The composition of the mixed hydrate experiments performed has been indirectly determined by PVTsim (Section 4.3.4). A significant uncertainty can be expected for the system composition listed, due to the “dead volume” discovered. This is further explained in Section 5.3.

Table 4.7: Estimated system composition for the experiments performed.

#	%H <sub>2</sub> O	%CO <sub>2</sub>	%CH <sub>4</sub>
2	90.327	9.673	-
5	93.220	6.780	-
8	71.702	-	28.298
9	71.702	-	28.298
10	84.500	-	15.500
11	93.422	-	6.578
12	93.000	3.200	3.800
13	93.000	4.000	3.000
15	93.000	3.500	3.500
16	93.000	2.800	4.200

### 4.3.1 Simple CO<sub>2</sub> hydrate experiments

Figure A.1 in Appendix A.3 displays the pressure- and temperature time trace of experiment 1. This was a test experiment and was based upon the CO<sub>2</sub> hydrates procedure proposed by Vaular (2011) [9]. A pressure of approximately 0.5 MPa was applied during the cooling period. The system pressure was subsequently increased to 3.5 MPa, which was applied for about 20 minutes. The pressure data exhibited unusual pressure values, which may be observed in b) in Fig. A.1. The data has subsequently been removed in c).

The experimental PT trace for the experiment is shown in Fig. A.2. It is evident that the experimental PT trace is within the hydrate stability region indicated by the red PT curve predicted by PVTsim. The temperature- and pressure data however exhibits no signs of hydrate formation.

Figure 4.14 displays the pressure- and temperature time trace of experiment 2. This is a parallel of experiment of 1, as the presence of hydrates was not confirmed for the previous experiment. The system has been heated to approximately 333 K. This serves to remove the “memory effect” [4] associated with hydrates as a precaution if any hydrates were formed in experiment 1.

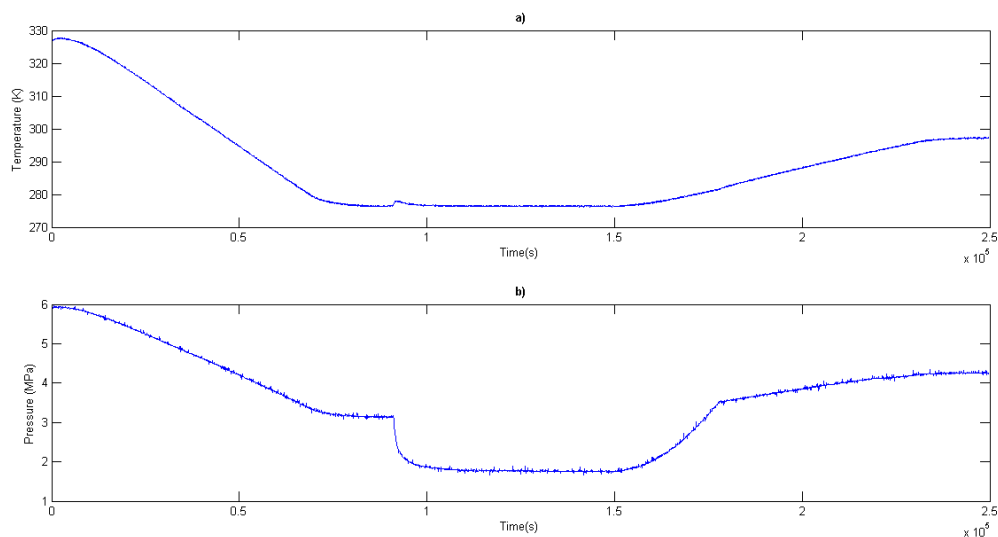


Figure 4.14: Temperature- and pressure time trace of experiment 2.

The data acquired for experiment 2 exhibit signs of hydrate formation in a) and b) respectively. An increase in temperature is observed in a), which is due to the exothermic heat associated with hydrate formation. The pressure trace simultaneously exhibits a pressure drop due to the incorporation of CO<sub>2</sub> gas molecules in hydrate structures.

Figure 4.15 displays the full experimental PT trace of experiment 2 in a), where b) displays the dissociation part of the experiment (zoomed in). The predicted PT curve by PVTsim in Fig. 4.15 essentially validates the experimental PT trace, as the accuracy of PVTsim for simple hydrates was established in Section 4.2.1. Due to the high water content in the system, hydrate formation automatically stops at the  $L_w$ -H-V equilibrium line. Further hydrate formation would result in a lower system pressure where hydrates would not be stable.

In b) in Fig. 4.15 it may be observed that the dissociation line of the experimental PT trace unmistakably follows the PT curve predicted by PVTsim during system heating, until all hydrates are dissociated, where the experimental PT curve consequently “breaks off” from the predicted PT curve by PVTsim.

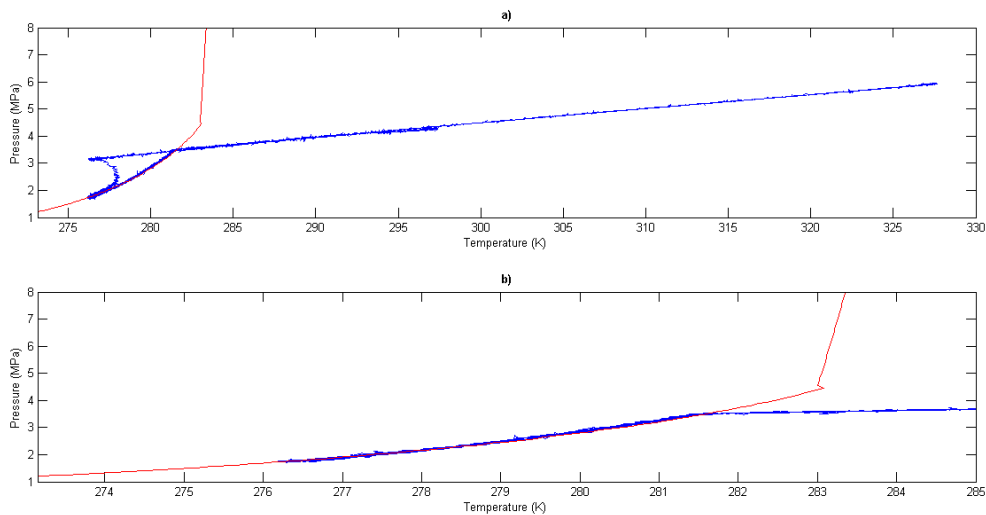


Figure 4.15: PT trace of experiment 2 (blue) plotted with the predicted PT curve by PVTsim (red).

Data from experiment 3 is presented in Figure A.3 and A.4 in Appendix A.3. From the latter it can be observed that the experimental PT trace does not cross the predicted PT curve by PVTsim. The system pressure is essentially too low for any hydrates to be stable.

Experiment 4 is presented in Figure A.5 and A.6 in Appendix A.3. The experimental PT trace barely crosses the predicted PT curve, and it is again hypothesized that the system pressure is too low for hydrate formation

Figure 4.16 presents the temperature- and pressure time trace of experiment 5. Hydrate formation is again evident by the increase in temperature and simultaneous pressure drop in a) and b) respectively.

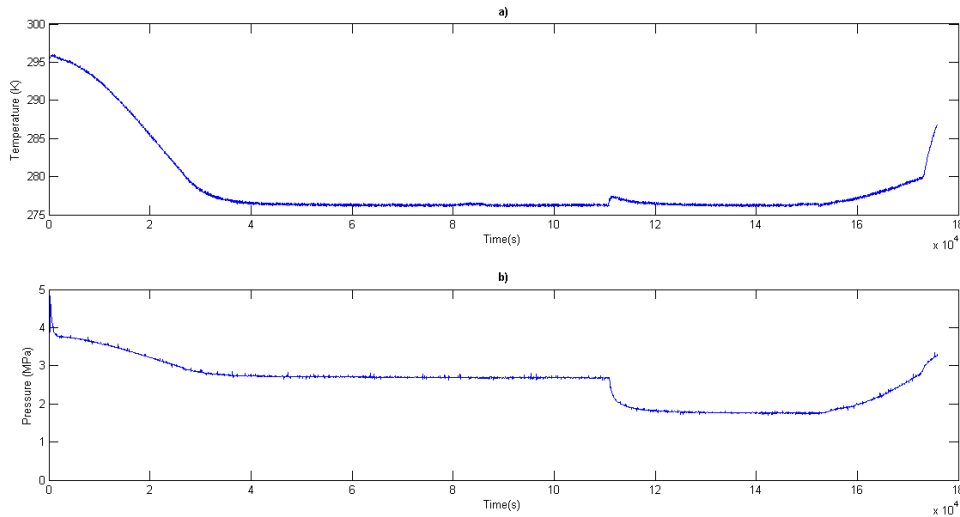


Figure 4.16: Temperature- and pressure time trace of experiment 5. The rapid increase in temperature at the end of the heating part of the experiment is due to the heating rate being reset. The incubator consequently increases the temperature as fast as possible.

Figure 4.17 presents the PT trace of experiment 5 plotted with the predicted PT curve by PVTsim. In b) it may be observed that the experimental data follows the predicted PT curve by PVTsim accurately. Hydrate formation again stops at the  $L_w$ -H-V equilibrium line and follows the predicted PT curve during dissociation until all hydrates are dissociated.

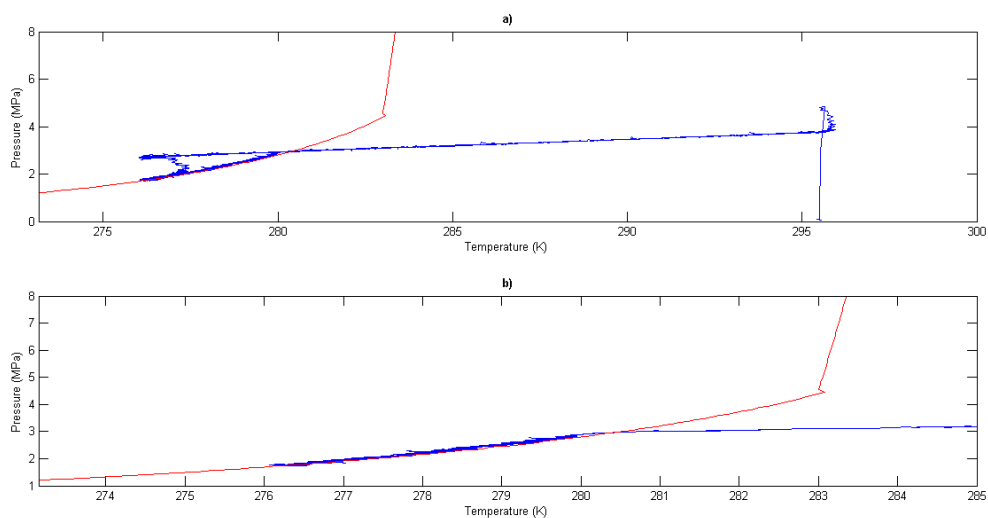


Figure 4.17. PT trace of experiment 5 (blue) plotted with the predicted PT curve by PVTsim (red).



### 4.3.2 Simple CH<sub>4</sub> hydrate experiments

The temperature- and pressure time trace of experiment 8 is shown in Fig. 4.18 below.

Hydrate formation is evident by the increase in temperature and simultaneous pressure drop in a) and b) respectively.

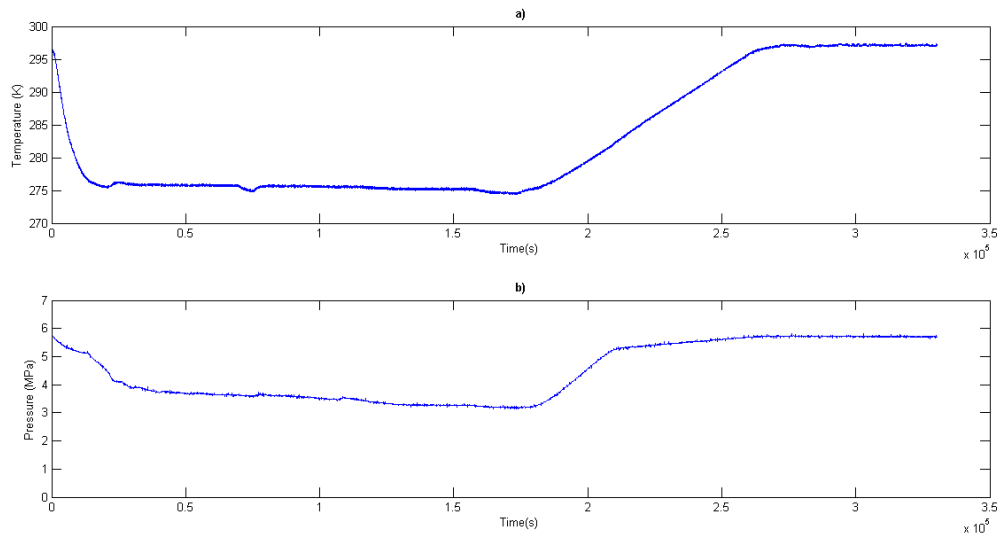


Figure 4.18: Temperature- and pressure time trace of experiment 8. Between  $0.5 - 1 \cdot 10^5$  seconds a small drop in temperature is observed in a). This is because the stirrer was turned off to prevent it from overheating.

The PT trace for experiment 8 is presented in Fig 4.19. The experimental PT trace deviates somewhat initially during heating (approximately 274.5 K). Thenceforth it follows the predicted PT curve before it again deviates at temperatures above 278 K.

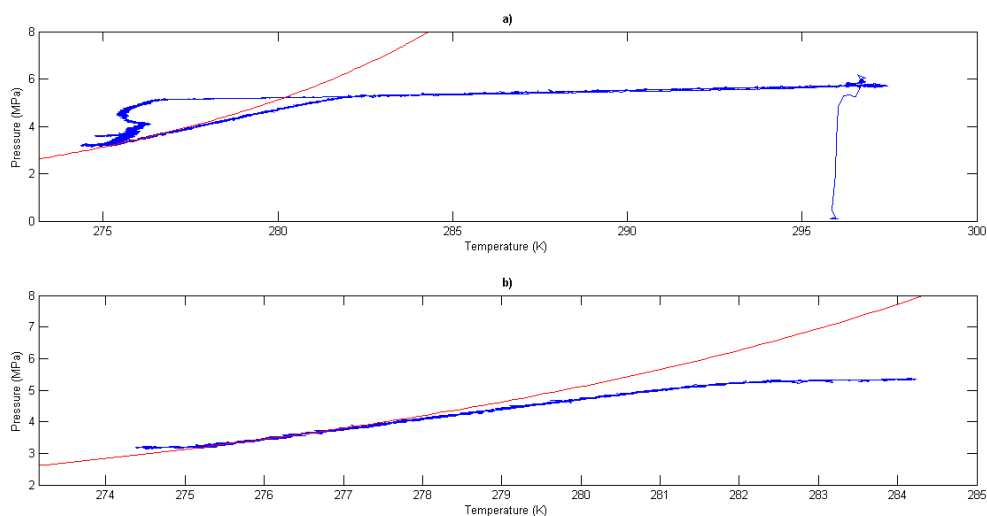


Figure 4.19: PT trace of experiment 8 (blue) plotted with the predicted PT curve by PVTsim (red).

The temperature- and pressure time trace of experiment 9 is shown in Fig. 4.20 below. This was a parallel of experiment 8, and was performed to re-examine the deviation observed in the PT trace of experiment 8. Hydrate formation is again evident by the increase in temperature and simultaneous pressure drop in a) and b) respectively.

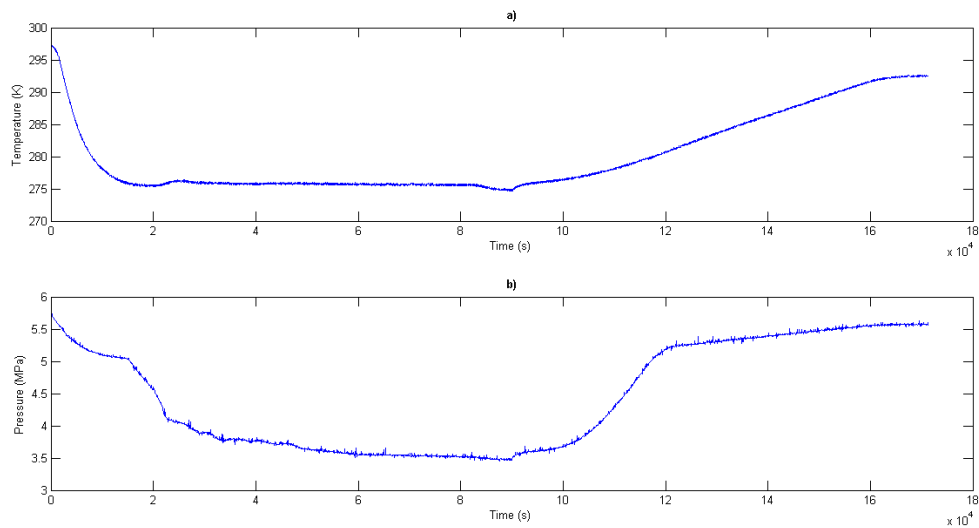


Figure 4.20: Temperature- and pressure time trace of experiment 9. Between  $8 - 10 \cdot 10^4$  seconds a small temperature drop is observed in a). This is again because the stirrer was turned off to prevent it from overheating.

The PT trace for experiment 9 is presented in Fig 4.21. It may be observed that the experimental PT trace deviates somewhat initially during heating (approximately 275.8 K). It subsequently follows the predicted PT curve by PVTsim accurately, and the deviation during dissociation is not as pronounced for this experiment as for experiment 8.

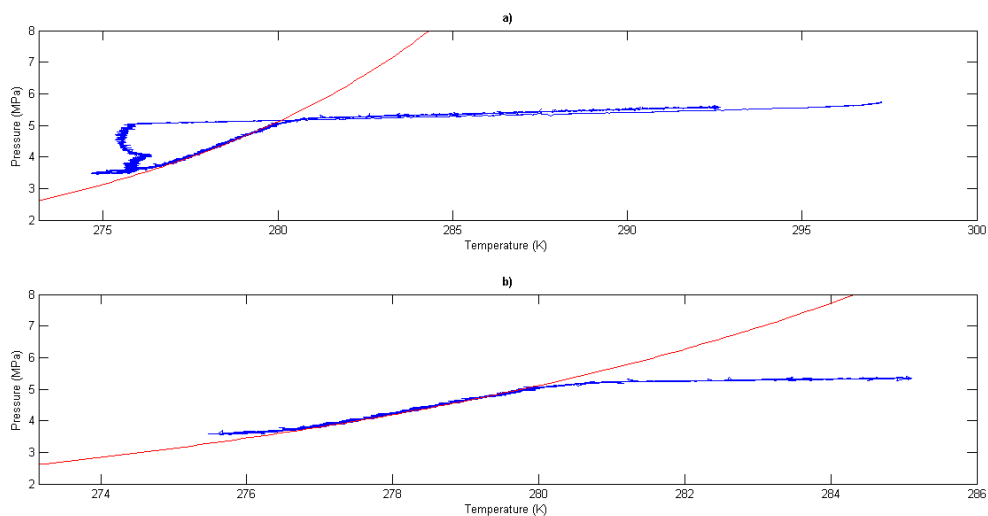


Figure 4.21: PT trace of experiment 9 (blue) plotted with the predicted PT curve by PVTsim (red).

The temperature- and pressure time trace of experiment 10 is shown in Fig. 4.22 below. Hydrate formation is again evident by the temperature increase and simultaneous pressure drop in a) and b) respectively.

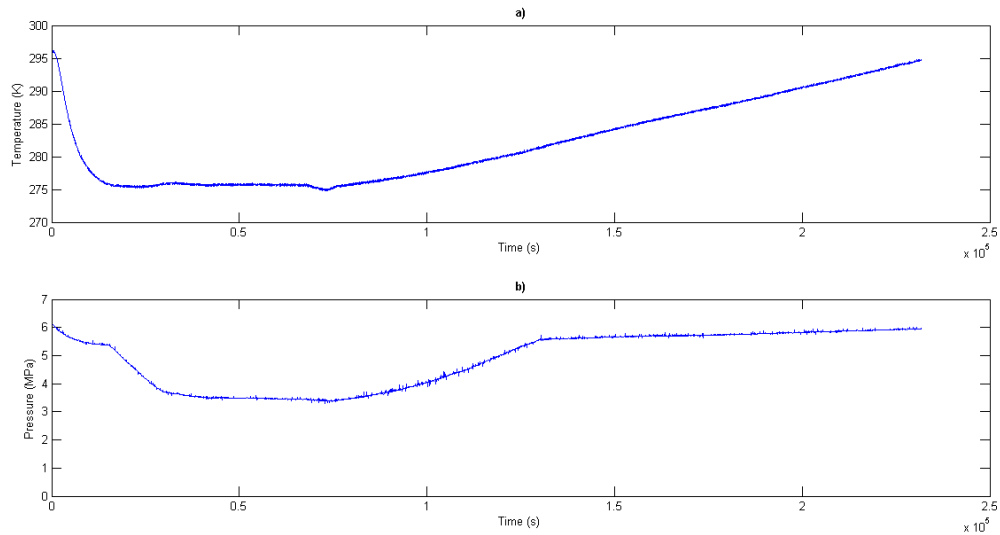


Figure 4.22: Temperature- and pressure time trace of experiment 10. A small temperature drop is again observed between  $0.5 - 1 \cdot 10^5$  seconds, due to stirrer being off.

The PT trace for experiment 10 is presented in Fig 4.23. It may be observed that the experimental PT trace deviates somewhat initially during heating (approximately 274.8 K). It subsequently follows the predicted PT curve by PVTsim accurately, before it again deviates at approximately 280.5 K.

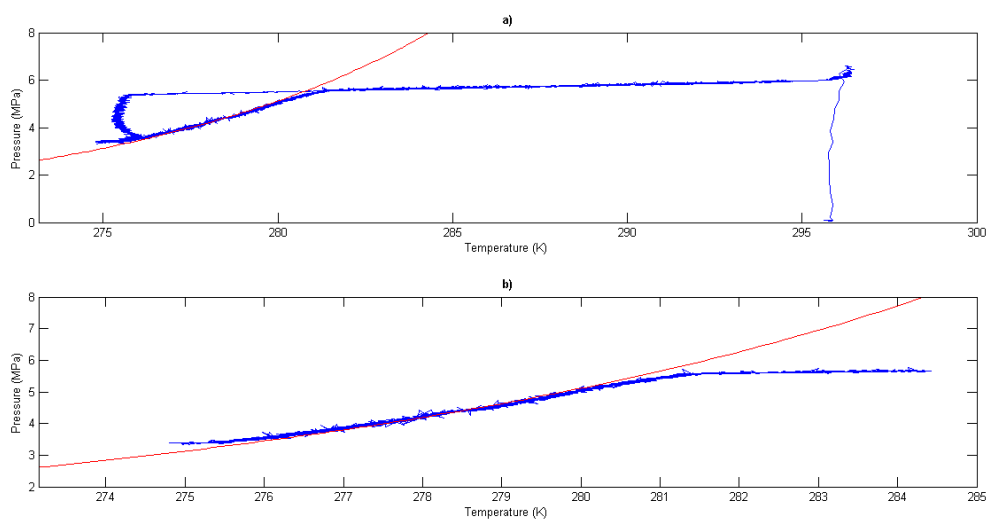


Figure 4.23: PT trace of experiment 10 (blue) plotted with predicted PT curve by PVTsim (red).

The temperature- and pressure time trace of experiment 11 is shown in Fig. 4.24 below. It may be observed that the increase in temperature associated with the exothermic heat of hydrate formation is not as pronounced in Fig 4.24 a) as in previous experiments. The simultaneous pressure drop associated with the incorporation of CH<sub>4</sub> gas in hydrates is however evident in b).

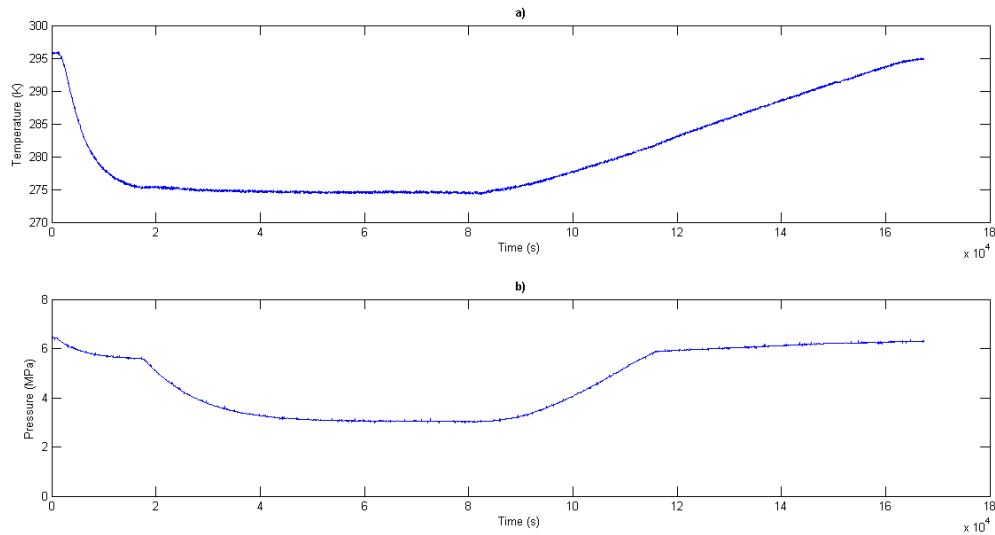


Figure 4.24: Temperature- and pressure time trace of experiment 11.

The PT trace for experiment 11 is presented in Fig 4.25. In b) it may be observed that the dissociation line of the experimental PT trace follows the PT curve predicted by PVTsim accurately during heating, with a minimal deviation observed between 281 – 282 K.

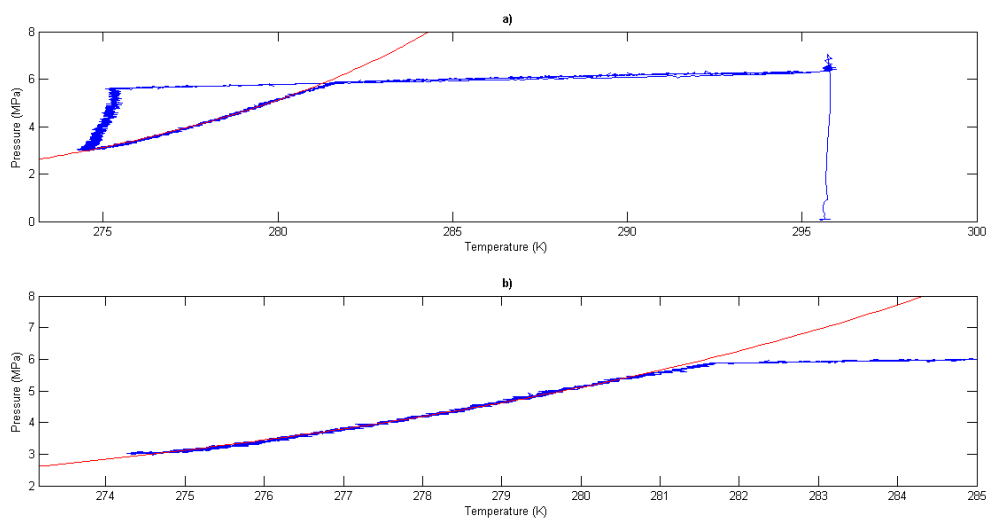


Figure 4.25: PT trace of experiment 11 (blue) plotted with predicted PT curve by PVTsim (red).

### 4.3.3 Mixed CO<sub>2</sub>-CH<sub>4</sub> hydrate experiments

The total system composition could not be determined for the mixed hydrate experiments due to the “dead volume” discovered (Section 3.5). However, having already established the accuracy of PVTsim predictions based upon previous studies (Section 4.2.2), the system composition of the mixed hydrate experiments could be indirectly determined with PVTsim. The water content for all mixed hydrate experiments has been approximated to 93 %. Although this composition is approximated, the predicted PT curves by PVTsim changes only slightly when varying the water content (and keeping the other components constant) as previously mentioned.

The experimental PT trace from the experiments were plotted, and several PT curves were predicted in PVTsim by varying the CO<sub>2</sub>/CH<sub>4</sub> ratio. The curve in most agreement with the experimental data was selected, and the composition which predicted this PT curve was approximated as the total system composition of that experiment. CO<sub>2</sub>- and CH<sub>4</sub> hydrate PT curves has also been plotted as dotted lines in the subsequent PT diagrams presented.

Figure 4.26 shows the pressure and temperature time trace of experiment 12, which was the first mixed CO<sub>2</sub>-CH<sub>4</sub> experiment performed. The exothermic heat associated with hydrate formation may be observed in a) as an increase in temperature, with a simultaneous pressure drop evident in b).

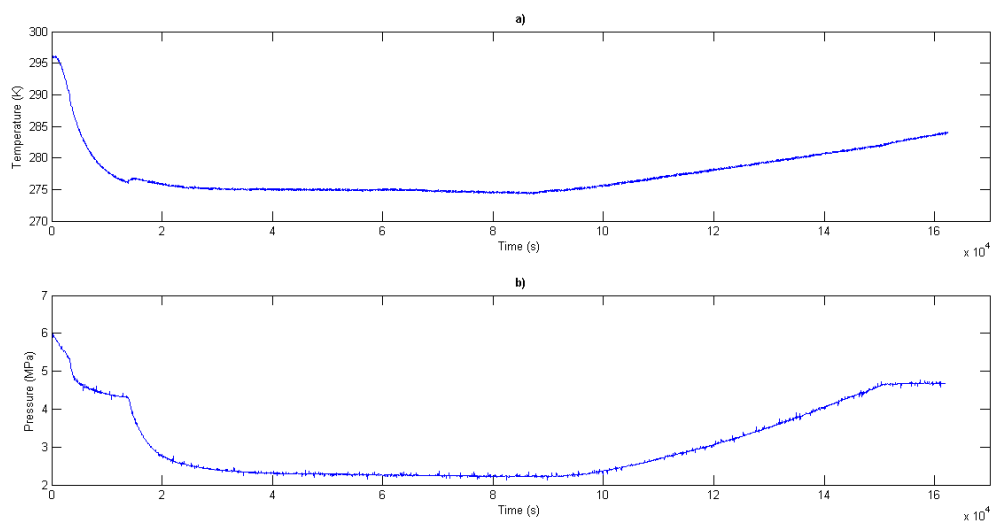


Figure 4.26: Temperature- and pressure time trace of experiment 12.

The experimental PT trace for experiment 12 is shown in Fig. 4.27. It may be observed that the experimental dissociation line is located between the predicted PT curves for simple CO<sub>2</sub>- and CH<sub>4</sub> hydrates. The experimental PT trace initially deviates from the predicted PT curve by PVTsim at approximately 274.5 K, before it follows the predicted PT curve accurately. A minimal deviation may additionally be observed at approximately 281.9 K.

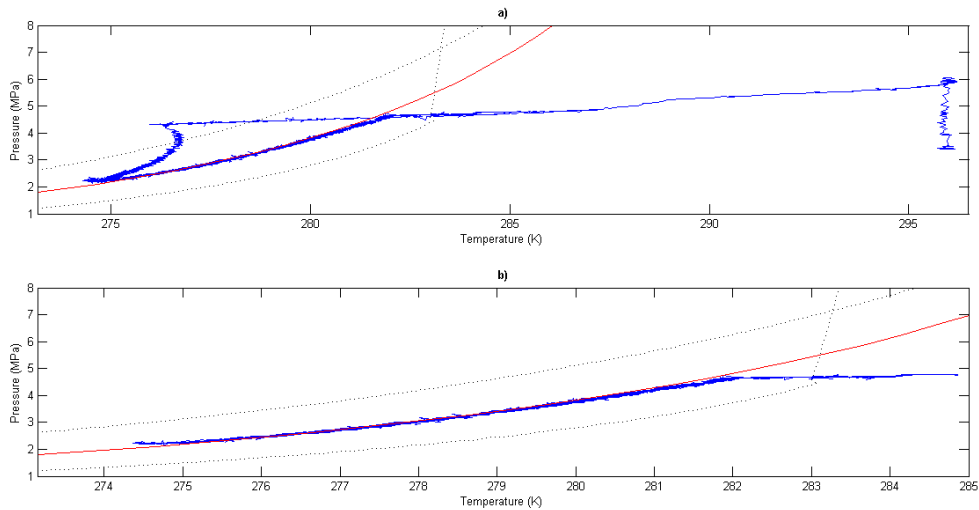


Figure 4.27: PT trace of experiment 12 (blue) plotted with predicted PT curve by PVTsim (red). System composition indirectly determined to 3.2% CO<sub>2</sub> and 3.8% CH<sub>4</sub>. The dotted lines are PT curves for simple CH<sub>4</sub> and CO<sub>2</sub> hydrates.

The temperature and pressure time trace of experiment 13 is presented in Figure 4.28. Hydrate formation is again evident by the increase in temperature, and the simultaneous pressure drop observed in a) and b) respectively.

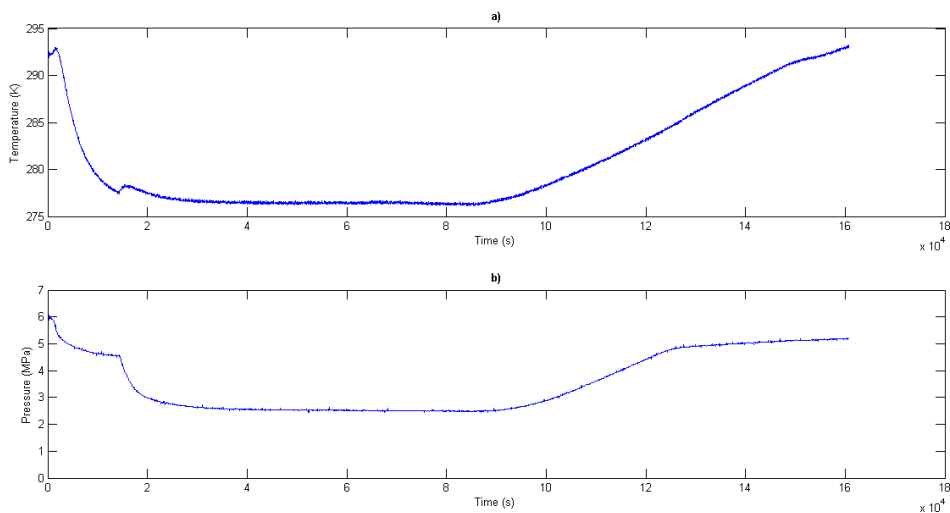


Figure 4.28: Temperature and pressure time trace of experiment 13.

The experimental PT trace for experiment 13 is shown in Figure 4.29. It may be observed that the experimental dissociation line is located between the predicted PT curves for simple CO<sub>2</sub>- and CH<sub>4</sub> hydrates. The experimental PT trace initially deviates somewhat from the predicted PT curve at approximately 276.2 K, before it follows the predicted PT curve accurately. A significant deviation is subsequently observed at approximately 280 K.

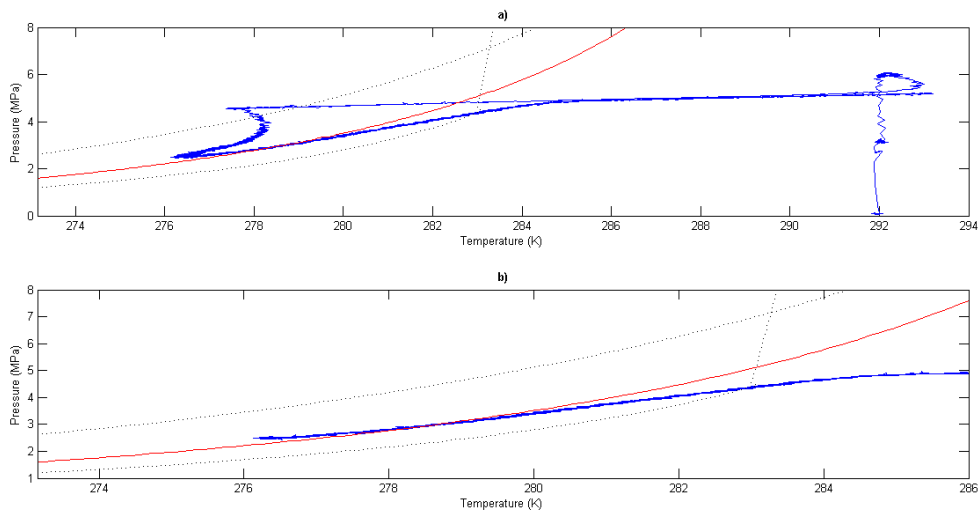


Figure 4.29: PT trace of experiment 13 (blue) plotted with predicted PT curve by PVTsim (red). System composition indirectly determined to 4% CO<sub>2</sub> and 3 % CH<sub>4</sub>. The dotted lines are PT curves for simple CH<sub>4</sub> and CO<sub>2</sub> hydrates.

The temperature and pressure time trace of experiment 15 is presented in Figure 4.30. Hydrate formation is again evident by the increase in temperature, and the simultaneous pressure drop observed in a) and b) respectively.

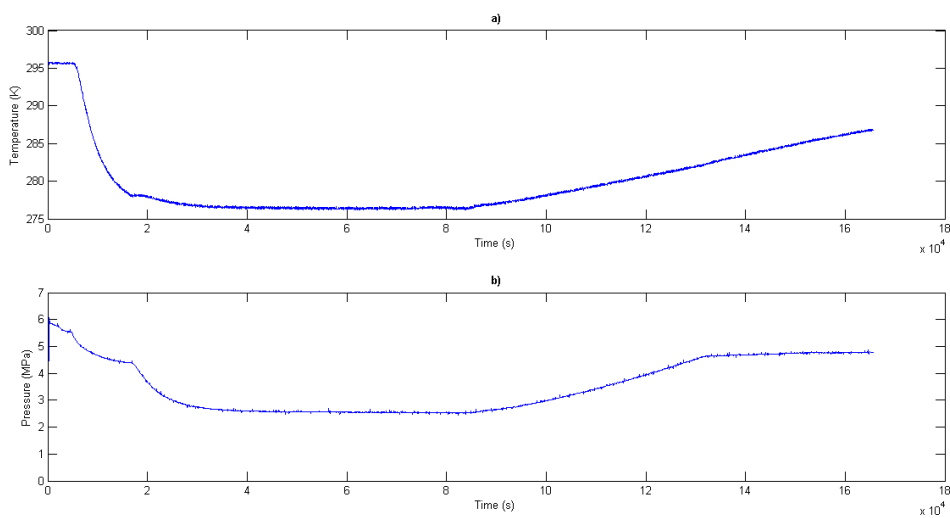


Figure 4.30: Temperature and pressure time trace of experiment 15.

The experimental PT trace for experiment 15 is shown in Figure 4.31. It may be observed that the experimental dissociation line is located between the predicted PT curves for simple CO<sub>2</sub>- and CH<sub>4</sub> hydrates. A minimal deviation is observed during initial heating, at approximately 276.3 K. The experimental PT trace subsequently follows the predicted PT curve accurately.

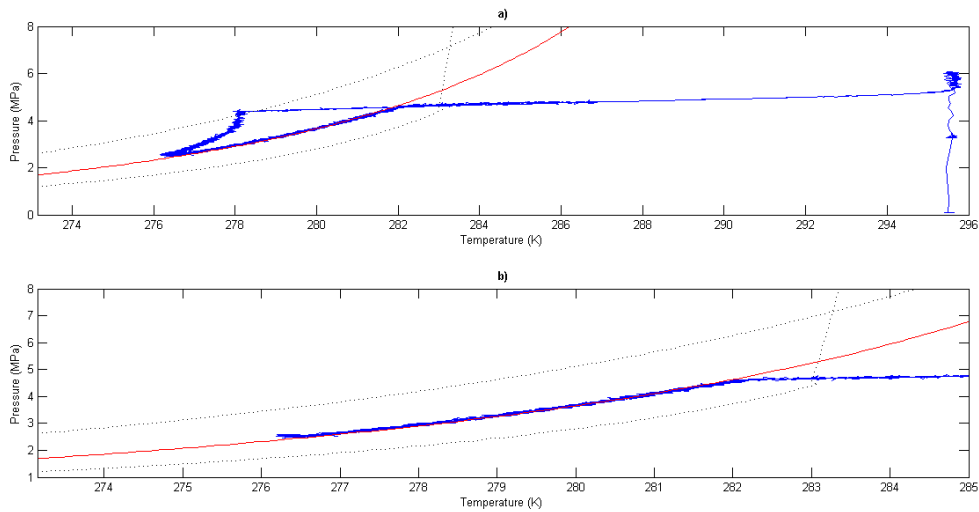


Figure 4.31: PT trace of experiment 15 (blue) plotted with predicted PT curve by PVTsim (red). System composition indirectly determined to 3.5% CO<sub>2</sub> and 3.5% CH<sub>4</sub>. The dotted lines are PT curves for simple CH<sub>4</sub> and CO<sub>2</sub> hydrates.

The temperature and pressure time trace of experiment 16 is presented in Figure 4.32. Hydrate formation is again evident by the increase in temperature, and the simultaneous pressure drop observed in a) and b) respectively.

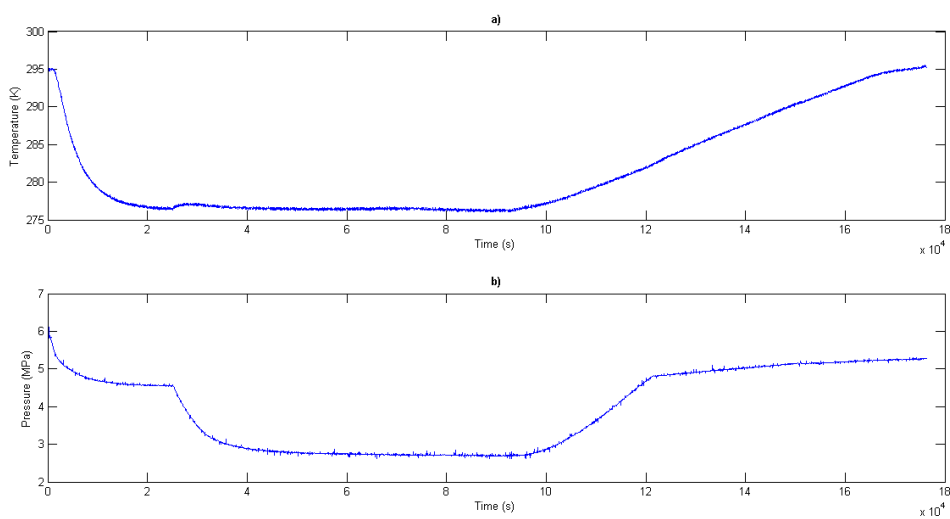


Figure 4.32: Temperature and pressure time trace of experiment 16.



The experimental PT trace for experiment 16 is shown in Figure 4.33. It may be observed that the experimental dissociation line is located between the predicted PT curves for simple CO<sub>2</sub>- and CH<sub>4</sub> hydrates. A minimal deviation is observed during initial heating at approximately 276.1 K. The experimental PT trace subsequently follows the predicted PT curve accurately, before it deviates somewhat at approximately 281.7 K.

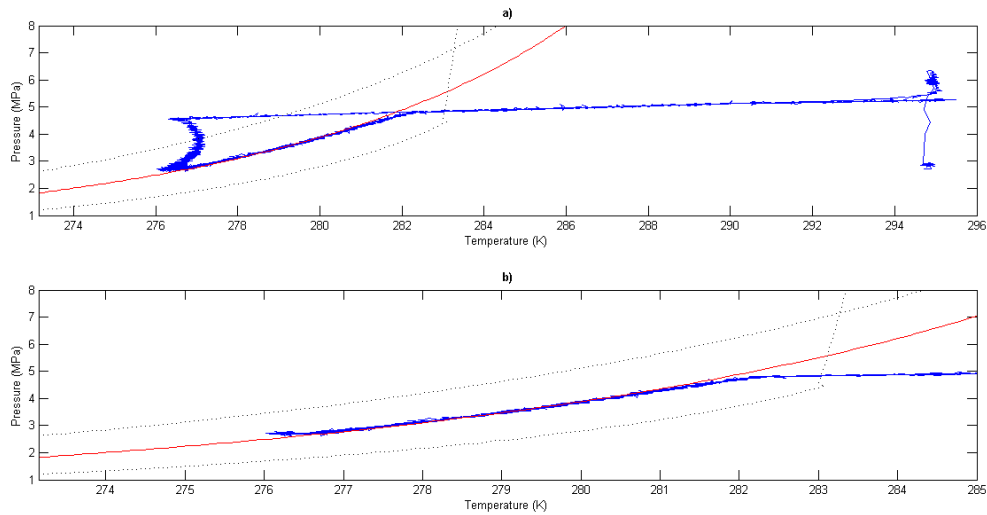


Figure 4.33: PT trace of experiment 16 (blue) plotted with predicted PT curve by PVTsim (red). System composition indirectly determined to 2.8% CO<sub>2</sub> and 4.2% CH<sub>4</sub>. The dotted lines are PT curves for simple CH<sub>4</sub> and CO<sub>2</sub> hydrates.

#### 4.4. Experiments performed at Statoil

As the total composition of the mixed CO<sub>2</sub>-CH<sub>4</sub> hydrate experiments performed at UiB could not be determined, the accuracy of PVTsim predictions could not be conclusively determined. Simulations performed based upon dissociation conditions listed in the literature on mixed CO<sub>2</sub>-CH<sub>4</sub> hydrates indicates that PVTsim accurately predicts equilibrium conditions.

However, as the data is from other sources the reliability of the measurements are not always certain. Some of the examined data is additionally from studies published several decades ago. Finally, with the exception of the data from Belandria et al. (2011), the system composition for previous mixed CO<sub>2</sub>-CH<sub>4</sub> hydrates has been approximated. To ultimately validate the hypothesis that PVTsim can be utilized to accurately predict equilibrium conditions for mixed CO<sub>2</sub>-CH<sub>4</sub> hydrates it was decided to perform a couple of experiments at the PVT laboratory at Statoil.

The experimental setup and the equipment available at Statoil, allowed for an accurate determination of the system composition for the experiments performed. The number of moles of H<sub>2</sub>O was calculated with Eq.(2.1). As the volume of gas injected into the hydrate cell was known, the number of moles of gas could be calculated with Eq.(2.2). The temperature and pressure after gas injection was known, and the compressibility factor (Z) was determined by PVTsim by utilizing a PT flash at these conditions (90/10 CH<sub>4</sub>-CO<sub>2</sub> fluid). The number of moles of each component in the vapor could subsequently be determined through Eq.(2.4). The total composition was calculated by Eq.(2.2).

From the calculations performed, the total system composition was determined to be: 63.699% H<sub>2</sub>O, 32.671% CO<sub>2</sub> and 3.630% CH<sub>4</sub>.

There is significantly less water in the system than what has usually been utilized by previous authors. This was desired as to compare the various ternary diagrams in this thesis where the water amount is fixed at 50.000. Due to the low water amount in the system, it is expected that full conversion of the water to hydrate is probable. The reason for the high concentration of CO<sub>2</sub> in the system is that PVTsim sometimes estimates the hydrate dissociation pressure and temperature in the high pressure region for high concentrations of CO<sub>2</sub> less accurately. At these conditions the CO<sub>2</sub>-CH<sub>4</sub> mixture might form a liquid phase.

Figure 4.34 presents the VT (volume-temperature) trace of experiment A. The temperature is measured by two temperature sensors. The average of the sensors has consequently been set as the temperature measured. The pressure was kept constant at approximately 7.7 MPa during the experiment.

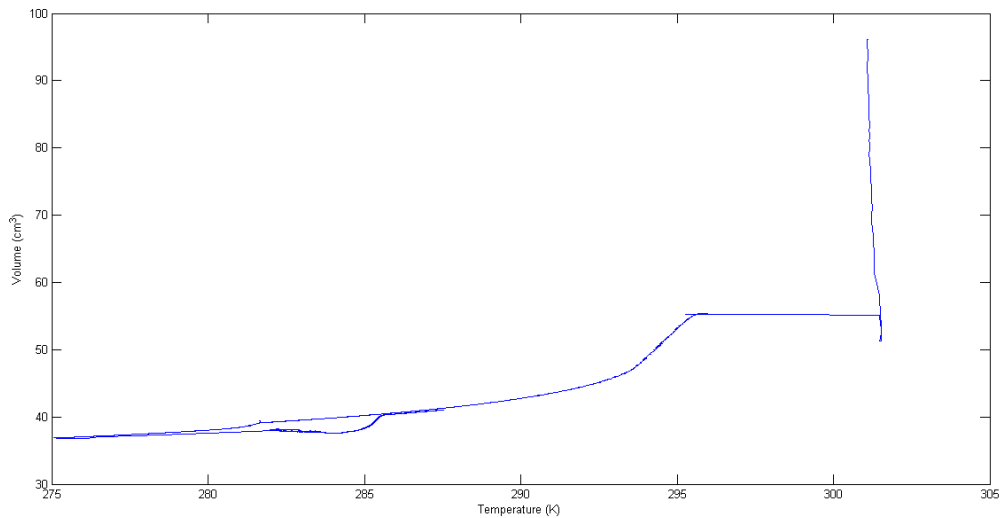


Figure 4.34: Full experimental VT trace of experiment A. Figure 4.35 presents a zoomed in part of the experimental VT trace.

Hydrate formation is indicated in Fig. 4.35 as a decrease in volume. Hydrate dissociation is contrarily indicated by an increase in volume during system heating. The dissociation point is the point where the last hydrate crystal melts (Section 1.2.4), and the thermodynamic conditions (PT) at this point is the values utilized to determine the accuracy of PVTsim predictions.

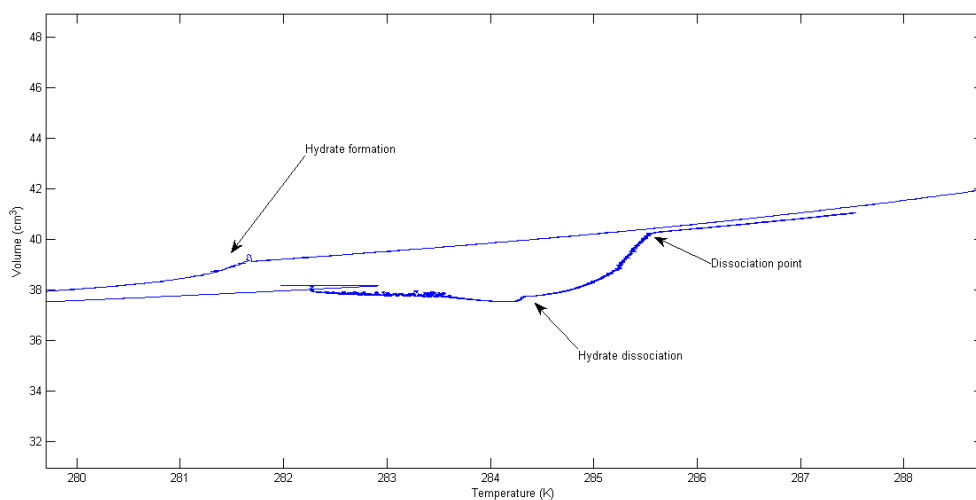


Figure 4.35: Zoomed in part of experiment A.

It can be observed from the VT trace in Fig. 4.35, and in the following figures, that the dissociation line does not hit the cool down line during system heating. A small gap between the cool down line and the dissociation line may be observed in Fig 4.35. This is due to hysteresis from the volume sensor. This does not influence the measured temperature and pressure.

Experiment B is a parallel experiment of A. The same isobaric conditions was applied (approximately 7.7 MPa). The full VT trace of experiment B is shown in Figure 4.36. Hydrate formation may again be observed as a decrease in volume. Hydrate dissociation is contrarily indicated by an increase in volume during system heating.

It may again be observed that the volume does not fall on the cool down line, where it is more pronounced for this experiment than for experiment A. The hysteresis of the volume sensor may be observed at approximately 279 K, as a small increase in volume. The subsequent values read are somewhat higher than the true volume of the system, which explains why the heating line “breaks off” at a somewhat higher volume.

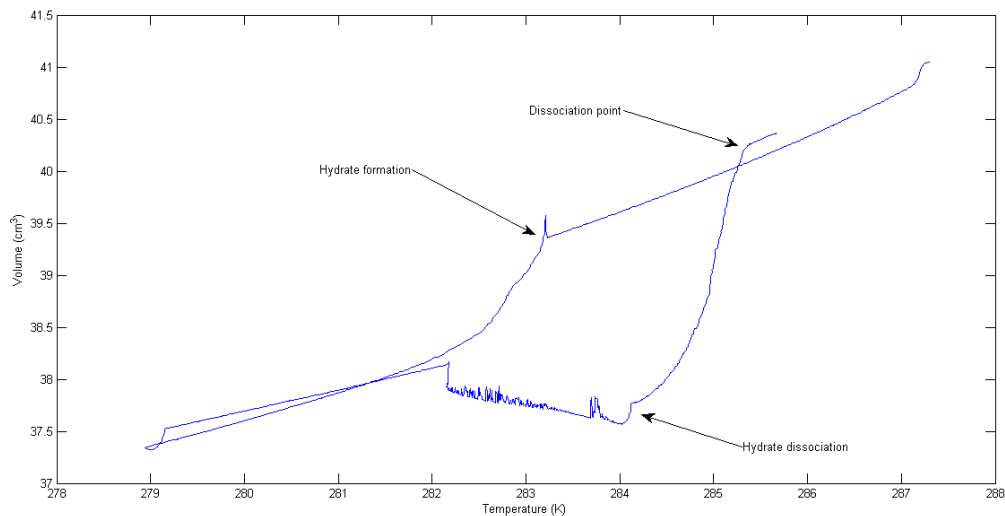


Figure 4.36: Full experimental VT trace of experiment B.

Figure 4.37 presents the full experimental VT trace of experiment C. A lower pressure was utilized for this experiment (approximately 7.0 MPa). Hydrate formation is again observed as a decrease in volume. Hydrate dissociation is contrarily indicated by an increase in volume during system heating. It may again be observed that the heating line of the experiment does not hit the cool down line directly.

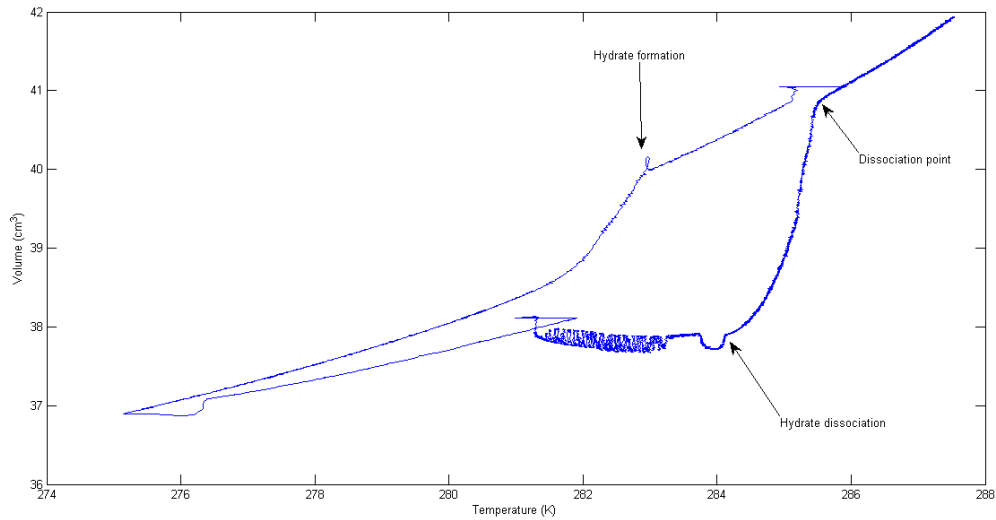


Figure 4.37: Full experimental VT trace of experiment C.

Table 5.3 in Section 5.4 lists the dissociation conditions determined for the experiments performed at Statoil. The dissociation conditions determined have been compared with predictions from PVTsim, where a discussion of the results is additionally provided.

## CHAPTER 5: DISCUSSION

### 5.1 PVTsim simulations of the CO<sub>2</sub>-CH<sub>4</sub>-H<sub>2</sub>O system

It was observed that PVTsim predicted a structural transition from sI to sII hydrate at specific compositions when utilizing the SRK EOS for simulations of the CO<sub>2</sub>-CH<sub>4</sub>-H<sub>2</sub>O system (Fig. 4.1). The structure changes back to sI again at high CO<sub>2</sub> concentrations. This was not observed when utilizing the PR EOS for the simulations, which predicts sI for all CO<sub>2</sub>-CH<sub>4</sub> ratios (Fig 4.2).

#### 5.1.1 Previous research on mixed CO<sub>2</sub>-CH<sub>4</sub> hydrate structures

It was established in Section 1.2 that CO<sub>2</sub> and CH<sub>4</sub> both form sI hydrates as simple hydrates. In previous studies regarding the phase equilibria of mixed CO<sub>2</sub>-CH<sub>4</sub> hydrates, it is either stated or assumed that a CO<sub>2</sub>-CH<sub>4</sub> gas mixture forms sI hydrate across the entire mole fraction range (Table 1.3). An exception is the study by Belandria et al. (2010), where a possible structural transition is specifically addressed. The authors compared experimental dissociation measurements with the HWHYD software, with predictions for both sI and sII. The deviation between experimental and predicted dissociation conditions were lower when assuming sI, where they subsequently concluded that this was the structure formed in their experiments [47].

CO<sub>2</sub>-CH<sub>4</sub> binary gas mixtures always form sI hydrates according to Sloan and Koh (2008) [4]. In the study by Hester and Sloan (2005) it is explicitly stated that CO<sub>2</sub> as an intermediate hydrate former cannot form sII hydrates with other sI hydrate formers. This was based upon results from hydrate modeling in CSMGem [75].

As thermodynamic equilibrium measurements and hydrate modeling are not comprehensive enough to determine the hydrate structure, other suitable techniques such as NMR, X-ray diffraction, or Raman spectroscopy is required to accurately determine the hydrate structure [4].

Rovetto et al. (2008) examined mixed CO<sub>2</sub>-CH<sub>4</sub> hydrates with <sup>13</sup>C NMR spectroscopy, with sI being formed in all experiments [76]. Lee et al. (2013) recently measured the <sup>13</sup>C NMR spectrum of mixed CO<sub>2</sub>-CH<sub>4</sub> hydrates, with hydrates formed from a feed gas mixture of 20%, 40%, 60% and 80% CO<sub>2</sub>. sI hydrate was determined for all compositions [77].

Schicks et al. (2011) examined the CO<sub>2</sub>-hydrocarbon exchange process with Raman spectroscopy and X-ray diffraction methods. When exposing pure CH<sub>4</sub> hydrate with CO<sub>2</sub>, a mixed hydrate formed, which was determined to be sI. Mixed CH<sub>4</sub>-C<sub>2</sub>H<sub>6</sub> and CH<sub>4</sub>-C<sub>3</sub>H<sub>8</sub> sII hydrates were additionally observed through both Raman spectroscopy and X-ray diffraction to undergo structural transitions when exposed to CO<sub>2</sub>, where a CO<sub>2</sub> rich sI hydrate was subsequently formed [32]. Finally, Schicks and Helbing (2013) examined hydrate formation from a CO<sub>2</sub>-CH<sub>4</sub> binary gas mixture with a composition of 9.7% CO<sub>2</sub> by Raman spectroscopy, which was determined to be sI [78].

### 5.1.2 Ternary phase diagrams

The simulations performed in PVTsim for the ternary CO<sub>2</sub>-CH<sub>4</sub>-H<sub>2</sub>O system, is hereby discussed. The results which are deemed significant is thoroughly discussed, while scattered data and general observations receives less attention and is consequently only summarized.

From Table 4.1 it is seems that the pressure and temperature has a small, and almost insignificant effect on the structural transitions predicted by SRK. At higher pressures (isothermal) the structural transitions occurs at higher CO<sub>2</sub> concentrations in the original fluid. The same trend is observed for higher temperatures (isobaric). The structural transitions observed for simulations with the SRK EOS thus seems to be mainly a function of the fluid composition.

It seems that the only pronounced effect the observed structural transition has on the predicted phase compositions, is regarding the fraction of CO<sub>2</sub> in the hydrate phase ( $z_{CO_2}$ ). From Figure 4.4 it may be observed that  $z_{CO_2}$  calculated from sI predictions by both SRK and PR are very similar.  $z_{CO_2}$  calculated from sII predictions by SRK is however significantly different from  $z_{CO_2}$  calculated from sI predictions by both PR and SRK.

From Figure 4.4 it may be observed that SRK predicts a larger  $z_{CO_2}$  for sII hydrate than PR do for sI hydrate, when the fluid utilized for the simulations has a low CO<sub>2</sub> concentration (Tick No. 2-3). When the fluid has a higher CO<sub>2</sub> concentration the opposite is however observed (Tick No. 5-8).  $z_{CO_2}$  calculated from sI predictions by PR, are larger than  $z_{CO_2}$  calculated by sII predictions from SRK. Looking at a) – i) in Figure 4.4, it may be observed that the latter is predicted in the majority of the cases.

In Table 1.2 the guest molecule/cavity ratio for CO<sub>2</sub> in the 5<sup>12</sup> cavity is listed as 1.00 and 1.02, for sI and sII respectively. Sloan and Koh (2008) states that at ratios above 1.0, the guest molecule cannot occupy the cavity without distortion [4]. This does not necessarily mean that CO<sub>2</sub> molecules cannot occupy the 5<sup>12</sup> cavities in sI. Circone et al. (2003) determined that as a simple hydrate former, CO<sub>2</sub> preferentially occupies the large cavities in sI hydrate, while the smaller 5<sup>12</sup> cavities have a variable cavity-filling dependent on the synthesis conditions [15]. Uchida et al. (2004) determined through thermodynamic modelling that CO<sub>2</sub> preferably occupies the large cavities, and CH<sub>4</sub> preferably occupies the small cavities in mixed sI CO<sub>2</sub>-CH<sub>4</sub> hydrates. However, the authors also states that the CO<sub>2</sub> and CH<sub>4</sub> molecules compete with each other regarding cavity occupation, as both guest molecules may occupy both the 5<sup>12</sup> and the 5<sup>12</sup>6<sup>2</sup> cavity [79].

Based on what was discussed in the preceding paragraph, it is subsequently assumed that CO<sub>2</sub> preferentially occupies the large cavities, while the smaller cavities are primarily occupied by CH<sub>4</sub>. The reason that sII usually results in a lower CO<sub>2</sub> fraction in the hydrate than sI, is thus hypothesized to be because of the cavity difference in the different hydrate structures. sI hydrate consists of two 5<sup>12</sup> and six 5<sup>12</sup>6<sup>2</sup> cavities while sII consists of sixteen 5<sup>12</sup> and eight 5<sup>12</sup>6<sup>4</sup> (Table 1.1). As sII consists of a larger amount of small cavities, a larger CH<sub>4</sub> fraction and a lower CO<sub>2</sub> fraction in the sII hydrate can be expected. This is usually what is predicted by PVTsim for the simulations presented in Section 4.1.1.

The hypothesis proposed above however fails when looking at the simulations where SRK predicted a larger z<sub>CO2</sub> for sII hydrate than what both PR and SRK predicted for sI hydrate in Fig. 4.4 (Tick No. 2-3). It is ultimately hard to determine a definite trend regarding the distribution of CO<sub>2</sub> in the hydrate phase. The literature however agrees that mixed CO<sub>2</sub>-CH<sub>4</sub> hydrates always form sI hydrate, where it may subsequently be argued that the validity regarding sII predictions from SRK should be questioned.

Other observations regarding the simulations performed in Section 4.1.1 are as follows:

- The difference in y<sub>CO2</sub> between the two respective EOS is not very pronounced (Fig. 4.3).
- SRK predicts a higher H<sub>2</sub>O fraction for both sI and sII compared to PR. A lower z<sub>CO2</sub> and z<sub>CH4</sub> fraction is consequently predicted by SRK (Table 4.2). The difference is however minimal.



### 5.1.3 PVTsim predictions compared with data from Belandria et al. (2011).

The experimental data published by Belandria et al. (2011) [48] have additionally been used as a reference to examine the significance of the structural transitions predicted by SRK. The results which are deemed significant is thoroughly discussed, while scattered data and general observations receives less attention and is consequently only summarized.

From Table 4.3 it may be observed that both PR and SRK predicts accurate dissociation conditions for the values listed in the reference (40. pts.). It may also be observed that predictions from PR results in a smaller calculated deviation in both temperature and pressure, compared to SRK predictions.

Calculated deviations is plotted against listed phase compositions from the reference in Fig. 4.9. The absolute average deviations are additionally listed in Table 4.4. PVTsim generally predicts a significantly large deviation for all phase compositions compared to the listed values in the reference. It should however be noted that the equilibrium temperature and pressure listed in the reference, which is used as T and P values for the Hydrate PT flash in PVTsim not always predicts the same phases as what is measured in the reference. PVTsim may predict  $L_w$ -V equilibria at conditions where the reference list  $L_w$ -H-V equilibria. The following points summarizes observations for the simulations performed (Table 4.4):

- Row 3 and 4 lists  $L_w$ -H-V equilibria predictions. PR predicts  $L_w$ -H-V equilibria for 21 points while SRK predicts  $L_w$ -H-V equilibria for 16 points. It may be observed that the calculated deviations for both PR and SRK is larger when considering only  $L_w$ -H-V equilibria predictions, where the difference is more pronounced for SRK predictions. This is surprising considering what was discussed in the preceding paragraph.
- Row 5 and 6 lists seven points where  $L_w$ -H-V equilibria were predicted by both PR and SRK, where PR predicts sI hydrate and SRK predicts sII hydrate. A large deviation for  $z_{CO_2}$  is observed for SRK predictions, compared to PR predictions. The deviation in  $y_{CO_2}$  is relatively similar, where SRK is more accurate. Both PR and SRK predictions significantly deviates with respect to the aqueous phase composition from the reference, with PR predictions being most accurate.
- Row 7 and 8 lists 3 points where SRK predicts sI. It may be observed that  $z_{CO_2}$  calculated from SRK and PR are similar. The absolute deviation with respect to listed  $z_{CO_2}$  in the reference is also small. It may additionally be observed from Table 4.4 that the deviation in  $y_{CO_2}$  is larger for SRK predictions than PR predictions.

It is again difficult to determine a definite trend regarding the distribution of CO<sub>2</sub> in the hydrate phase. However, based upon the deviations calculated with respect to the listed hydrate composition by Belandria et al. (2011) [48], it seems that the hydrate phase is more accurately predicted by PR.

Belandria et al. (2011) compared their compositional findings with predictions from the CSMGem software. Calculated average absolute relative deviation is listed for 19 measurements (L<sub>w</sub>-H-V equilibria). The average absolute relative deviation for y<sub>CO<sub>2</sub></sub> is listed as 9.7, while the average absolute relative deviation for z<sub>CO<sub>2</sub></sub> is listed as 20.3% [48]. Comparing these values with the 21 points calculated from PR predictions (L<sub>w</sub>-H-V equilibria), it may be observed that PVTsim predictions utilizing PR results in a larger deviation for y<sub>CO<sub>2</sub></sub>, but a lower deviation for z<sub>CO<sub>2</sub></sub>.

There is always a degree of uncertainty related to experimental results. Belandria et al. (2011) lists the uncertainty in regards to the composition of the vapor phase to be less than 1%. The uncertainty of the liquid and hydrate phase are additionally stated by the authors to be less than 1%. Based upon the calculated deviations with respect to the phase compositions listed by Belandria et al. (2011), it seems that the phase compositions predicted by PVTsim are relatively inaccurate.

## 5.2 Accuracy of PVTsim predictions

Predicted PT curves from SRK and PR are visible in Fig. 4.10 and Fig. 4.11, and have been plotted with  $L_w$ -H-V equilibrium measurements listed in Sloan and Koh (2008).

In Figure 4.10 there is not a significant difference between SRK and PR as all equilibrium data is located on or close to the predicted PT curves. The exception being equilibrium measurements from Ohgaki et al. (1993), which not only deviates from the predicted PT curves but also from the rest of the literature data. It appears that PR is slightly more accurate as more data falls on the blue curve near the  $L_{CO_2}$  region, right before the sudden break of the PT curve due to it intersecting with the vapor pressure curve for  $CO_2$  (not shown - see Section 1.2.3). This is contrary to the observations made by Li and Yan (2008) who examined the predictive ability of several EOS. The authors states that SRK is generally superior in regards to vapor-liquid equilibrium (VLE) properties of pure  $CO_2$  [80].

Both SRK and PR predicts the PT curves for  $CH_4$  exceptionally well in Figure 4.11, where it appears that SRK is marginally better. None of the measured experimental equilibrium data deviates from any of the PT curves.

It is stated by Li and Yan (2008) that PR is the more accurate EOS in determining VLE properties of  $CO_2$ - $CH_4$  gas mixtures [80]. Diamantonis et al. (2013) states that both SRK and PR accurately predicts VLE properties of  $CO_2$ - $CH_4$  mixtures, with PR being listed with a marginally lower ARD% [81].

It should be noted that Li and Yan (2008) and Diamantonis et al. (2013) examined the accuracy of the respective equations of states on the basis of VLE measurements. Their results in regards to the more accurate may not be directly comparable to predictions on the basis of hydrate equilibrium conditions.

Based on the fact that SRK erroneously predicts sII for a range of  $CO_2/CH_4$  ratios (see Chapter 6), the PR EOS has been utilized for all calculations for the  $CO_2$ - $CH_4$ - $H_2O$  system. It is also the selected EOS for pure components calculations, i.e., simple hydrates of  $CO_2$  and  $CH_4$ . This was to have a systematic approach to all predictions made in PVTsim.

The accuracy of PVTsim predictions for the  $CO_2$ - $CH_4$ - $H_2O$  system was presented in Section 4.2.2, and was based upon dissociation conditions measurements of mixed  $CO_2$ - $CH_4$  hydrates from the literature.

Ballard and Sloan (2003) has previously examined the predictive ability of several hydrate prediction programs, which includes PVTsim. PVTsim is listed as having an average absolute deviation in temperature of approximately 0.25 K for simple hydrates (632 points), and approximately 0.65 K for binary hydrates (747 pts.). The average absolute relative deviation in pressure is listed as less than 4% for simple hydrates (632 pts.), and above 15% for binary hydrates (747 pts.) [82]. The PVTsim version utilized in this study was version 3.0, while the latest version is PVTsim Nova 1 (the version preceding Nova 1 was PVTsim 21.2) [83].

Calsep has also extensively examined the accuracy of PVTsim predictions, where experimental equilibrium data have been compared with predictions from PVTsim. Version 20.2 with PR was utilized for all predictions [58]. To determine the deviation they utilized the same procedure as the one used in this thesis (Equation 2.6 and 2.7). The experimental dissociation value is however subtracted from the predicted value, a positive value thus means that PVTsim overestimates the listed dissociation value.

Predictions from PVTsim agrees well with measured dissociation conditions for simple CH<sub>4</sub> hydrates according to the report by Calsep. The average relative deviation in pressure is listed in the report as 2.628% for 166 experimental points (0.0053 – 816 MPa range). The average deviation in temperature is listed as -0.69 K (190 – 318.4 K range) [58]. An average absolute relative deviation in pressure of 10.76%, and an average absolute deviation in temperature of 1.26 K was calculated from the data listed.

The largest deviations for both temperature and pressure predictions in regards to CH<sub>4</sub> hydrates are for measurements below the freezing point of water, or at pressures above 100 MPa. A deviation in temperature of -0.06 K and a relative deviation in pressure of -0.829% was calculated from the data considering only measurements made above the freezing point of water, and at pressures below 100 MPa (120 pts.). An average absolute relative deviation in pressure of 3.38%, and an average absolute deviation in temperature of 0.32 K was respectively calculated from the same data.

PVTsim has a poor predictive ability with respect to dissociation conditions for CO<sub>2</sub> hydrates. The relative deviation in pressure is listed in the report as 31.174% for 370 points (5.35 · 10<sup>-4</sup> MPa – 494 MPa range). The average deviation in temperature is listed in the report as 2.14 K for 364 points (151.5 K - 298.3 K range) [83]. An average absolute relative deviation in pressure of 66.57%, and an average absolute deviation in temperature of 2.66 K was calculated from the same data.

The largest deviations for both temperature and pressure predictions in regards to CO<sub>2</sub> hydrates are for measurements below the freezing point of water, or at pressures above the vapor pressure curve of CO<sub>2</sub>. The deviation in temperature and relative deviation in pressure was calculated to 0.19 K and -0.02% when considering only experimental data above the freezing point of water, and below the vapor pressure curve of CO<sub>2</sub>. An average absolute deviation in temperature of 0.32 K, and an average absolute relative deviation in pressure of 5.43% was calculated from the same data (170 pts.)

A total of 73 experimental points for mixed CO<sub>2</sub>-CH<sub>4</sub> hydrates from four sources are additionally listed in the report by Calsep. Table 5.1 lists the average deviation in temperature, absolute average deviation in temperature, relative deviation in pressure, and absolute relative deviation in pressure calculated from the data listed in the report.

Table 5.1: Deviations and relative deviations in temperature and pressure calculated from dissociation data for mixed CO<sub>2</sub>-CH<sub>4</sub> hydrates listed in the report by Calsep [58].

<b>Reference*:</b>	<b># exp. pts.</b>	<b>D T (K)</b>	<b>AD T (K)</b>	<b>RD% P</b>	<b>ARD% P</b>
Adisasmito et al. (1991) [38]	42	0.1	-1.30	0.2	1.77
Fan and Guo (1999) [42]	9	-0.3	3.17	0.6	8.14
Unruh and Katz (1949) [37]	17	-0.2	2.12	0.3	3.12
Hachikubo et al. (2002) [84]	5	1.2	-5.58	1.2	5.58
<b>Weighted average:</b>		0.1	-0.25	0.3	3.13

\* From the reference list in the report.

Table 4.5 in Section 4.2.2 list the calculated deviation in temperature and pressure of PVTsim predictions from experimental measurements of mixed CO<sub>2</sub>-CH<sub>4</sub> hydrates performed in this thesis. PVTsim generally predicts a higher pressure than the measured dissociation pressure, with the exception of 40 measurements from Belandria et al. (2011) [48].

This might be due to the fact that the composition is not exact for the other studies listed, as any dissolved species are neglected when approximating the total composition (Section 2.2.4). A higher CO<sub>2</sub> content would yield a lower predicted pressure by PVTsim, which might be closer to the experimental pressures listed in the various studies. Even when approximating the total system composition, PVTsim estimates the equilibrium conditions for mixed CO<sub>2</sub>-CH<sub>4</sub> hydrates exceptionally well according to the calculations performed.

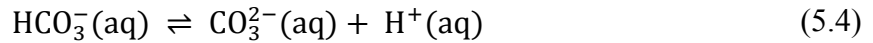
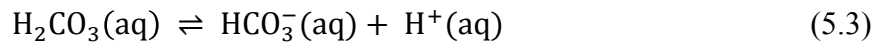
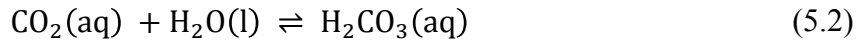
The weighted absolute deviation in temperature listed in Table 4.4 is significantly less than what was reported by Ballard and Sloan (2008) [82]. The weighted average absolute relative deviation in pressure listed in Table 4.4 is additionally almost 1/3 of the value stated by Ballard and Sloan (2008) [82].

The weighted average deviation and absolute average deviation in temperature listed in Table 4.5 is close to the weighted average calculated from the data listed in the report by Calsep (Table 5.1) [58]. The RD% and ARD% in pressure listed in Table 4.4 is somewhat higher than what was calculated from the data listed in the report by Calsep. The number of experimental data points examined in this thesis is however twice as many (152 vs. 73). Calsep may additionally have considered dissolved species when determining the system composition, and may thus have utilized a more accurate system composition when performing their simulations.

As a closing comment, it should be noted that the studied phase equilibrium data which has been utilized to determine the accuracy of PVTsim may not always be reliable. The experimental procedures utilized by the respective authors have not been taken into account when performing the previously mentioned calculations. There is always a degree of uncertainty related to experimental results, which should be taken into consideration regarding the results presented.

### 5.3 Experiments performed at the University of Bergen

A significant decrease in pressure can be observed for all CO<sub>2</sub> experiments after gas injection, which is due to the reduction in temperature (gas contraction), but mainly because of the dissolution of CO<sub>2</sub> species in water. The solubility of CO<sub>2</sub> in water is significantly higher than what is observed for other nonpolar molecules, e.g. CH<sub>4</sub>. This is due to the acid/base reaction CO<sub>2</sub> has with water, where the dissolution of CO<sub>2</sub> in water results in the following dissolved species [85]:



As an example to describe the solubility difference between CO<sub>2</sub> and CH<sub>4</sub>, a fluid with a 9:1 ratio of water to vapor (CO<sub>2</sub> or CH<sub>4</sub>) was flashed in PVTsim (aqueous flash) at 3 MPa and 293.15 K. The fraction of CO<sub>2</sub> in the aqueous phase ( $x_{\text{CO}_2}$ ) at these conditions is  $1.761 \cdot 10^{-2}$ , while the fraction of CH<sub>4</sub> in the aqueous phase ( $x_{\text{CH}_4}$ ) at these conditions is  $7.4 \cdot 10^{-4}$  [11]. A significant difference is observed between them.

In the Previous CO<sub>2</sub> hydrate experiments by Vaular (2011) and Corak (2011) a constant pressure was applied during cool down, to avoid the significant decrease in pressure due to CO<sub>2</sub> dissolution [9, 10]. However, this procedure could not be utilized as the objective for the experiments performed in this thesis was to control the system composition.

From the experimental data for experiment 3 and 4 (Fig. A.4 and A.6), it can be concluded that the full pressure of the CO<sub>2</sub> flask should be utilized when injecting gas (limited to ~ 5.0 MPa). The pressure reduction associated with the reduction in temperature and dissolution of CO<sub>2</sub> species is additionally relatively rapid, and there should be no risk of crossing the vapor-pressure line of CO<sub>2</sub>.

The unusual pressure data in experiment 1 and 3 (Fig. A.1 and A.3) were not observed for subsequent experiments. In some cases the pressure data displayed one or two extreme outliers (pressure above the maximum pressure recorded during gas injection), these have been removed from the time- and PT traces which are presented.

Less water was utilized in Experiment 8 and 9 (50 ml), with CH<sub>4</sub> as the hydrate former. Due to the lesser amount of water and the lower solubility of CH<sub>4</sub>, a greater amount of hydrates is probably formed in these experiments compared to the CO<sub>2</sub> experiments.

From the time traces of both experiments, a decrease in temperature is observed when the stirring of the system was off. The decrease in temperature observed might be because hydrate formation ceases when there is no agitation of the system. When the stirring is off, there is no continuous mix of the various phases in the system. The temperature increases again when the stirrer is turned on, as hydrate formation is again initiated when the phases again are thoroughly mixed.

A significant deviation in the experimental PT trace is observed for experiment 8 during system heating, with respect to the predicted PT curve by PVTsim. It is hypothesized that the reason for this deviation is due to the heating rate being too high for accurate dissociation of the hydrates formed. The heating rate is not slow enough to dissociate the hydrates gradually, and the system is not a thermodynamic equilibrium where the experimental PT trace deviates during system heating. Tohidi et al. (2000) states that a step heating is more accurate than continuous heating, where the error related to continuous heating is a function of the heating rate applied [86].

The dissociation data for experiment 9 does however not display the same deviation, even though the same rate was employed (1 K per hour). Even though experiment 8 and 9 displays different PT traces, it is recommended to utilize a slower heating rate for further experiments on the system. A higher heating rate will however significantly increase the time for each hydrate experiment, and a compromise has to be made between accurate dissociation data and the duration of experiments. It is recommended to at least utilize a heating rate of 2 K per hour based on the deviations observed for experiment 8 (and experiment 13). This rate was utilized for experiment 10 and 12 in this thesis. Further adjustments to the heating rate could be made on the basis of observations from dissociation data acquired from future experiments.

As the same amount of H<sub>2</sub>O was utilized for Experiment 5 and 11 (CO<sub>2</sub> and CH<sub>4</sub> hydrate respectively), the experimental data may be compared. For comparisons sake, the pressure and temperature time traces for the two experiments have been plotted together, and are presented in the figure below.



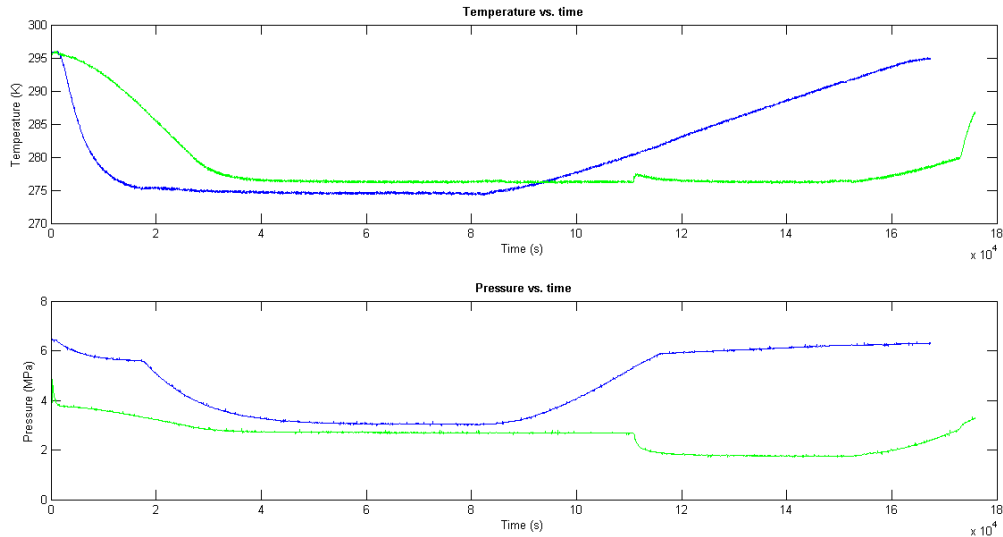


Figure 5.1: Pressure- and temperature time traces of experiment 5 and 11 (CO<sub>2</sub> and CH<sub>4</sub> respectively). The blue curve represents CH<sub>4</sub> data, and the green curve represents CO<sub>2</sub> data.

The solubility difference between CO<sub>2</sub> and CH<sub>4</sub> is clearly visible, where the pressure time trace for CO<sub>2</sub> displays a more drastic decrease in pressure from initial pressure, compared to the corresponding decrease in pressure after gas injection for the CH<sub>4</sub> experiment.

Hydrate formation occurs between 10-12 · 10<sup>4</sup> seconds for experiment 5, while hydrate formation occurs at approximately 2 · 10<sup>4</sup> for experiment 11, i.e., a significant difference in induction time is observed. Hydrate nucleation is generally thought to be stochastic, which may explain the large difference in induction times observed between the two experiments (Section 1.2.4).

Larger thermodynamic driving forces (temperature and pressure) are present in experiment 11. A pressure of approximately 6 MPa is observed before hydrate formation for experiment 11, compared to a pressure of approximately 3 MPa for experiment 5. A lower temperature was additionally appointed during cool down for experiment 11 in comparison to experiment 5, with 273.15 and 276.15 K respectively. Higher thermodynamic driving forces are believed to reduce the induction period, and consequently promote the onset of hydrate nucleation and subsequent hydrate growth [4].

Comparing the pressure drop associated with the incorporation of gas in the hydrate structures, it may be observed that the pressure drop associated CO<sub>2</sub> hydrate formation is more rapid compared to the pressure drop associated with CH<sub>4</sub> hydrate formation.

This is hypothesized to be because of the solubility difference between CO<sub>2</sub> and CH<sub>4</sub>. Hydrate formation is initiated at the vapor-water interface for these hydrate formers (Section 1.2.4). Due to dissolution of CO<sub>2</sub> in water, a higher concentration of CO<sub>2</sub> species at the interface is probable compared to the interface between H<sub>2</sub>O and CH<sub>4</sub>. The relatively rapid drop in pressure is also observed for the other successful CO<sub>2</sub> experiment (Experiment 2). The other successful CH<sub>4</sub> experiments (8-10) is characterized by the same gradual drop in pressure which was observed for experiment 11.

The associated temperature increase related to the exothermic heat of hydrate formation is not as pronounced for experiment 11 as for experiment 5. This is also the case for the other CH<sub>4</sub> experiments compared to the CO<sub>2</sub> experiments. It was proposed in the preceding paragraph that a higher concentration of CO<sub>2</sub> species at the interface is probable compared to the interface between H<sub>2</sub>O and CH<sub>4</sub>, due to the larger amount of dissolved CO<sub>2</sub> species. This might cause a higher formation rate for CO<sub>2</sub> hydrates, which might also explains the more pronounced increase in temperature associated with CO<sub>2</sub> hydrate formation observed in the temperature traces presented.

For the mixed CO<sub>2</sub>-CH<sub>4</sub> hydrate experiments presented, hydrate formation is clearly evident by the temperature increase and simultaneous pressure drop in the pressure- and time traces. The observed pressure drop in the pressure traces is more similar to the pressure drop observed in the pressure traces for the pure CO<sub>2</sub> experiments. This is again hypothesized to be due to the concentration of dissolved CO<sub>2</sub> species at the interface.

For the temperature traces for the mixed hydrate it seems that hydrate formation occurs relatively fast, where it in all cases appear before the system reaches its set temperature (274 K for all experiments). This is probably due to the high thermodynamic driving forces present in the system.

In the PT traces for all the mixed hydrate experiments it is clearly evident that the experimental dissociation line is located between the simple CH<sub>4</sub>- and CO<sub>2</sub> hydrate PT curves. The PT curves simulated to fit the experimental PT data additionally results in a system composition which contains both CO<sub>2</sub> and CH<sub>4</sub> species. All PT curves predicted in PVTsim fits the experimental PT data accurately, where the experimental dissociation data again follow the predicted PT curves during heating. The exception being experiment 13, where the experimental data deviates from the predicted curve at approximately 280 K. A slower heating rate might result in a more accurate dissociation curve, as previously explained.

Due to the lack of feed gas composition because of the previously mentioned non-mixed volume, no further conclusive statements can be made in regards to the mixed hydrate experiments presented.

For all the hydrate experiments performed, a low uncertainty can be considered in regards to the experimental data acquired. The error in the temperature and pressure sensors was previously presented in Section 3.1.4. This corresponds to  $\pm 0.2$  K, and  $\pm 0.1\% \pm 0.01$  MPa, as the units are converted from  $^{\circ}\text{C}$  and bar respectively. The presence of the non-mixed volume discovered is the largest uncertainty, where the listed system composition in Table 5.2 consequently has a large degree of uncertainty.

With the exception of experiment 8 and 13, all experiments accurately follows the predicted PT curve by PVTsim during dissociation. In the experiments presented where the experimental PT trace follows the predicted PT curve, it is proposed that the systems are essentially at three-phase  $L_w$ -H-V conditions during the entire heating period. When the experimental PT traces “breaks off” at high temperatures, all hydrates are dissociated. Having validated the predictive ability of PVTsim in the preceding section, it may be stated that the updated hydrate cell for the most part generate accurate PT data for the experiments performed. Table 4.8 additionally lists the determined dissociation point for the hydrate experiments performed, i.e., the point where the last hydrate crystal melts from the system (Section 1.2.4). It has been determined from the experimental PT traces, by the method proposed by Gjertsen and Fadnes by fitting straight lines to the dissociation curve and the curve after full dissociation [87]. It may be observed that PVTsim accurately predict the dissociation conditions for the experiments performed (with the exception of experiment 8 and 13).

Table 5.2: Determined dissociation conditions for the experiments performed at UiB.

#	$T_{\text{exp}}$	$P_{\text{exp}}$	$T_{\text{pred}}$	$P_{\text{pred}}$	D T (%)	AD T (K)	RD P (%)	ARD P (%)
2	281.3	3.46	281.23	3.50	0.1	0.1	-1.16	1.16
5	280.2	2.94	280.14	2.97	0	0	-0.95	0.95
8	282.4	5.32	280.30	6.64	2.1	2.1	-24.83	24.83
9	280.5	5.17	280.03	5.43	0.5	0.5	-5.04	5.04
10	281.2	5.57	280.74	5.85	0.5	0.5	-5.11	5.11
11	281.5	5.83	281.17	6.03	0.3	0.3	-3.37	3.37
12	281.9	4.56	281.93	4.54	0	0	0.53	0.53
13	284.7	4.89	282.69	6.40	2	2	-30.9	30.9
15	282.1	4.60	282.11	4.60	0	0	-0.11	0.11
16	282.2	4.79	282.14	4.82	0.1	0.1	-0.62	0.62

Based on observations from the experiments performed, the following points summarize observations regarding experimental procedures, and should be considered when planning for eventual future experiments:

- Use the full gas cylinder pressure for simple CO<sub>2</sub> hydrate experiments.
- A minimum heating rate of 2 K per hour is recommended for accurate dissociation data.
- Stopping the stirring of the hydrate cell causes a decrease in temperature. It is however recommended to let the stirring motor cool down before system heating as the motor may shut down automatically if it is overheated. If the motor shuts down during system heating it may result in loss of dissociation data.

## 5.4 Experiments performed at Statoil

Measured dissociation conditions for the three experiments performed at Statoil is listed in Table 5.3. The deviation in temperature, absolute deviation in temperature, relative deviation in pressure, and absolute relative deviation in pressure with respect to predictions by PVTsim is additionally listed.

Table 5.3: Measured equilibrium conditions for the experiments performed at Statoil. The composition for all experiments is 63.699% H<sub>2</sub>O, 32.671% CO<sub>2</sub> and 3.630% CH<sub>4</sub>

#	T <sub>exp</sub>	P <sub>exp</sub>	T <sub>pred</sub>	P <sub>pred</sub>	D T	AD T (K)	RD P (%)	ARD P (%)
A	285.55	7.70	285.95	6.94	-0.40	0.40	9.87	9.87
B	285.36	7.70	285.95	6.70	-0.59	0.59	12.99	12.99
C	285.54	7.00	285.60	6.93	-0.06	0.06	1.00	1.00
$\bar{x}$ :					-0.35	0.35	7.95	7.95

The deviation in the VT trace due to the hysteresis of the volume sensor was mentioned in Section 4.4. This does not influence the measured temperature and pressure. A low uncertainty is additionally expected in the variables measured (Section 3.6). The system composition is additionally very accurate, where both calculations and GC analysis on the gas mixture indicates a 90/10 mixture. The transferred gas volume additionally allows for an accurate determination of the system composition. The high deviation calculated for experiment A and B may be explained by the PT curve for the experiment, shown below.

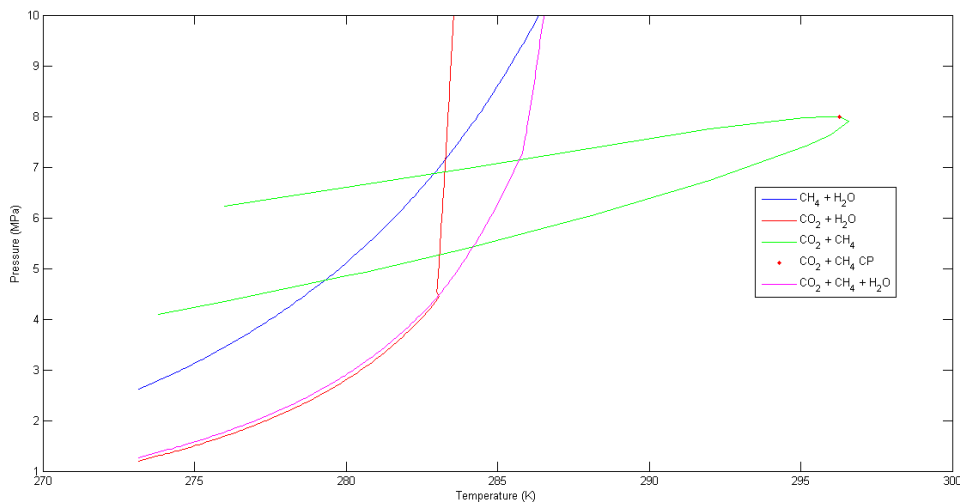


Figure 5.2: PT diagram with PT curves for simple CH<sub>4</sub> hydrate (blue), simple CO<sub>2</sub> hydrate (red), and mixed CO<sub>2</sub>-CH<sub>4</sub> hydrate (magenta). The PT curve for the mixed hydrates has been predicted in regards to the system composition for the experiments performed. The phase envelope for the CO<sub>2</sub>-CH<sub>4</sub> gas mixture is also included in the figure (green), with the critical point predicted as 296.27 K and 7.99 MPa [11].

In Figure 5.2 it may be observed that the gas mixture utilized for the experiments may undergo a phase transition, which may be observed from the green phase envelope predicted for the gas mixture. Vapor-liquid equilibria for the gas mixture were predicted inside the phase envelope when an ordinary PT flash was executed in PVTsim. A liquid phase is predicted above the phase envelope, while a vapor phase is predicted below.

The predicted hydrate PT curve for the mixed experiments is shown in Fig. 5.2 as the magenta colored curve. It may be observed that the steepness of the curve increases when the PT curve intersects with the upper part of the phase envelope for the gas mixture. This is also observed when the PT curve for pure CO<sub>2</sub> hydrate intersects with the pure CO<sub>2</sub> vapor pressure curve (Fig. 1.3 in Section 1.2.3).

Both experiment A and B were performed at a constant pressure of 7.70 MPa, where it may be observed that hydrate dissociation occurs in the liquid region from Fig 5.2 at these pressures. An inaccurate determination of the temperature or pressure in this region may consequently result in a large deviation with respect to the predicted dissociation conditions by PVTsim, due to the steep slope observed for the PT curve in this region.

Experiment C was performed at a constant pressure of 7.0 MPa, where it may be observed that hydrate dissociation occurs inside the predicted phase envelope in Fig. 5.2. The slope of the PT curve is in this region not as steep as what is observed for the PT curve in the liquid region. An inaccurate determination of the temperature or pressure in this region consequently results in a less pronounced deviation with respect to the predicted dissociation conditions by PVTsim.

The average deviations listed in Table 5.3 is significantly lower than what Ballard and Sloan (2004) determined [82]. But is somewhat higher than the average deviations listed in Table 4.5. However, many of the measurements used to determine the accuracy of PVTsim in Table 4.5 were for L<sub>w</sub>-H-V equilibria, which results in smaller deviations due to what was discussed in the previous paragraphs. It may be observed that large deviations are also calculated in Table A.2.4 and A.2.7 for some of the dissociation conditions examined, where PVTsim predicts a liquid phase (where the liquid phase is mainly CO<sub>2</sub>). It was also discussed in Section 5.2. on the basis of data listed in the report by Calsep [58], that larger deviations are usually calculated from predictions where CO<sub>2</sub> may be in a liquid phase. Which again is due to what was discussed in the preceding paragraphs.

# CHAPTER 6: CONCLUSION AND SUGGESTIONS FOR FURTHER WORK

## 6.1 Conclusion

The main purpose of this work was to examine the thermodynamic phase behavior of mixed CO<sub>2</sub>-CH<sub>4</sub> hydrates. The three-component CO<sub>2</sub>-CH<sub>4</sub>-H<sub>2</sub>O system has been examined with respect to simulations in PVTsim, and with respect to experiments performed at UiB and Statoil. The accuracy regarding PVTsim predictions has additionally been thoroughly reviewed. Conclusions drawn from the work may be summarized as follows:

It is hereby concluded that the SRK equation of state in PVTsim incorrectly predicts the sI/sII structural transition observed. This is based on simulations performed in PVTsim, the deviations calculated based on experimental data from Belandria et al. (2011), and literary evidence. It is hypothesized that the reason for the inaccurate structure predictions is because the fugacity parameter that determines the Langmuir constant for hydrate calculations is inaccurately estimated by the SRK EOS for CO<sub>2</sub>-CH<sub>4</sub>-H<sub>2</sub>O systems.

This may have implications related to flow assurance problems as the hydrate dissociation pressure (consequently the formation pressure) for the majority of cases is underestimated. This also has implications in regards to PVTsim as a simulation tool for quantitative research on mixed CO<sub>2</sub>-CH<sub>4</sub> hydrates as the composition of the hydrate phase is believed to be inaccurately predicted. It is therefore recommended to utilize the PR equation of state for all CO<sub>2</sub>-CH<sub>4</sub>-H<sub>2</sub>O simulations in PVTsim until Calsep corrects the observed error for the SRK equation of state.

It was observed that PVTsim accurately predicted dissociation conditions for simple CO<sub>2</sub>-, CH<sub>4</sub>-, and mixed CO<sub>2</sub>-CH<sub>4</sub> hydrates, based upon experimental dissociation conditions from the literature. The experiments performed at Statoil additionally indicates that PVTsim predicts the dissociation conditions of mixed CO<sub>2</sub>-CH<sub>4</sub> hydrates at high system pressures adequately. Predictions regarding L<sub>w</sub>-H-V equilibria exhibit smaller deviations than predictions regarding L<sub>w</sub>-H-L<sub>CO2</sub> equilibria. Overall it may be concluded that PVTsim can be utilized to validate any further experiments for the CO<sub>2</sub>-CH<sub>4</sub>-H<sub>2</sub>O system, where any predictions from PVTsim may be viewed as reliable.

The hydrate experiments performed at the University of Bergen indicates that the updated hydrate cell generates very accurate equilibrium data, based upon the validation by the PT curves predicted by PVTsim.

Due to the lack of accurate system composition it is difficult to conclude anything in regards to the mixed hydrate experiments, other than the fact that the hydrates formed are indeed mixed CO<sub>2</sub>-CH<sub>4</sub> hydrates based upon the experimental PT traces presented.

## **6.2: Suggestions for further work**

The updated experimental setup at UiB seemingly produce accurate equilibrium data. The main objective for further work should therefore be to generate additional experimental data for the CO<sub>2</sub>-CH<sub>4</sub>-H<sub>2</sub>O system. In this context it would be interesting to plan the experiments on the basis of experimental design, and to subsequently utilize various chemometric methods to possibly determine a trend for the data acquired.

In regards to future improvements to the experimental setup, it would be interesting to utilize the gas booster available at The Department of Chemistry. This would allow for a higher system pressure, where the pressure of the current setup is limited to the upper pressure in the gas cylinders.

Additional variables could also be introduced for the CO<sub>2</sub>-CH<sub>4</sub>-H<sub>2</sub>O system, however these variables have to be kept constant if it is desired to represent the CO<sub>2</sub>-CH<sub>4</sub>-H<sub>2</sub>O system in ternary phase diagrams. An example could be to form mixed CO<sub>2</sub>-CH<sub>4</sub> from water with a constant salinity or pH. The phase equilibria determined for these experiments could be compared with the phase equilibria of mixed CO<sub>2</sub>-CH<sub>4</sub> hydrates formed from pure water.

Compositional phase predictions by PVTsim has in this thesis been compared with listed phase compositions in the study by Belandria et al. (2011) [48]. The results generally indicates that PVTsim is less accurate in regards to compositional predictions. It would consequently be interesting to re-examine the compositional predictions by PVTsim as a function of controlled experiments. The vapor fraction could be analyzed through GC analysis, and subsequently be compared to vapor phase predictions by PVTsim. A material balance could additionally be utilized to determine the composition of the other phases, which could be compared to the other compositional phase predictions by PVTsim.



If the compositional phase predictions by PVTsim is found to be accurate, it would be interesting to simulate CH<sub>4</sub> recovery from a hydrate reservoir as a function of CO<sub>2</sub> injection by modeling the process through PVTsim simulations with Open Structure.

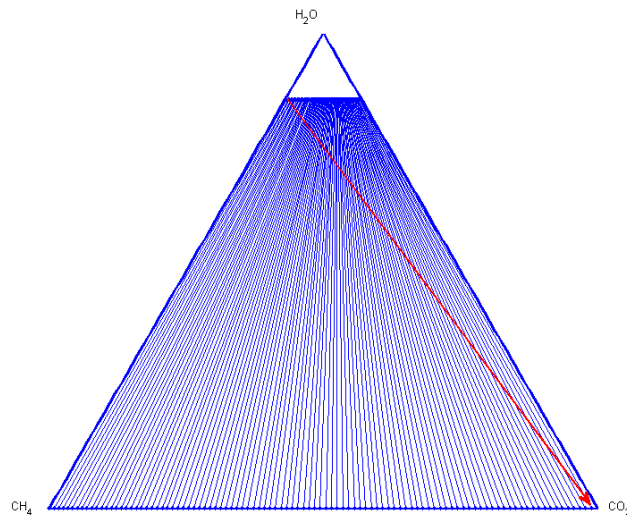


Figure 6.1: Ternary phase diagram for the CO<sub>2</sub>-CH<sub>4</sub>-H<sub>2</sub>O system simulated in PVTsim through Open Structure at 275 K and 3.0 MPa. Water content fixed at 50% during calculations.

In a CH<sub>4</sub> hydrate reservoir the composition is locked at the leftmost side of the ternary plot, the excess phase being vapor in the system which is modeled here. When CO<sub>2</sub> is injected into the reservoir, the concentration of CO<sub>2</sub> in the reservoir increases, and the overall composition consequently moves from a point along the CH<sub>4</sub>-H<sub>2</sub>O line which represents the reservoir, to the CO<sub>2</sub> vertex, illustrated with the red arrow. It would be interesting to review the distribution of the three components in the various phases predicted, in regards to any overall compositions located along the red arrow.

# APPENDIX A: RESULTS

## Appendix A.1: PVTsim simulations

Table A.1.1: Fluid values for manual simulations performed in PVTsim. Water content fixed at 50.000%.

<b>a) T = 274 K and P = 3.0 MPa</b>		<b>b) T = 274 K and P = 4.5 Mpa</b>		<b>c) T = 274 K and P = 5.5 Mpa</b>	
<u>CO<sub>2</sub> (%)</u>	<u>CH<sub>4</sub> (%)</u>	<u>CO<sub>2</sub> (%)</u>	<u>CH<sub>4</sub> (%)</u>	<u>CO<sub>2</sub> (%)</u>	<u>CH<sub>4</sub> (%)</u>
0.000	50.000	0.000	50.000	0.000	50.000
4.842	45.158	4.877	45.123	4.894	45.106
9.842	40.158	9.877	40.123	9.894	40.106
14.842	35.158	14.877	35.123	14.894	35.106
19.842	30.158	19.877	30.123	19.894	30.106
24.842	25.158	24.877	25.123	24.894	25.106
29.842	20.158	29.877	20.123	29.894	20.106
30.559	19.441	30.393	19.607	30.865	19.135
35.559	14.441	35.393	14.607	35.865	14.135
40.559	9.441	40.393	9.607	40.865	9.135
45.559	4.441	45.393	4.607	45.865	4.135
50.000	0.000	50.000	0.000	50.000	0.000
<b>d) T = 277 K and P = 3.0 Mpa</b>		<b>e) T = 277 K and P = 4.5 Mpa</b>		<b>f) T = 277 K and P = 5.5 Mpa</b>	
<u>CO<sub>2</sub> (%)</u>	<u>CH<sub>4</sub> (%)</u>	<u>CO<sub>2</sub> (%)</u>	<u>CH<sub>4</sub> (%)</u>	<u>CO<sub>2</sub> (%)</u>	<u>CH<sub>4</sub> (%)</u>
0.000	50.000	0.000	50.000	0.000	50.000
5.000	45.000	4.924	45.076	4.957	45.043
9.113	40.887	9.924	40.076	9.957	40.043
14.113	35.887	14.924	35.076	14.957	35.043
19.113	30.887	19.924	30.076	19.957	30.043
24.113	25.887	24.924	25.076	24.957	25.043
29.113	20.887	29.924	20.076	29.957	20.043
31.274	18.726	30.982	19.018	31.388	18.612
36.274	13.726	35.982	14.018	36.388	13.612
41.274	8.726	40.982	9.018	41.388	8.612
46.274	3.726	45.982	4.018	46.388	3.612
50.000	0.000	50.000	0.000	50.000	0.000
<b>g) T = 280 K and P = 3.0 Mpa</b>		<b>h) T = 280 K and P = 4.5 Mpa</b>		<b>i) T = 280 K and P = 5.5 Mpa</b>	
<u>CO<sub>2</sub> (%)</u>	<u>CH<sub>4</sub> (%)</u>	<u>CO<sub>2</sub> (%)</u>	<u>CH<sub>4</sub> (%)</u>	<u>CO<sub>2</sub> (%)</u>	<u>CH<sub>4</sub> (%)</u>
0.000	50.000	0.000	50.000	0.000	50.000
5.000	45.000	5.000	45.000	5.000	45.000
10.000	40.000	6.281	43.719	5.066	44.934
15.000	35.000	11.281	38.719	10.066	39.934
20.000	30.000	16.281	33.719	15.066	34.934
25.000	25.000	21.281	28.719	20.066	29.934
30.000	20.000	26.281	23.719	25.066	24.934
35.000	15.000	31.160	18.840	30.066	19.934
40.000	10.000	36.160	13.840	31.494	18.506
45.000	5.000	41.160	8.840	36.494	13.506
45.329	4.671	46.160	3.840	41.494	8.506
50.000	0.000	50.000	0.000	46.494	3.506
				50.000	0.000

Table A.1.2:  $y_{CO_2}$  calculated from predicted phase compositions by PVTsim for both the SRK and the PR EOS. Original fluid compositions are listed in Table A.1.1.

<b>a) T = 274 K and P = 3.0 Mpa</b>		<b>b) T = 274 K and P = 4.5 Mpa</b>		<b>c) T = 274 K and P = 5.5 Mpa</b>	
<u>SRK</u>	<u>PR</u>	<u>SRK</u>	<u>PR</u>	<u>SRK</u>	<u>PR</u>
0.000	0.000	0.000	0.000	0.000	0.000
0.085	0.083	0.086	0.085	0.086	0.085
0.168	0.174	0.170	0.177	0.171	0.178
0.271	0.270	0.273	0.273	0.275	0.275
0.376	0.369	0.379	0.372	0.381	0.375
0.481	0.470	0.485	0.474	0.487	0.477
0.587	0.574	0.591	0.578	0.594	0.581
0.602	0.589	0.602	0.588	0.614	0.601
0.692	0.693	0.691	0.693	0.704	0.706
0.798	0.799	0.796	0.798	0.737	0.736
0.904	0.905	0.839	0.834	0.928	0.930
1.000	1.000	0.000	0.985	0.000	0.985
<b>d) T = 277 K and P = 3.0 Mpa</b>		<b>e) T = 277 K and P = 4.5 Mpa</b>		<b>f) T = 277 K and P = 5.5 Mpa</b>	
<u>SRK</u>	<u>PR</u>	<u>SRK</u>	<u>PR</u>	<u>SRK</u>	<u>PR</u>
0.000	0.000	0.000	0.000	0.000	0.000
0.098	0.098	0.087	0.086	0.088	0.087
0.179	0.179	0.172	0.178	0.173	0.180
0.257	0.256	0.275	0.274	0.277	0.277
0.361	0.355	0.381	0.374	0.383	0.376
0.467	0.456	0.487	0.476	0.489	0.479
0.572	0.559	0.592	0.579	0.595	0.582
0.617	0.604	0.614	0.601	0.626	0.612
0.708	0.709	0.704	0.706	0.715	0.717
0.813	0.815	0.809	0.811	0.780	0.778
0.920	0.921	0.888	0.883	0.935	0.937
1.000	1.000	0.000	0.985	0.000	0.985
<b>g) T = 280 K and P = 3.0 Mpa</b>		<b>h) T = 280 K and P = 4.5 Mpa</b>		<b>i) T = 280 K and P = 5.5 Mpa</b>	
<u>SRK</u>	<u>PR</u>	<u>SRK</u>	<u>PR</u>	<u>SRK</u>	<u>PR</u>
0.000	0.000	0.000	0.000	0.000	0.000
0.098	0.098	0.097	0.097	0.089	0.088
0.196	0.196	0.122	0.122	0.090	0.089
0.295	0.295	0.200	0.204	0.176	0.182
0.395	0.394	0.304	0.302	0.280	0.279
0.494	0.494	0.410	0.402	0.386	0.379
0.594	0.594	0.516	0.504	0.492	0.481
0.695	0.695	0.619	0.605	0.598	0.585
0.796	0.796	0.709	0.710	0.628	0.615
0.897	0.894	0.814	0.815	0.718	0.719
0.904	0.901	0.919	0.920	0.823	0.820
1.000	1.000	0.986	0.986	0.823	0.820
				0.000	0.985

Table A.1.3:  $z_{CO_2}$  calculated from predicted phase compositions by PVTsim for both the SRK EOS and the PR EOS. Original fluid compositions are listed in Table A.1.1.

<b>a) T = 274 K and P = 3.0 Mpa</b>			<b>b) T = 274 K and P = 4.5 Mpa</b>			<b>c) T = 274 K and P = 5.5 Mpa</b>		
<u>SRK (sI)</u>	<u>SRK (sII)</u>	<u>PR (sI)</u>	<u>SRK (sI)</u>	<u>SRK (sII)</u>	<u>PR (sI)</u>	<u>SRK (sI)</u>	<u>SRK (sII)</u>	<u>PR (sI)</u>
0.000	0.000	0.000	0.000	0.000	0.000	0.000	0.000	0.000
0.022	0.034	0.023	0.022	0.033	0.023	0.022	0.033	0.023
-	0.048	0.044	-	0.047	0.043	-	0.047	0.042
-	0.059	0.061	-	0.059	0.060	-	0.059	0.059
-	0.069	0.075	-	0.069	0.074	-	0.068	0.073
-	0.079	0.088	-	0.078	0.087	-	0.078	0.086
-	0.088	0.100	-	0.088	0.099	-	0.087	0.097
0.103	0.089	0.101	0.102	0.089	0.100	0.102	0.089	0.099
0.112	-	0.112	0.112	-	0.110	0.111	-	0.110
0.122	-	0.121	0.122	-	0.120	0.114	-	0.113
0.132	-	0.131	0.126	-	0.124	0.117	-	0.115
0.139	-	0.139	0.140	-	0.139	0.140	-	0.140
<b>d) T = 277 K and P = 3.0 Mpa</b>			<b>e) T = 277 K and P = 4.5 Mpa</b>			<b>f) T = 277 K and P = 5.5 Mpa</b>		
<u>SRK (sI)</u>	<u>SRK (sII)</u>	<u>PR (sI)</u>	<u>SRK (sI)</u>	<u>SRK (sII)</u>	<u>PR (sI)</u>	<u>SRK (sI)</u>	<u>SRK (sII)</u>	<u>PR (sI)</u>
0.000	0.000	0.000	0.000	0.000	0.000	0.000	0.000	0.000
-	-	-	0.022	0.033	0.023	0.022	0.033	0.023
-	0.048	-	-	0.047	0.043	-	0.047	0.042
-	0.057	0.058	-	0.058	0.060	-	0.058	0.059
-	0.067	0.073	-	0.068	0.074	-	0.068	0.073
-	0.076	0.086	-	0.077	0.087	-	0.077	0.086
-	0.085	0.098	-	0.087	0.098	-	0.086	0.097
0.103	0.089	0.102	0.102	0.089	0.101	0.102	0.089	0.100
0.112	-	0.113	0.111	-	0.111	0.111	-	0.111
0.122	-	0.122	0.121	-	0.121	0.117	-	0.117
0.131	-	0.132	0.129	-	0.128	0.119	-	0.119
0.137	-	0.138	0.139	-	0.140	0.139	-	0.140
<b>g) T = 280 K and P = 3.0 Mpa</b>			<b>h) T = 280 K and P = 4.5 Mpa</b>			<b>i) T = 280 K and P = 5.5 Mpa</b>		
<u>SRK (sI)</u>	<u>SRK (sII)</u>	<u>PR (sI)</u>	<u>SRK (sI)</u>	<u>SRK (sII)</u>	<u>PR (sI)</u>	<u>SRK (sI)</u>	<u>SRK (sII)</u>	<u>PR (sI)</u>
0.000	0.000	0.000	0.000	0.000	0.000	0.000	0.000	0.000
-	-	-	-	-	-	0.022	-	0.023
-	-	-	-	0.039	-	0.022	0.033	0.023
-	-	-	-	0.049	0.047	-	0.046	0.042
-	-	-	-	0.060	0.063	-	0.057	0.059
-	-	-	-	0.070	0.077	-	0.067	0.073
-	-	-	-	0.079	0.090	-	0.076	0.086
-	-	-	0.100	0.088	0.101	-	0.085	0.097
-	-	-	0.110	-	0.111	0.100	0.088	0.100
-	-	0.129	0.120	-	0.122	0.109	-	0.111
0.127	-	0.130	0.130	-	0.132	0.120	-	0.121
0.135	-	0.138	0.137	-	0.140	0.120	-	0.121
						0.137	-	0.140

Table A.1.4: Predicted dissociation conditions by PVTsim based on experimental data listed in Belandria et al. (2011) [48]. PR EOS utilized.

Mole% in feed			$T_{\text{exp}}$ (K)	$P_{\text{exp}}$ (MPa)	$T_{\text{pred}}$ (K)	$P_{\text{pred}}$ (MPa)	D T	RD% P	AD T	ARD% P	Strc.
H <sub>2</sub> O	CO <sub>2</sub>	CH <sub>4</sub>									
87.100	2.657	10.243	279.3	4.03	279.35	4.01	-0.05	0.50	0.1	0.50	a
96.100	0.803	3.097	282.0	5.48	281.78	5.61	0.22	-2.37	0.2	2.37	a
97.500	0.515	1.985	285.5	8.27	285.27	8.49	0.23	-2.66	0.2	2.66	a
87.700	5.855	6.445	277.9	2.72	277.49	2.85	0.41	-4.78	0.4	4.78	a
95.900	1.952	2.148	279.8	3.61	279.44	3.77	0.36	-4.43	0.4	4.43	a
97.300	1.285	1.415	285.0	6.09	283.55	7.28	1.45	-19.54	1.4	19.54	a
87.700	9.151	3.149	279.0	2.72	278.84	2.78	0.16	-2.21	0.2	2.21	a
95.600	3.274	1.126	280.1	3.21	279.83	3.32	0.27	-3.43	0.3	3.43	a
97.200	2.083	0.717	283.2	4.70	282.43	5.21	0.77	-10.85	0.8	10.85	a
$\bar{x}$ :							<b>0.4</b>	<b>-5.53</b>	<b>0.4</b>	<b>5.64</b>	

<sup>a</sup> Forms sI when flashed at  $T_{\text{exp}}$  and  $P_{\text{pred}}$

Table A.1.5: Predicted dissociation conditions by PVTsim based on experimental data listed in Belandria et al. (2011) [48]. SRK utilized.

Mole% in feed			$T_{\text{exp}}$ (K)	$P_{\text{exp}}$ (MPa)	$T_{\text{pred}}$ (K)	$P_{\text{pred}}$ (MPa)	D T	RD% P	AD T	ARD% P	Strc.
H <sub>2</sub> O	CO <sub>2</sub>	CH <sub>4</sub>									
87.100	2.657	10.243	279.3	4.03	279.69	3.86	-0.4	4.22	0.4	4.22	b
96.100	0.803	3.097	282.0	5.48	281.73	5.66	0.3	-3.28	0.3	3.28	b
97.500	0.515	1.985	285.5	8.27	284.92	8.86	0.6	-7.13	0.6	7.13	a
87.700	5.855	6.445	277.9	2.72	277.8	2.76	0.1	-1.47	0.1	1.47	b
95.900	1.952	2.148	279.8	3.61	279.85	3.59	-0.1	0.55	0.1	0.55	b
97.300	1.285	1.415	285.0	6.09	283.8	7.12	1.2	-16.91	1.2	16.91	b
87.700	9.151	3.149	279.0	2.72	278.55	2.89	0.4	-6.25	0.4	6.25	a
95.600	3.274	1.126	280.1	3.21	279.49	3.47	0.6	-8.10	0.6	8.10	b
97.200	2.083	0.717	283.2	4.70	282.4	5.23	0.8	-11.28	0.8	11.28	b
$\bar{x}$ :							<b>0.4</b>	<b>-5.52</b>	<b>0.5</b>	<b>6.58</b>	

<sup>a</sup> Forms sI when flashed at  $T_{\text{exp}}$  and  $P_{\text{pred}}$

<sup>b</sup> Forms sII when flashed at  $T_{\text{exp}}$  and  $P_{\text{pred}}$

Table A.1.6: Predicted dissociation conditions by PVTsim based on experimental data from Belandria et al. (2011) [48]. PR EOS utilized.

Mole% in feed			T <sub>exp</sub> (K)	P <sub>exp</sub> (MPa)	T <sub>pred</sub> (K)	P <sub>pred</sub> (MPa)	D T	RD% P	AD T	ARD% P
H <sub>2</sub> O	CO <sub>2</sub>	CH <sub>4</sub>								
87.036	2.921	10.043	273.6	2.234	273.86	2.17	-0.26	2.86	0.3	2.86
96.091	0.881	3.028	273.6	2.416	274.15	2.28	-0.55	5.63	0.5	5.63
97.464	0.572	1.965	273.6	2.440	273.98	2.35	-0.38	3.69	0.4	3.69
87.719	6.167	6.114	273.6	1.844	274.14	1.74	-0.54	5.64	0.5	5.64
95.865	2.077	2.059	273.6	1.941	274.10	1.84	-0.50	5.20	0.5	5.20
97.348	1.332	1.320	273.6	2.048	274.18	1.92	-0.58	6.25	0.6	6.25
87.694	9.359	2.947	273.6	1.510	273.89	1.46	-0.29	3.31	0.3	3.31
95.609	3.339	1.052	273.6	1.607	274.15	1.51	-0.55	6.04	0.5	6.04
87.036	2.921	10.043	275.2	2.583	275.26	2.57	-0.06	0.50	0.1	0.50
96.091	0.881	3.028	275.2	2.712	275.26	2.70	-0.06	0.44	0.1	0.44
97.464	0.572	1.965	275.2	2.766	275.19	2.77	0.01	-0.14	0.0	0.14
87.719	6.167	6.114	275.2	2.123	275.42	2.07	-0.22	2.50	0.2	2.50
95.865	2.077	2.059	275.2	2.220	275.30	2.19	-0.10	1.35	0.1	1.35
97.348	1.332	1.320	275.2	2.400	275.58	2.30	-0.38	4.17	0.4	4.17
87.694	9.359	2.947	275.2	1.792	275.38	1.75	-0.18	2.34	0.2	2.34
95.609	3.339	1.052	275.2	1.865	275.42	1.82	-0.22	2.41	0.2	2.41
87.036	2.921	10.043	276.1	2.813	276.08	2.82	0.02	-0.25	0.0	0.25
96.091	0.881	3.028	276.1	3.025	276.31	2.96	-0.21	2.15	0.2	2.15
97.464	0.572	1.965	276.1	3.027	276.06	3.04	0.04	-0.43	0.0	0.43
87.719	6.167	6.114	276.1	2.318	276.21	2.29	-0.11	1.21	0.1	1.21
95.865	2.077	2.059	276.1	2.503	276.37	2.43	-0.27	2.92	0.3	2.92
97.348	1.332	1.320	276.1	2.690	276.59	2.54	-0.49	5.58	0.5	5.58
87.694	9.359	2.947	276.1	1.985	276.26	1.95	-0.16	1.76	0.2	1.76
95.609	3.339	1.052	276.1	2.174	276.72	2.02	-0.62	7.08	0.6	7.08
87.036	2.921	10.043	278.1	3.416	277.94	3.48	0.16	-1.87	0.2	1.87
96.091	0.881	3.028	278.1	3.631	278.05	3.65	0.05	-0.52	0.1	0.52
97.464	0.572	1.965	278.1	3.802	278.24	3.75	-0.14	1.37	0.1	1.37
95.865	2.077	2.059	278.1	3.037	278.08	3.05	0.02	-0.43	0.0	0.43
97.348	1.332	1.320	278.1	3.319	278.44	3.19	-0.34	3.89	0.3	3.89
87.694	9.359	2.947	278.1	2.450	278.05	2.47	0.05	-0.82	0.1	0.82
95.609	3.339	1.052	278.1	2.580	278.14	2.57	-0.04	0.39	0.0	0.39
87.036	2.921	10.043	279.2	3.565	278.34	3.91	0.86	-9.68	0.9	9.68
96.091	0.881	3.028	280.2	4.486	280.03	4.57	0.17	-1.87	0.2	1.87
97.464	0.572	1.965	280.2	4.655	280.15	4.68	0.05	-0.54	0.1	0.54
95.865	2.077	2.059	280.2	3.541	279.41	3.88	0.79	-9.57	0.8	9.57
97.348	1.332	1.320	280.2	4.109	280.30	4.06	-0.10	1.19	0.1	1.19
95.609	3.339	1.052	280.2	3.139	279.73	3.33	0.47	-6.08	0.5	6.08
97.243	2.097	0.660	280.2	3.481	280.14	3.51	0.06	-0.83	0.1	0.83
97.464	0.572	1.965	282.2	5.767	282.13	5.81	0.07	-0.75	0.1	0.75
97.464	0.572	1.965	284.2	7.190	284.12	7.26	0.08	-0.97	0.1	0.97
<b><math>\bar{x}</math>:</b>							<b>-0.1</b>	<b>1.1</b>	<b>0.3</b>	<b>2.9</b>

Table A.1.7: Predicted dissociation conditions from PVTsim based on experimental data from Belandria et al (2011) [48]. SRK EOS utilized.

Mole% in feed			T <sub>exp</sub> (K)	P <sub>exp</sub> (MPa)	T <sub>pred</sub> (K)	P <sub>pred</sub> (MPa)	D T	RD% P	AD T	ARD% P
H <sub>2</sub> O	CO <sub>2</sub>	CH <sub>4</sub>								
87.036	2.921	10.043	273.6	2.234	274.53	2.03	-0.9	9.13	0.9	9.13
96.091	0.881	3.028	273.6	2.416	274.67	2.15	-1.1	11.01	1.1	11.01
97.464	0.572	1.965	273.6	2.440	274.38	2.24	-0.8	8.20	0.8	8.20
87.719	6.167	6.114	273.6	1.844	274.54	1.66	-0.9	9.98	0.9	9.98
95.865	2.077	2.059	273.6	1.941	274.69	1.72	-1.1	11.39	1.1	11.39
97.348	1.332	1.320	273.6	2.048	274.87	1.77	-1.3	13.57	1.3	13.57
87.694	9.359	2.947	273.6	1.510	273.78	1.48	-0.2	1.99	0.2	1.99
95.609	3.339	1.052	273.6	1.607	274.02	1.53	-0.4	4.79	0.4	4.79
87.036	2.921	10.043	275.2	2.583	275.86	2.41	-0.7	6.70	0.7	6.70
96.091	0.881	3.028	275.2	2.712	275.72	2.57	-0.5	5.24	0.5	5.24
97.464	0.572	1.965	275.2	2.766	275.51	2.68	-0.3	3.11	0.3	3.11
87.719	6.167	6.114	275.2	2.123	275.76	1.99	-0.6	6.26	0.6	6.26
95.865	2.077	2.059	275.2	2.220	275.85	2.06	-0.7	7.21	0.7	7.21
97.348	1.332	1.320	275.2	2.400	276.22	2.13	-1.0	11.25	1.0	11.25
87.694	9.359	2.947	275.2	1.792	275.23	1.79	0.0	0.11	0.0	0.11
95.609	3.339	1.052	275.2	1.865	275.25	1.85	-0.1	0.80	0.1	0.80
87.036	2.921	10.043	276.1	2.813	276.64	2.66	-0.5	5.44	0.5	5.44
96.091	0.881	3.028	276.1	3.025	276.70	2.84	-0.6	6.12	0.6	6.12
97.464	0.572	1.965	276.1	3.027	276.31	2.96	-0.2	2.21	0.2	2.21
87.719	6.167	6.114	276.1	2.318	276.52	2.21	-0.4	4.66	0.4	4.66
95.865	2.077	2.059	276.1	2.503	276.87	2.29	-0.8	8.51	0.8	8.51
97.348	1.332	1.320	276.1	2.690	277.19	2.37	-1.1	11.90	1.1	11.90
87.694	9.359	2.947	276.1	1.985	276.08	1.99	0.0	-0.25	0.0	0.25
95.609	3.339	1.052	276.1	2.174	276.50	2.07	-0.4	4.78	0.4	4.78
87.036	2.921	10.043	278.1	3.416	278.39	3.31	-0.3	3.10	0.3	3.10
96.091	0.881	3.028	278.1	3.631	278.32	3.55	-0.2	2.23	0.2	2.23
97.464	0.572	1.965	278.1	3.802	278.33	3.71	-0.2	2.42	0.2	2.42
95.865	2.077	2.059	278.1	3.037	278.51	2.9	-0.4	4.51	0.4	4.51
97.348	1.332	1.320	278.1	3.319	278.96	3	-0.9	9.61	0.9	9.61
87.694	9.359	2.947	278.1	2.450	277.80	2.55	0.3	-4.08	0.3	4.08
95.609	3.339	1.052	278.1	2.580	277.86	2.66	0.2	-3.10	0.2	3.10
87.036	2.921	10.043	279.2	3.565	278.78	3.74	0.4	-4.91	0.4	4.91
96.091	0.881	3.028	280.2	4.486	280.18	4.5	0.0	-0.31	0.0	0.31
97.464	0.572	1.965	280.2	4.655	280.10	4.71	0.1	-1.18	0.1	1.18
95.865	2.077	2.059	280.2	3.541	279.79	3.72	0.4	-5.06	0.4	5.06
97.348	1.332	1.320	280.2	4.109	280.72	3.86	-0.5	6.06	0.5	6.06
95.609	3.339	1.052	280.2	3.139	279.38	3.5	0.8	-11.50	0.8	11.50
97.243	2.097	0.660	280.2	3.481	280.07	3.54	0.1	-1.69	0.1	1.69
97.464	0.572	1.965	282.2	5.767	281.94	5.95	0.3	-3.17	0.3	3.17
97.464	0.572	1.965	284.2	7.190	283.78	7.56	0.4	-5.15	0.4	5.15
<b><math>\bar{x}</math>:</b>							<b>-0.3</b>	<b>3.55</b>	<b>0.5</b>	<b>5.57</b>



Table A.1.9: Experimental phase compositions listed in the study by Belandria et al. (2011) [48].

#	Mole% in feed			Dissociation conditions		Experimental data (phase composition)				
	H <sub>2</sub> O	CO <sub>2</sub>	CH <sub>4</sub>	P (MPa)	T (K)	y(CO <sub>2</sub> )	Aqueous phase			
	H <sub>2</sub> O	CO <sub>2</sub>	CH <sub>4</sub>				H <sub>2</sub> O	CO <sub>2</sub>	CH <sub>4</sub>	z(CO <sub>2</sub> )
1	87.036	2.921	10.043	2.234	273.6	0.141	-	-	-	-
2	96.091	0.881	3.028	2.416	273.6	0.125	-	-	-	-
3	97.464	0.572	1.965	2.44	273.6	0.081	0.994	0.0055	0.0006	0.096
4	87.719	6.167	6.114	1.844	273.6	0.345	0.9898	0.0099	0.0003	0.549
5	95.865	2.077	2.059	1.941	273.6	0.288	0.9932	0.0062	0.0006	0.392
6	97.348	1.332	1.320	2.048	273.6	0.22	0.9902	0.0095	0.0003	0.294
7	87.694	9.359	2.947	1.51	273.6	0.63	0.9872	0.0127	0.0001	0.884
8	95.609	3.339	1.052	1.607	273.6	0.545	0.9871	0.0128	0.0001	0.801
9	87.036	2.921	10.043	2.583	275.2	0.166	0.9921	0.0071	0.0008	0.338
10	96.091	0.881	3.028	2.712	275.2	0.129	-	-	-	-
11	97.464	0.572	1.965	2.766	275.2	0.086	0.9961	0.003	0.0009	0.179
12	87.719	6.167	6.114	2.123	275.2	0.384	0.9889	0.0108	0.0003	0.65
13	95.865	2.077	2.059	2.22	275.2	0.302	0.9919	0.0075	0.0006	0.586
14	97.348	1.332	1.320	2.4	275.2	0.228	0.9889	0.0108	0.0003	0.366
15	87.694	9.359	2.947	1.792	275.2	0.657	0.9875	0.0123	0.0002	0.831
16	95.609	3.339	1.052	1.865	275.2	0.565	0.9884	0.0113	0.0003	0.752
17	87.036	2.921	10.043	2.813	276.1	0.179	0.9931	0.0062	0.0007	0.264
18	96.091	0.881	3.028	3.025	276.1	0.134	0.9957	0.0034	0.0009	0.239
19	97.464	0.572	1.965	3.027	276.1	0.096	0.9931	0.0062	0.0007	0.238
20	87.719	6.167	6.114	2.318	276.1	0.405	0.9883	0.0113	0.0004	0.644
21	95.865	2.077	2.059	2.503	276.1	0.315	0.9883	0.0113	0.0004	0.4
22	97.348	1.332	1.320	2.69	276.1	0.232	0.9883	0.0113	0.0004	0.312
23	87.694	9.359	2.947	1.985	276.1	0.669	0.984	0.0158	0.0002	0.877
24	95.609	3.339	1.052	2.174	276.1	0.579	0.9882	0.0114	0.0004	0.784
25	87.036	2.921	10.043	3.416	278.1	0.202	0.989	0.0088	0.0021	0.233
26	96.091	0.881	3.028	3.631	278.1	0.139	0.9917	0.0074	0.0009	0.225
27	97.464	0.572	1.965	3.802	278.1	0.103	0.9924	0.0068	0.0008	0.148
28	95.865	2.077	2.059	3.037	278.1	0.323	0.9871	0.0124	0.0004	0.457
29	97.348	1.332	1.320	3.319	278.1	0.233	0.987	0.0126	0.0004	0.273
30	87.694	9.359	2.947	2.45	278.1	0.694	-	-	-	-
31	95.609	3.339	1.052	2.58	278.1	0.609	0.9859	0.0137	0.0004	0.786
32	87.036	2.921	10.043	3.565	279.2	0.202	0.992	0.0071	0.0009	0.266
33	96.091	0.881	3.028	4.486	280.2	0.147	0.9898	0.0023	0.0079	0.307
34	97.464	0.572	1.965	4.655	280.2	0.108	0.9917	0.0013	0.007	0.245
35	95.865	2.077	2.059	3.541	280.2	0.344	0.9849	0.0146	0.0005	0.727
36	97.348	1.332	1.320	4.109	280.2	0.235	0.9881	0.0114	0.0005	0.42
37	95.609	3.339	1.052	3.139	280.2	0.62	0.983	0.0167	0.0004	0.86
38	97.243	2.097	0.660	3.481	280.2	0.49	0.9848	0.015	0.0002	0.788
39	97.464	0.572	1.965	5.767	282.2	0.114	0.9919	0.0065	0.0016	0.276
40	97.464	0.572	1.965	7.19	284.2	0.115	0.9921	0.0067	0.0012	0.107

Table A.1.10: Phase compositions predicted by PVTsim based on experimental dissociation conditions and total system composition listed in the study by Belandria et al. (2011) [48]

#	PR Peneloux					SRK Peneloux				
	y(CO <sub>2</sub> )	Aqueous phase			z(CO <sub>2</sub> )	y(CO <sub>2</sub> )	Aqueous phase			z(CO <sub>2</sub> )
		H <sub>2</sub> O	CO <sub>2</sub>	CH <sub>4</sub>			H <sub>2</sub> O	CO <sub>2</sub>	CH <sub>4</sub>	
1	0.175	0.9954	0.004	0.0007	0.322	0.133	0.9964	0.0029	0.0007	0.321
2	0.101	0.9968	0.0024	0.0008	0.204	0.092	0.9971	0.0022	0.0008	0.264
3	0.092	0.9969	0.0022	0.0008	0.188	0.087	0.9972	0.0021	0.0008	0.257
4	0.392	0.992	0.0076	0.0004	0.581	-	0.9935	0.0061	0.0004	0.501
5	0.329	0.9929	0.0066	0.0005	0.516	-	0.9943	0.0052	0.0005	0.457
6	0.267	0.9938	0.0056	0.0006	0.444	-	0.9948	0.0047	0.0005	0.426
7	0.683	0.9886	0.0112	0.0002	0.815	0.706	0.9885	0.0113	0.0002	0.836
8	0.584	0.9896	0.0101	0.0003	0.745	-	0.9893	0.0105	0.0002	0.715
9	0.193	0.9946	0.0047	0.0007	0.342	0.147	0.9958	0.0035	0.0008	0.331
10	0.143	0.9956	0.0036	0.0008	0.269	0.118	0.9963	0.0029	0.0008	0.296
11	0.123	0.996	0.0032	0.0009	-	0.107	0.9965	0.0027	0.0008	0.281
12	0.433	0.9905	0.009	0.0004	0.612	0.345	0.9926	0.007	0.0005	0.501
13	0.373	0.9915	0.008	0.0005	0.554	0.284	0.9935	0.0059	0.0006	0.455
14	0.276	0.9931	0.0063	0.0006	0.448	-	0.9943	0.0051	0.0006	0.417
15	0.699	0.987	0.0128	0.0002	0.82	0.731	0.9868	0.013	0.0002	0.848
16	0.631	0.9879	0.0119	0.0003	0.773	0.665	0.9876	0.0122	0.0002	0.803
17	0.199	0.9942	0.005	0.0008	-	0.155	0.9954	0.0038	0.0008	0.335
18	0.125	0.9957	0.0034	0.0009	0.237	0.110	0.9962	0.0029	0.0009	0.281
19	0.120	0.9959	0.0032	0.0009	-	0.110	0.9963	0.0029	0.0009	0.281
20	0.447	0.9898	0.0098	0.0005	0.62	0.366	0.9918	0.0077	0.0005	0.511
21	0.341	0.9915	0.0079	0.0006	0.517	-	0.9932	0.0062	0.0006	0.447
22	0.252	0.9931	0.0062	0.0007	0.415	-	0.994	0.0054	0.0007	0.411
23	0.699	0.9862	0.0136	0.0002	0.817	0.735	0.9858	0.014	0.0002	-
24	-	0.9882	0.0115	0.0004	0.708	-	0.9871	0.0126	0.0003	0.701
25	0.197	0.9936	0.0055	0.0009	-	0.170	0.9945	0.0046	0.0009	0.343
26	0.141	0.9949	0.0041	0.001	-	0.127	0.9954	0.0036	0.001	0.296
27	0.099	0.9959	0.003	0.0011	0.189	0.101	0.996	0.003	0.0011	0.261
28	0.368	0.9899	0.0094	0.0006	-	0.294	0.992	0.0073	0.0007	0.448
29	0.252	0.9923	0.0069	0.0008	0.406	-	0.9933	0.006	0.0008	0.398
30	0.730	0.9836	0.0161	0.0002	-	0.731	0.9841	0.0157	0.0002	-
31	0.642	0.985	0.0147	0.0003	0.767	0.653	0.9851	0.0146	0.0003	-
32	0.197	0.9936	0.0055	0.0009	-	0.197	0.9937	0.0054	0.0009	-
33	0.136	0.9945	0.0044	0.0012	-	0.137	0.9946	0.0043	0.0011	-
34	0.108	0.9952	0.0036	0.0012	-	0.109	0.9953	0.0035	0.0012	-
35	0.361	0.9895	0.0098	0.0007	-	0.364	0.9896	0.0097	0.0007	-
36	0.269	0.991	0.0081	0.0009	0.414	-	0.9925	0.0066	0.0009	0.383
37	0.636	0.9836	0.0161	0.0004	-	0.640	0.9839	0.0158	0.0004	-
38	0.528	0.98513	0.01435	0.00053	-	0.534	0.9853	0.0142	0.0005	-
39	0.103	0.9949	0.0037	0.0014	-	0.104	0.9949	0.0037	0.0014	-
40	0.098	0.9945	0.0038	0.0016	-	0.099	0.9946	0.0038	0.0016	-

Table A.1.11: Calculated relative deviations and absolute relative deviations from listed experimental compositions in Belandria et al. (2011) [48] in regards to predicted compositions from PVTsim utilizing PR.

#	Relative deviation (%)					Absolute relative deviation (%)				
	Aqueous phase					Aqueous phase				
	yCO2	H2O	CO2	CH4	zCO2	yCO2	H2O	CO2	CH4	zCO2
1	-24.1	-	-	-	-	24.1	-	-	-	-
2	19.2	-	-	-	-	19.2	-	-	-	-
3	-13.6	-0.3	60.0	-33.3	-95.8	13.6	0.3	60.0	33.3	95.8
4	-13.6	-0.2	23.2	-33.3	-5.8	13.6	0.2	23.2	33.3	5.8
5	-14.2	0.0	-6.5	16.7	-31.6	14.2	0.0	6.5	16.7	31.6
6	-21.4	-0.4	41.1	-100.0	-51.0	21.4	0.4	41.1	100.0	51.0
7	-8.4	-0.1	11.8	-100.0	7.8	8.4	0.1	11.8	100.0	7.8
8	-7.2	-0.3	21.1	-200.0	7.0	7.2	0.3	21.1	200.0	7.0
9	-16.3	-0.3	33.8	12.5	-1.2	16.3	0.3	33.8	12.5	1.2
10	-10.9	-	-	-	-	10.9	-	-	-	-
11	-43.0	0.0	-6.7	0.0	-	43.0	0.0	6.7	0.0	-
12	-12.8	-0.2	16.7	-33.3	5.8	12.8	0.2	16.7	33.3	5.8
13	-23.5	0.0	-6.7	16.7	5.5	23.5	0.0	6.7	16.7	5.5
14	-21.1	-0.4	41.7	-100.0	-22.4	21.1	0.4	41.7	100.0	22.4
15	-6.4	0.1	-4.1	0.0	1.3	6.4	0.1	4.1	0.0	1.3
16	-11.7	0.1	-5.3	0.0	-2.8	11.7	0.1	5.3	0.0	2.8
17	-11.2	-0.1	19.4	-14.3	-	11.2	0.1	19.4	14.3	-
18	6.7	0.0	0.0	0.0	0.8	6.7	0.0	0.0	0.0	0.8
19	-25.0	-0.3	48.4	-28.6	-	25.0	0.3	48.4	28.6	-
20	-10.4	-0.2	13.3	-25.0	3.7	10.4	0.2	13.3	25.0	3.7
21	-8.3	-0.3	30.1	-50.0	-29.3	8.3	0.3	30.1	50.0	29.3
22	-8.6	-0.5	45.1	-75.0	-33.0	8.6	0.5	45.1	75.0	33.0
23	-4.5	-0.2	13.9	0.0	6.8	4.5	0.2	13.9	0.0	6.8
24	-	0.0	-0.9	0.0	9.7	-	0.0	0.9	0.0	9.7
25	2.5	-0.5	37.5	57.1	-	2.5	0.5	37.5	57.1	-
26	-1.4	-0.3	44.6	-11.1	-	1.4	0.3	44.6	11.1	-
27	3.9	-0.4	55.9	-37.5	-27.7	3.9	0.4	55.9	37.5	27.7
28	-13.9	-0.3	24.2	-50.0	-	13.9	0.3	24.2	50.0	-
29	-8.2	-0.5	45.2	-100.0	-48.7	8.2	0.5	45.2	100.0	48.7
30	-5.2	-	-	-	-	5.2	-	-	-	-
31	-5.4	0.1	-7.3	25.0	2.4	5.4	0.1	7.3	25.0	2.4
32	2.5	-0.2	22.5	0.0	-	2.5	0.2	22.5	0.0	-
33	7.5	-0.5	-91.3	84.8	-	7.5	0.5	91.3	84.8	-
34	0.0	-0.4	-176.9	82.9	-	0.0	0.4	176.9	82.9	-
35	-4.9	-0.5	32.9	-40.0	-	4.9	0.5	32.9	40.0	-
36	-14.5	-0.3	28.9	-80.0	1.4	14.5	0.3	28.9	80.0	1.4
37	-2.6	-0.1	3.6	0.0	-	2.6	0.1	3.6	0.0	-
38	-7.8	0.0	4.3	-165.0	-	7.8	0.0	4.3	165.0	-
39	9.6	-0.3	43.1	12.5	-	9.6	0.3	43.1	12.5	-
40	14.8	-0.2	43.3	-33.3	-	14.8	0.2	43.3	33.3	-
<b><math>\bar{x}</math>:</b>	<b>-8.0</b>	<b>-0.2</b>	<b>13.9</b>	<b>-27.8</b>	<b>-13.5</b>	<b>11.4</b>	<b>0.2</b>	<b>30.9</b>	<b>44.9</b>	<b>18.2</b>

Table A.1.12: Calculated relative deviations and absolute relative deviations from listed experimental compositions in Belandria et al. (2011) [48] in regards to predicted compositions from PVTsim utilizing SRK.

#	Relative deviation (%)					Absolute relative deviation (%)					
	Aqueous phase					Aqueous phase					Structure
	yCO2	H2O	CO2	CH4	zCO2	yCO2	H2O	CO2	CH4	zCO2	
1	5.7	-	-	-	-	5.7	-	-	-	-	-
2	26.4	-	-	-	-	26.4	-	-	-	-	-
3	-7.4	-0.3	61.8	-33.3	-167.7	7.4	0.3	61.8	33.3	167.7	sII
4	-	-0.4	38.4	-33.3	8.7	-	0.4	38.4	33.3	8.7	sII
5	-	-0.1	16.1	16.7	-16.6	-	0.1	16.1	16.7	16.6	sII
6	-	-0.5	50.5	-66.7	-44.9	-	0.5	50.5	66.7	44.9	sII
7	-12.1	-0.1	11.0	-100.0	5.4	12.1	0.1	11.0	100.0	5.4	sI
8	-	-0.2	18.0	-100.0	10.7	-	0.2	18.0	100.0	10.7	sII
9	11.4	-0.4	50.7	0.0	2.1	11.4	0.4	50.7	0.0	2.1	sII
10	8.5	-	-	-	-	8.5	-	-	-	-	-
11	-24.4	0.0	10.0	11.1	-57.0	24.4	0.0	10.0	11.1	57.0	sII
12	10.2	-0.4	35.2	-66.7	22.9	10.2	0.4	35.2	66.7	22.9	sII
13	6.0	-0.2	21.3	0.0	22.4	6.0	0.2	21.3	0.0	22.4	sII
14	-	-0.5	52.8	-100.0	-13.9	-	0.5	52.8	100.0	13.9	sII
15	-11.3	0.1	-5.7	0.0	-2.0	11.3	0.1	5.7	0.0	2.0	sI
16	-17.7	0.1	-8.0	33.3	-6.8	17.7	0.1	8.0	33.3	6.8	sI
17	13.4	-0.2	38.7	-14.3	-26.9	13.4	0.2	38.7	14.3	26.9	sII
18	17.9	-0.1	14.7	0.0	-17.6	17.9	0.1	14.7	0.0	17.6	sII
19	-14.6	-0.3	53.2	-28.6	-18.1	14.6	0.3	53.2	28.6	18.1	sII
20	9.6	-0.4	31.9	-25.0	20.7	9.6	0.4	31.9	25.0	20.7	sII
21	-	-0.5	45.1	-50.0	-11.8	-	0.5	45.1	50.0	11.8	sII
22	-	-0.6	52.2	-75.0	-31.7	-	0.6	52.2	75.0	31.7	sII
23	-9.9	-0.2	11.4	0.0	-	9.9	0.2	11.4	0.0	-	-
24	-	0.1	-10.5	25.0	10.6	-	0.1	10.5	25.0	10.6	sII
25	15.8	-0.6	47.7	57.1	-47.2	15.8	0.6	47.7	57.1	47.2	sII
26	8.6	-0.4	51.4	-11.1	-31.6	8.6	0.4	51.4	11.1	31.6	sII
27	1.9	-0.4	55.9	-37.5	-76.4	1.9	0.4	55.9	37.5	76.4	sII
28	9.0	-0.5	41.1	-75.0	2.0	9.0	0.5	41.1	75.0	2.0	sII
29	-	-0.6	52.4	-100.0	-45.8	-	0.6	52.4	100.0	45.8	sII
30	-5.3	-	-	-	-	5.3	-	-	-	-	-
31	-7.2	0.1	-6.6	25.0	-	7.2	0.1	6.6	25.0	-	-
32	2.5	-0.2	23.9	0.0	-	2.5	0.2	23.9	0.0	-	-
33	6.8	-0.5	-87.0	86.1	-	6.8	0.5	87.0	86.1	-	-
34	-0.9	-0.4	-169.2	82.9	-	0.9	0.4	169.2	82.9	-	-
35	-5.8	-0.5	33.6	-40.0	-	5.8	0.5	33.6	40.0	-	-
36	-	-0.4	42.1	-80.0	8.8	-	0.4	42.1	80.0	8.8	sII
37	-3.2	-0.1	5.4	0.0	-	3.2	0.1	5.4	0.0	-	-
38	-9.0	-0.1	5.3	-150.0	-	9.0	0.1	5.3	150.0	-	-
39	8.8	-0.3	43.1	12.5	-	8.8	0.3	43.1	12.5	-	-
40	13.9	-0.3	43.3	-33.3	-	13.9	0.3	43.3	33.3	-	-
<b><math>\bar{x}</math>:</b>	<b>1.6</b>	<b>-0.3</b>	<b>21.4</b>	<b>-24.2</b>	<b>-19.3</b>	<b>10.2</b>	<b>0.3</b>	<b>37.4</b>	<b>43.6</b>	<b>28.1</b>	

## Appendix A.2: Accuracy of PVTsim predictions

Table A.2.1: Predicted dissociation conditions from PVTsim based on experimental data from Belandria et al. (2010) [47]. PR EOS utilized.

Mole% in feed			$T_{\text{exp}}$ (K)	$P_{\text{exp}}$ (MPa)	$T_{\text{pred}}$ (K)	$P_{\text{pred}}$ (MPa)	D T	RD% P	AD T	ARD% P
H <sub>2</sub> O	CO <sub>2</sub>	CH <sub>4</sub>								
69.995	7.921	22.084	284.2	5.29	282.35	6.56	1.8	-24.01	1.8	24.01
53.019	12.403	34.578	287.2	9.83	287.43	9.53	-0.2	3.05	0.2	3.05
48.43	13.615	37.956	289.2	11.62	288.64	12.6	0.6	-8.43	0.6	8.43
77.903	6.01	16.087	279.1	3.6	278.87	3.69	0.2	-2.50	0.2	2.5
66.008	16.656	17.336	284.8	5.82	284.1	6.39	0.7	-9.79	0.7	9.79
42.036	28.402	29.562	289.9	12.41	289.06	14.44	0.8	-16.36	0.8	16.36
65.63	17.185	17.185	284.9	5.88	284.21	6.46	0.7	-9.86	0.7	9.86
80.909	9.622	9.469	279.1	2.96	278.49	3.17	0.6	-7.09	0.6	7.09
79.056	15.289	5.655	280.6	3.16	280.07	3.38	0.5	-6.96	0.5	6.96
73.715	19.188	7.097	281.9	4.02	281.97	3.98	-0.1	1.00	0.1	1
31.258	50.182	18.56	289.1	13.06	288.66	14.54	0.4	-11.33	0.4	11.33
$\bar{x}$ :							<b>0.6</b>	<b>-8.39</b>	<b>0.6</b>	<b>9.13</b>

Table A.2.2: Predicted dissociation conditions from PVTsim based on experimental data from Belatrán and Servio (2008) [45]. PR EOS utilized.

Mole% in feed			$T_{\text{exp}}$ (K)	$P_{\text{exp}}$ (MPa)	$T_{\text{pred}}$ (K)	$P_{\text{pred}}$ (MPa)	D T	RD% P	AD T	ARD% P
H <sub>2</sub> O	CO <sub>2</sub>	CH <sub>4</sub>								
92.574	1.485	5.941	275.14	2.36	274.01	2.65	1.13	-12.29	1.13	12.29
93.817	3.092	3.092	275.24	1.92	274.24	2.15	1	-11.98	1.00	11.98
92.683	3.659	3.659	277.01	2.28	275.87	2.59	1.14	-13.60	1.14	13.60
90.045	1.991	7.964	277.43	3.20	277.05	3.33	0.38	-4.06	0.38	4.06
91.071	4.464	4.464	278.96	2.79	277.75	3.20	1.21	-14.70	1.21	14.70
87.910	2.418	9.672	279.48	3.93	279.06	4.11	0.42	-4.58	0.42	4.58
86.560	2.688	10.752	281.12	4.41	280.16	4.89	0.96	-10.88	0.96	10.88
87.994	6.003	6.003	281.20	3.75	280.42	4.11	0.78	-9.60	0.78	9.60
85.537	7.232	7.232	282.97	4.52	282.02	5.08	0.95	-12.39	0.95	12.39
81.608	3.678	14.714	283.38	6.16	283.26	6.24	0.12	-1.30	0.12	1.30
80.484	9.758	9.758	284.73	5.63	283.82	6.35	0.91	-12.79	0.91	12.79
78.156	4.369	17.475	285.34	7.47	284.95	7.83	0.39	-4.82	0.39	4.82
$\bar{x}$ :							<b>0.78</b>	<b>-9.42</b>	<b>0.78</b>	<b>9.42</b>

Table A.2.3: Predicted dissociation conditions from PVTsim based on experimental data from Adisasmito et al. (1991) [38]. PR EOS utilized.

Mole% in feed			$T_{\text{exp}}$ (K)	$P_{\text{exp}}$ (MPa)	$T_{\text{pred}}$ (K)	$P_{\text{pred}}$ (MPa)	D T	RD% P	AD T	ARD% P
H <sub>2</sub> O	CO <sub>2</sub>	CH <sub>4</sub>								
95.879	0.412	3.709	273.7	2.52	273.61	2.54	0.1	-0.79	0.1	0.79
94.949	0.455	4.597	275.8	3.10	275.66	3.140	0.1	-1.29	0.1	1.29
93.778	0.498	5.724	277.8	3.83	277.73	3.86	0.1	-0.78	0.1	0.78
92.046	0.636	7.317	280.2	4.91	280.21	4.9	0.0	0.20	0.0	0.20
89.047	0.876	10.077	283.2	6.80	283.34	6.7	-0.1	1.47	0.1	1.47
86.579	1.074	12.347	285.1	8.40	285.27	8.24	-0.2	1.90	0.2	1.90
83.098	1.521	15.380	287.2	10.76	287.45	10.44	-0.3	2.97	0.3	2.97
95.764	0.593	3.643	274.6	2.59	274.22	2.69	0.4	-3.86	0.4	3.86
94.719	0.686	4.594	276.9	3.24	276.42	3.4	0.5	-4.94	0.5	4.94
93.189	0.885	5.926	279.1	4.18	278.98	4.23	0.1	-1.20	0.1	1.20
91.249	1.138	7.613	281.6	5.38	281.45	5.47	0.2	-1.67	0.2	1.67
88.364	1.513	10.123	284.0	7.17	284.13	7.06	-0.1	1.53	0.1	1.53
84.914	1.810	13.276	283.1	9.24	286.31	6.41	-3.2	30.63	3.2	30.63
82.626	2.259	15.115	287.4	10.95	287.71	10.54	-0.3	3.74	0.3	3.74
96.515	0.871	2.614	273.8	2.12	273.01	2.3	0.8	-8.49	0.8	8.49
93.493	1.431	5.075	279.4	3.96	279.07	4.1	0.3	-3.54	0.3	3.54
89.704	2.265	8.031	283.4	6.23	283.35	6.27	0.0	-0.64	0.0	0.64
87.212	2.686	10.103	285.2	7.75	285.22	7.73	0.0	0.26	0.0	0.26
82.671	4.332	12.996	287.6	10.44	287.77	10.2	-0.2	2.30	0.2	2.30
96.997	1.321	1.682	273.7	1.81	272.78	2	0.9	-10.50	0.9	10.50
95.618	1.841	2.542	276.9	2.63	276.35	2.8	0.5	-6.46	0.5	6.46
93.209	2.717	4.075	280.7	4.03	280.31	4.21	0.4	-4.47	0.4	4.47
90.714	3.621	5.664	283.1	5.43	282.95	5.53	0.2	-1.84	0.2	1.84
87.931	4.707	7.362	285.1	6.94	285.01	7.02	0.1	-1.15	0.1	1.15
82.616	6.780	10.605	287.4	9.78	287.58	9.53	-0.2	2.56	0.2	2.56
96.692	1.654	1.654	275.6	1.99	274.13	2.35	1.5	-18.09	1.5	18.09
94.993	2.353	2.654	278.5	2.98	277.86	3.2	0.6	-7.38	0.6	7.38
93.013	2.795	4.192	280.9	4.14	280.56	4.3	0.3	-3.86	0.3	3.86
92.420	3.108	4.472	281.8	4.47	281.32	4.73	0.5	-5.82	0.5	5.82
87.886	5.330	6.784	285.1	6.84	285.05	6.89	0.1	-0.73	0.1	0.73
82.334	7.950	9.716	287.4	9.59	287.52	9.42	-0.1	1.77	0.1	1.77
97.195	2.048	0.757	274.6	1.66	273.90	1.800	0.7	-8.43	0.7	8.43
96.462	2.477	1.061	276.4	2.08	275.83	2.22	0.6	-6.73	0.6	6.73
95.569	3.013	1.418	278.2	2.58	277.71	2.73	0.5	-5.81	0.5	5.81
94.252	3.909	1.839	280.2	3.28	279.86	3.42	0.3	-4.27	0.3	4.27
92.594	4.962	2.444	282.0	4.12	281.75	4.25	0.3	-3.16	0.3	3.16
97.548	1.937	0.515	273.7	1.45	273.04	1.57	0.7	-8.28	0.7	8.28
96.790	2.504	0.706	275.9	1.88	275.40	2	0.5	-6.38	0.5	6.38
95.905	3.112	0.983	277.8	2.37	277.39	2.49	0.4	-5.06	0.4	5.06
94.770	3.922	1.307	279.6	2.97	279.33	3.07	0.3	-3.37	0.3	3.37
93.129	5.084	1.786	281.6	3.79	281.34	3.92	0.3	-3.43	0.3	3.43
91.432	7.283	1.285	282.7	4.37	282.00	4.33	0.7	0.92	0.7	0.92
$\bar{x}$ :							<b>0.2</b>	<b>-2.19</b>	<b>0.4</b>	<b>4.59</b>

Table A.2.4: Predicted dissociation conditions from PVTsim based on experimental data from Fan and Guo (1999). PR EOS utilized.

Mole% in feed			$T_{exp}$ (K)	$P_{exp}$ (MPa)	$T_{pred}$ (K)	$P_{pred}$ (MPa)	D T	RD% P	AD T	ARD% P
H <sub>2</sub> O	CO <sub>2</sub>	CH <sub>4</sub>								
97.243	2.661	0.096	273.5	1.1	272.10	1.30	1.40	-18.18	1.4	18.18
97.085	2.814	0.101	273.6	1.2	272.56	1.31	1.04	-12.93	1.0	12.93
96.979	2.916	0.105	273.7	1.2	272.86	1.33	0.84	-10.83	0.8	10.83
94.964	4.861	0.175	277.2	2.0	277.00	2.00	0.20	-2.56	0.2	2.56
95.002	4.824	0.174	277.6	1.9	276.95	2.10	0.65	-8.25	0.7	8.25
94.693	5.123	0.185	277.9	2.1	277.41	2.18	0.49	-6.34	0.5	6.34
91.844	7.872	0.284	280.4	3.0	280.40	3.00	0.00	0.00	0.0	0.00
89.329	10.299	0.371	281.7	3.7	281.94	3.60	-0.24	3.49	0.2	3.49
76.217	22.956	0.828	282.3	4.8	283.50	3.93	-1.20	18.13	1.2	18.13*
$\bar{x}$ :							<b>0.4</b>	<b>-4.2</b>	<b>0.7</b>	<b>8.97</b>

\* PVTsim determined hydrate former to be in liquid phase.

Table A.2.5: Predicted dissociation conditions from PVTsim based on experimental data from Seo et al. (2001) [43]. PR EOS utilized.

Mole% in feed			$T_{exp}$ (K)	$P_{exp}$ (MPa)	$T_{pred}$ (K)	$P_{pred}$ (MPa)	D T	RD% P	AD T	ARD% P
H <sub>2</sub> O	CO <sub>2</sub>	CH <sub>4</sub>								
88.639	6.817	4.545	273.56	1.5	272.88	1.62	0.68	-8.0	0.68	8.0
85.532	2.894	11.574	273.56	2.0	272.58	2.21	0.98	-10.6	0.98	10.6
85.199	8.880	5.920	275.86	2.0	275.51	2.08	0.35	-4.0	0.35	4.0
81.802	3.640	14.558	275.36	2.6	275.18	2.65	0.18	-1.9	0.18	1.9
81.235	11.259	7.506	277.96	2.6	277.86	2.63	0.1	-1.2	0.10	1.2
76.670	4.666	18.664	278.06	3.5	278.08	3.50	-0.02	0.0	0.02	0.0
75.554	14.667	9.778	280.16	3.5	280.41	3.95	-0.25	-12.9	0.25	12.9
69.100	6.180	24.720	281.46	5.0	281.46	5.00	0	0.0	0.00	0.00
$\bar{x}$ :							<b>0.25</b>	<b>-4.8</b>	<b>0.32</b>	<b>4.8</b>

Table A.2.6: Predicted dissociation conditions from PVTsim based on experimental data from Dholabhai et al. (1994) [39]. PR Peneloux utilized.

Mole% in feed			$T_{exp}$ (K)	$P_{exp}$ (MPa)	$T_{pred}$ (K)	$P_{pred}$ (MPa)	D T	RD% P	AD T	ARD% P
H <sub>2</sub> O	CO <sub>2</sub>	CH <sub>4</sub>								
95.600	0.880	3.520	277.56	3.41	277.35	3.49	0.21	-2.35	0.21	2.35
93.311	1.338	5.351	281.50	5.14	281.38	5.21	0.12	-1.36	0.12	1.36
96.965	0.607	2.428	274.10	2.36	273.59	2.49	0.51	-5.51	0.51	5.51
90.096	1.981	7.923	284.84	7.53	284.88	7.49	-0.04	0.53	0.04	0.53
$\bar{x}$ :							<b>0.20</b>	<b>-2.17</b>	<b>0.22</b>	<b>2.44</b>

Table A.2.7: Predicted dissociation conditions from PVTsim based on experimental data from Unruh and Katz (1949) [37]. PR Peneloux utilized.

Mole% in feed										
H <sub>2</sub> O	CO <sub>2</sub>	CH <sub>4</sub>	T <sub>exp</sub> (K)	P <sub>exp</sub> (MPa)	T <sub>pred</sub> (K)	P <sub>pred</sub> (MPa)	D T	RD% P	AD T	ARD% P
97.519	1.337	1.144	277.0	2.84	277.20	2.78	-0.2	2.11	0.2	2.11
97.894	1.135	0.971	278.9	3.46	278.72	3.53	0.2	-2.02	0.2	2.02
96.954	1.660	1.386	278.9	3.43	279.09	3.36	-0.2	2.04	0.2	2.04
97.349	1.445	1.206	280.9	4.24	280.75	4.31	0.1	-1.65	0.1	1.65
97.886	1.152	0.962	282.9	5.17	282.19	5.62	0.7	-8.70	0.7	8.70
98.199	0.981	0.819	284.7	6.47	283.92	7.12	0.8	-10.05	0.8	10.05
98.589	1.096	0.315	275.5	1.99	274.66	2.21	0.8	-11.06	0.8	11.06
99.219	0.607	0.174	279.2	3.08	277.13	3.90	2.1	-26.62	2.1	26.62
97.785	0.607	1.608	276.4	3.20	276.76	3.08	-0.4	3.75	0.4	3.75
98.529	0.403	1.068	278.4	3.95	278.47	3.92	-0.1	0.76	0.1	0.76
98.677	0.363	0.961	281.0	5.10	280.81	5.20	0.2	-1.96	0.2	1.96
98.769	0.337	0.894	283.8	6.89	283.54	7.09	0.3	-2.90	0.3	2.90
97.231	2.282	0.487	279.6	3.00	279.30	3.12	0.3	-4.00	0.3	4.00
98.134	1.538	0.328	282.2	4.27	281.49	4.68	0.7	-9.60	0.7	9.60
98.849	0.948	0.203	283.8	5.27	282.44	6.24	1.4	-18.41	1.4	18.41
98.888	0.916	0.196	285.5	6.89	284.56	7.76	0.9	-12.63	0.9	12.63*
98.833	0.961	0.205	285.7	7.00	284.74	7.91	1.0	-13.00	1.0	13.00*
$\bar{x}$ :							0.5	-6.70	0.6	7.72

\* PVTsim determined hydrate former to be in liquid phase.



## Appendix A.3: Unsuccessful hydrate experiments

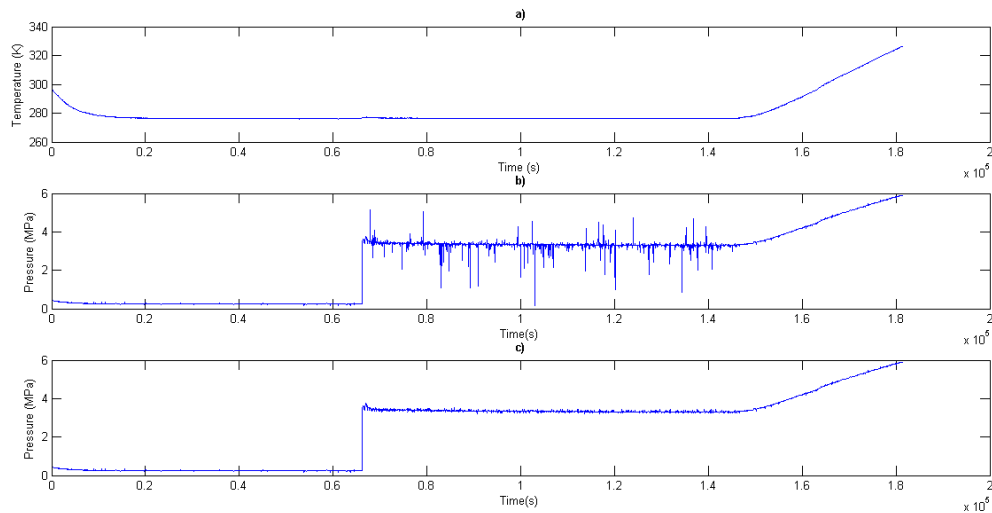


Figure A.1: Temperature and pressure time trace of experiment 1. The unusual pressure data is visible in b). The data has subsequently been removed in c).

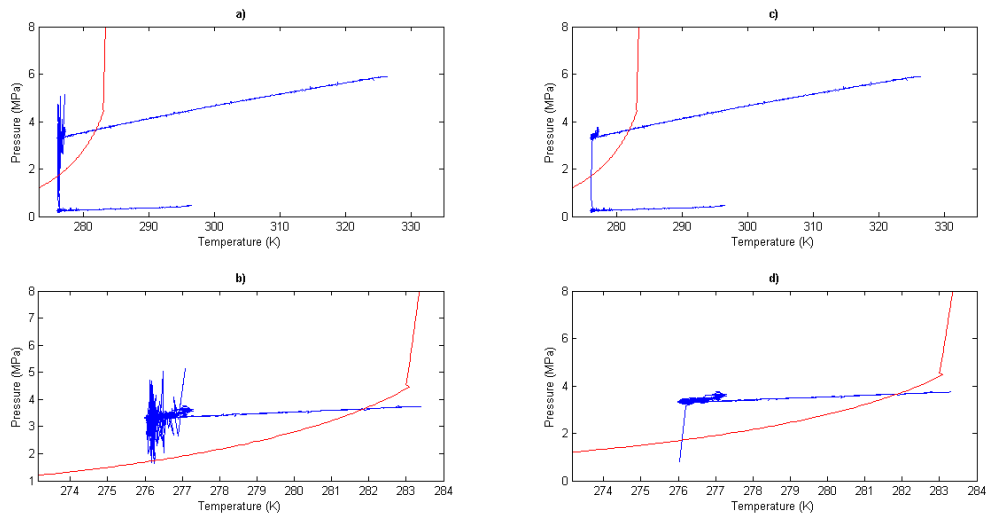


Figure A.2: PT trace of experiment 1 (blue) plotted with predicted PT curve by PVTsim (red). a) displays the entire experimental run, and c) displays the entire experimental run with the unusual pressure data removed. b) and d) presents the dissociation part of the experiment only, where b) is related to a), and d) to c).

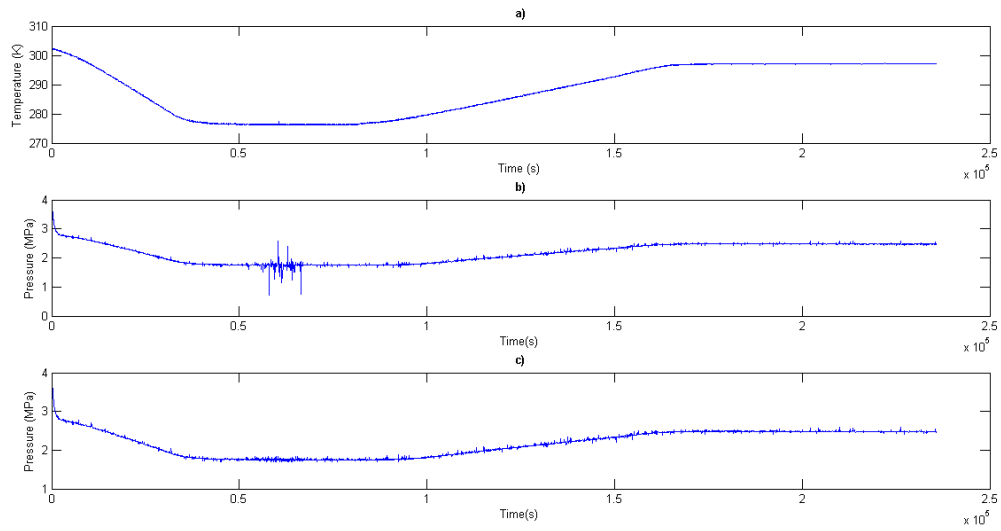


Figure A.3: Temperature and pressure time trace of experiment 3.

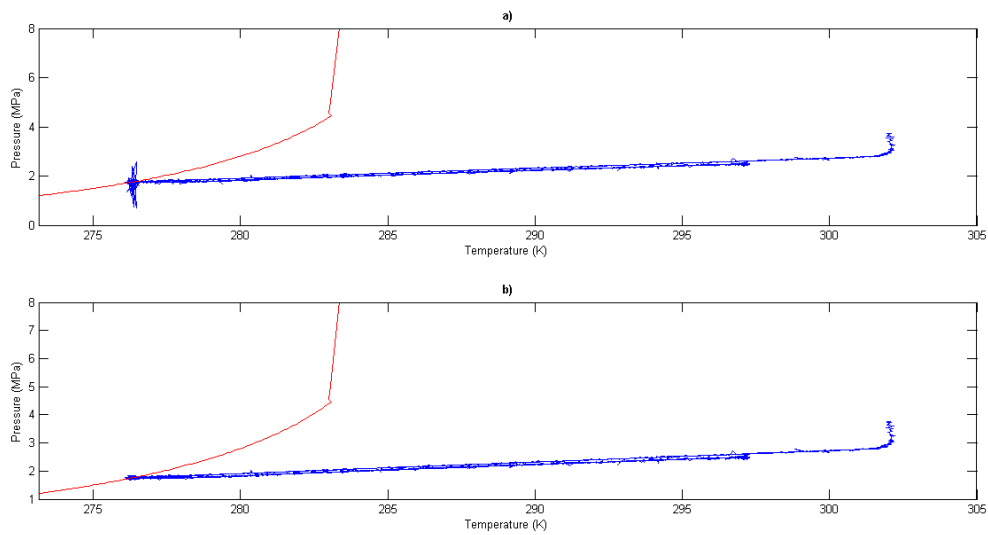


Figure A.4: PT trace of experiment 3 (blue) plotted with predicted PT curve by PVTsim (red).

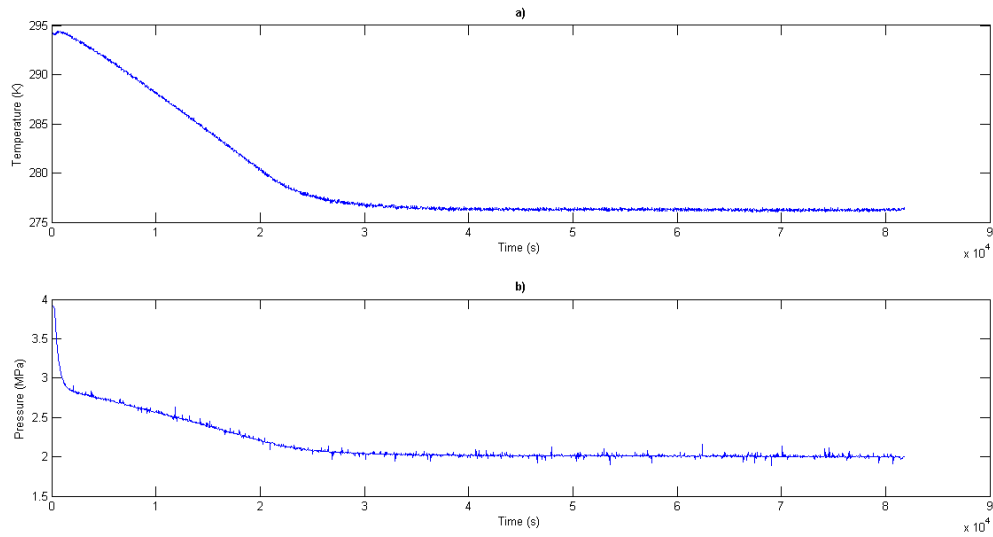


Figure A.5: Temperature and pressure time trace of experiment 4.

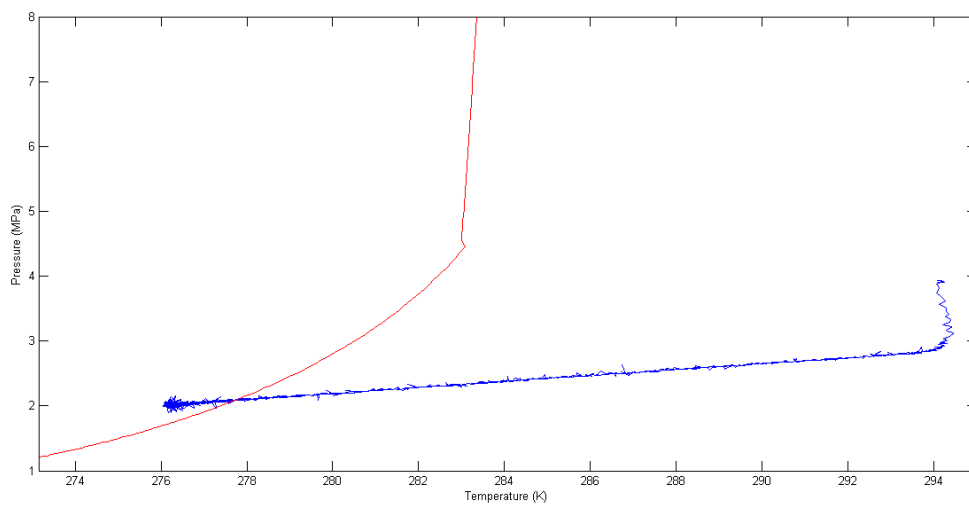


Figure A.6: PT trace of experiment 4 (blue) plotted with predicted PT curve by PVTsim (red).

## **APPENDIX B: EXPERIMENTAL PROCEDURES**

## B.1 The cooling incubator

A basic procedure for using the incubator is provided here. Additional information can be found in the manual [63].

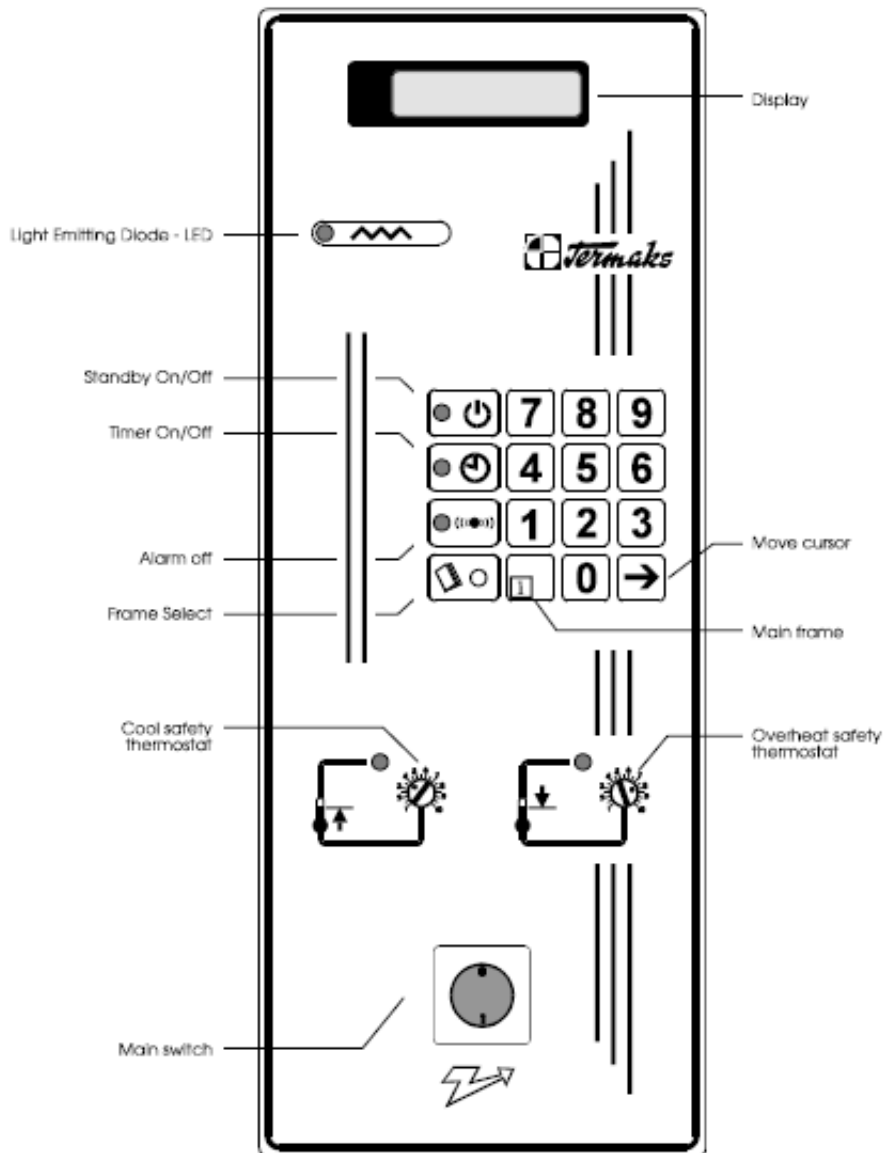


Figure B.1: The front panel of the incubator cabinet. From [63].

### B.1.1 Basic operations

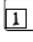



Turn on the main switch (green) to turn the power on. The LCD display on the front of the controller should start up. If an error message appears press the  button to access the main frame. The main frame displays the current temperature as TEMP and the input temperature as SET 1. Nine different frames can be viewed through the LCD display, where shuffling through the frames is possible by pressing the  button [63].



Figure B.2: The mainframe display. From [63].

If the incubator is not in use it is recommended to set it in standby mode rather than turn the main power switch off. By turning the main power switch off, the battery in the incubator will start to discharge. To set the incubator in standby mode press the  button. A light beside the standby button indicates standby mode. To restart the incubator press the same button. If the incubator will not be used for a significant time, the main power switch should be turned off [63].

### B.1.2 Cooling and heating

1. Push the  button once from the main frame and the second frame will appear [63]:

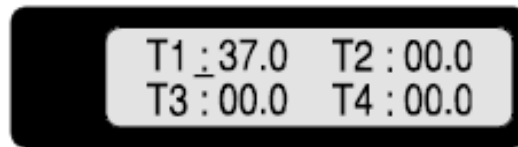


Figure B.3: Set temperature frame. From [63].

Move the underline marker with  $\rightarrow$ , and the temperature may be changed by pressing the numbers on the front panel [63].

Set T1: desired temperature, T2: 00.0, T3: 00.0 and T4: 00.0. After some seconds the display will change to the main frame and the incubator cabinet will reach this temperature in a number of hours [63].


2. The cooling/heating rate may be set by pressing  to reach frame 9, which is the ramping frame [63]:



Figure B.4: Set rate frame. From [63].

This may be adjusted by moving the underline marker with  $\rightarrow$ , and set the desired rate per minute with the keypad on the front panel. UP is for heating and DN is for cooling. A value of 006 means a rate of .1 °C per 6 minutes (or 1 °C per hour) [63].

If the main display shows TEMP and Set R, it means that the cooling/heating rate is controlled. By setting UP and DN to 000, the rate is not controlled and the incubator will reach the set temperature as fast as possible. The main display will consequently display TEMP and SET 1 [63].

## B.2 The stirring device.

This appendix is a basic operating procedure for the inverter and stirrer, where a more comprehensive explanation of the inverter may be found in the manual [88].

The inverter will be on as long as it is connected to a power source, as there is no OFF switch. Changes or inputs are done through the LED display on the inverter [88].

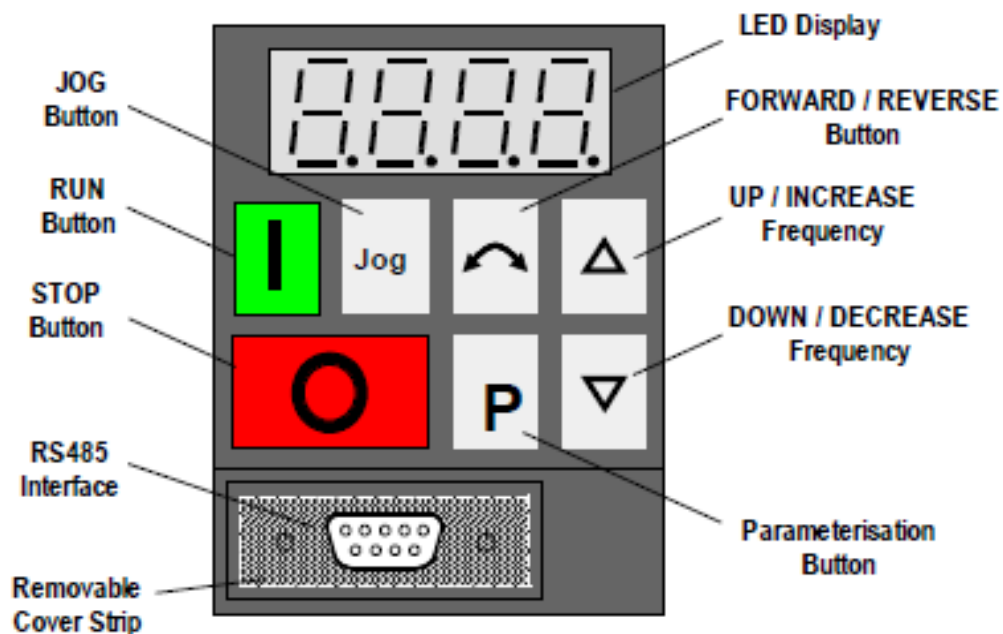


Figure B.5: Inverter display. The inverter in this experimental setup features a larger LED display and an additional MENU button not shown below. From [88].

Different functions are accessed through the LED display by pressing the MENU button. This displays a number of different submenus. Shuffle through the submenus by pressing the UP or DOWN button, and select a submenu by pressing the PARAMETERISATION button - P.

The relevant submenus for controlling and viewing the operating conditions are [88]:

1. Displays the current operating conditions while the motor is running.
2. Parameters.



Parameters may be viewed and edited through the keypad on the front panel. The parameters are numbered from P000 to P931. To edit a parameter select the Parameters submenu from the Menu by pressing P. Select the ALL submenu by pressing P, and shuffle through the parameters by pressing the UP or DOWN button. Select the parameter to be edited and press P to edit it. Editing the parameters is done by assigning different numbers to the selected parameter which is also done by pressing the UP (to increase the number) or DOWN (to decrease the number). Press P to store a value and MENU to return. The access to parameters is controlled by P009 (parameter protection settings). This should be set to P009 = 3 to allow the operator to read and edit all parameters, which it is currently set to. The electrical frequency parameter (to set the motor speed) is designated by P005 [88].

Table B.1: Overview of inverter functions and buttons. From [88].

RUN	Starts the inverter
STOP	Press once for cool down and stop, hold for immediate stop.
LED display	Displays frequency, parameter values or parameter numbers.
FORWARD/REVERSE	Pressing this changes the direction of the motor.
UP/INCREASE	For shuffling through parameters, and increase value.
DOWN/DECREASE	For shuffling through parameters, and decrease value.
PARAMETERISATION	To access or select parameters to be edited.
MENU	Displays the menu on the LED display.

## B.2.1 Troubleshooting

As with all electrical devices, always remove them from the power source before any alterations.

To detach the stirring shaft from the hydrate cell, use the customized wrench located in the lab. There are two sockets in the top cap of the hydrate cell that the wrench fits into. When mounting the stirring shaft back onto the hydrate cell apply vacuum grease to the grooves to avoid leakage.

The rotating plate under the motor is the part that experiences the most strain. It has been fitted with three screws to prevent it from grinding on the bottom of the motor. It is advisable to regularly check the screws and tighten them if they are loose to prevent any problems. To tighten the screws the motor has to be detached from the incubator cabinet. Loosen the bolts that hold the motor suspended on the platform with a hex key. Make sure that the belt transmission that connects the motor to the stirring shaft is correctly arranged during reassembling.

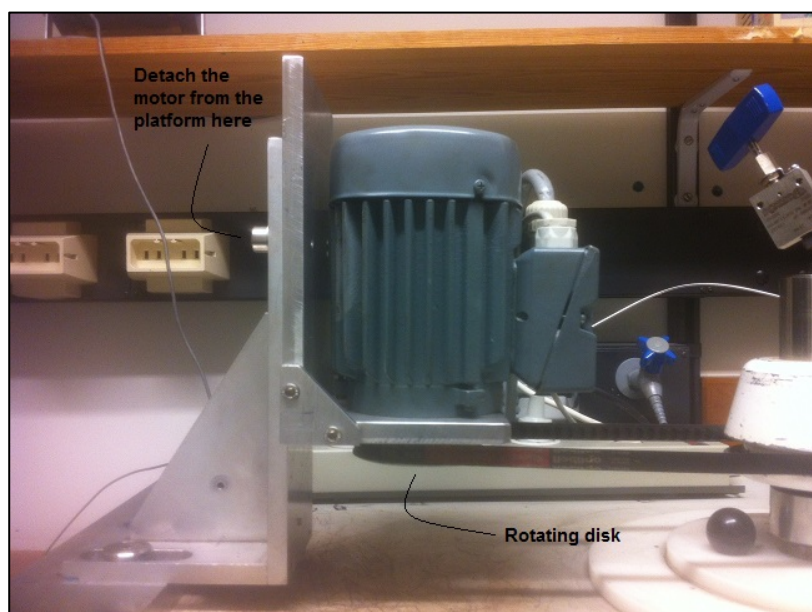


Figure B.6: The electric motor.

If the motor makes a very loud knocking sound when running, some of the bearings have probably been displaced. Detach the motor from the platform on the incubator cabinet, and detach the rotating plate. Sometimes the bearings fall back into place when tipping the motor to either side.

The motor has a tendency to get very hot when used for an extended time period. The temperature of the motor was measured with a thermometer, where a temperature of approximately 70 °C was measured. It is advisable to let it cool down whenever possible. If the inverter itself gets overheated it will shut down. When sampling or releasing explosive gas through valve 1, it is recommended to wait until the motor has cooled down sufficiently.

The motor is quite heavy so it is advisable to be two people when disassembling and reassembling the motor onto the cabinet. The same applies when disassembling the stirring device mounted to the top cap, to avoid any damage.

### B.3 LabVIEW VIs

A LabVIEW program is termed a VI, which is short for virtual instrument. A procedure for using the calibration VI and the logging VI for hydrate experiments is provided in the subsequent sections.

A LabVIEW VI consists of two parts. A front panel with “controls”, where controls may be knobs, buttons and graphs. The front panel is the user interface of the VI. The second part of a VI is the block diagram, which is the programming interface. It contains the programming elements, such as blocks, functions or subVIs. These elements are wired together and determine the execution order of the program [67-69].

Only the front panel is visible when opening a VI in LABVIEW. To view the block diagram, select “Window” from the toolbar menu, and select “Show block diagram”.

To run a VI in LABVIEW press the “Run arrow” in the toolbar. For both the calibration and the measurements VI, a stop button has been incorporated in the VI. Always use this stop button to stop a running VI. It is not recommended to use the “Abort execution” button from the main toolbar as this may cause a loss of data.

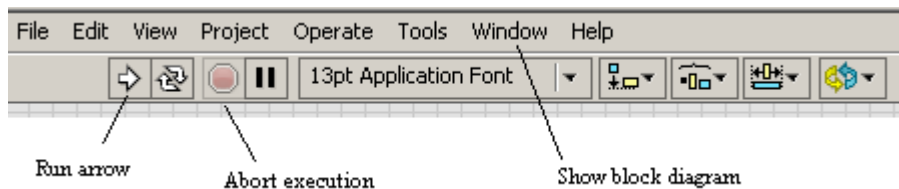


Figure B.7: The main toolbar in LabVIEW.

When a VI is running in LabVIEW the gridlines in the front panel disappears:

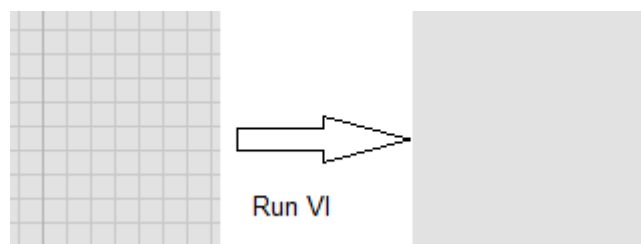


Figure B.8: Gridlines disappear in the front panel while a VI is running.

### B.3.1 The calibration VI

The simple VI programmed for calibration procedures is displayed below. The textboxes in the figures explain the calibration procedure. The directory for the calibration VI is:

D:\LABVIEW\Ole\calibration.vi

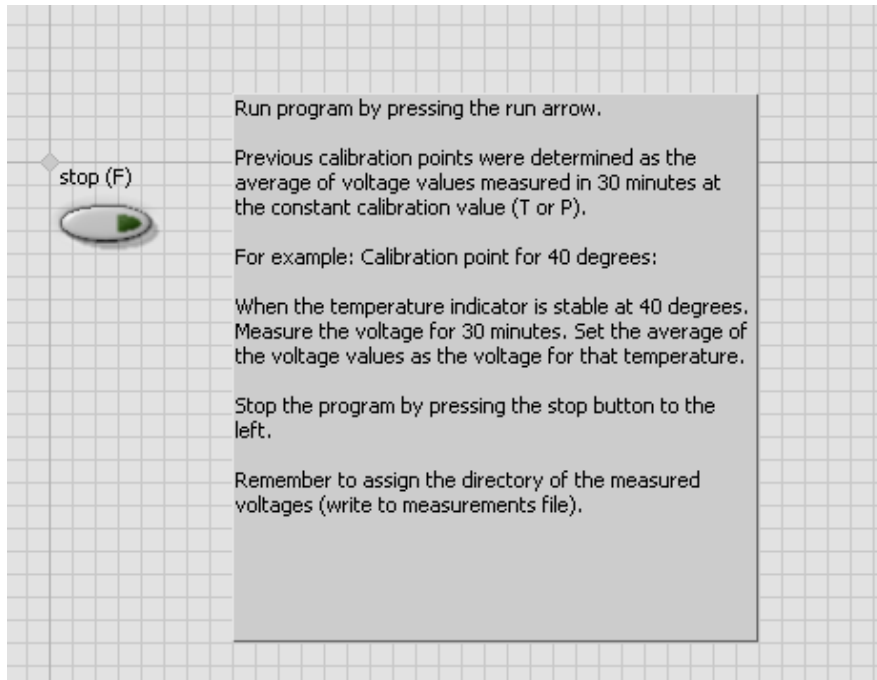
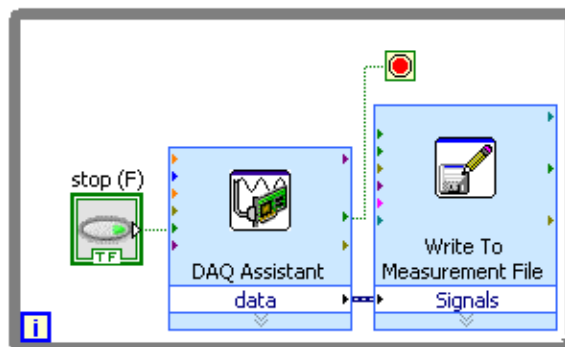


Figure B.9: Front panel of the calibration VI constructed.



The calibration VI is here programmed to acquire voltage values from channel ai0. This channel receives voltage values from the temperature sensor. The sampling is continuous, with a rate of 1 Hz.

To acquire voltages from the pressure sensor the channel has to be changed:

- 1) Open the DAQ Assistant and add a new channel (voltage signal).
- 2) The pressure sensor is connected to channel a1, select this channel.
- 3) Choose the same configuration for this channel as for the temperature channel (T).
- 4) Remove the temperature channel, so it only measures the voltages from the pressure sensor.

Figure B.10: Block diagram of the calibration VI constructed.

### B.3.1 The logging VI

The directory for the VI utilized to acquire data from hydrate experiments is:

D:\LABVIEW\Ole\MeasurementsOle.vi

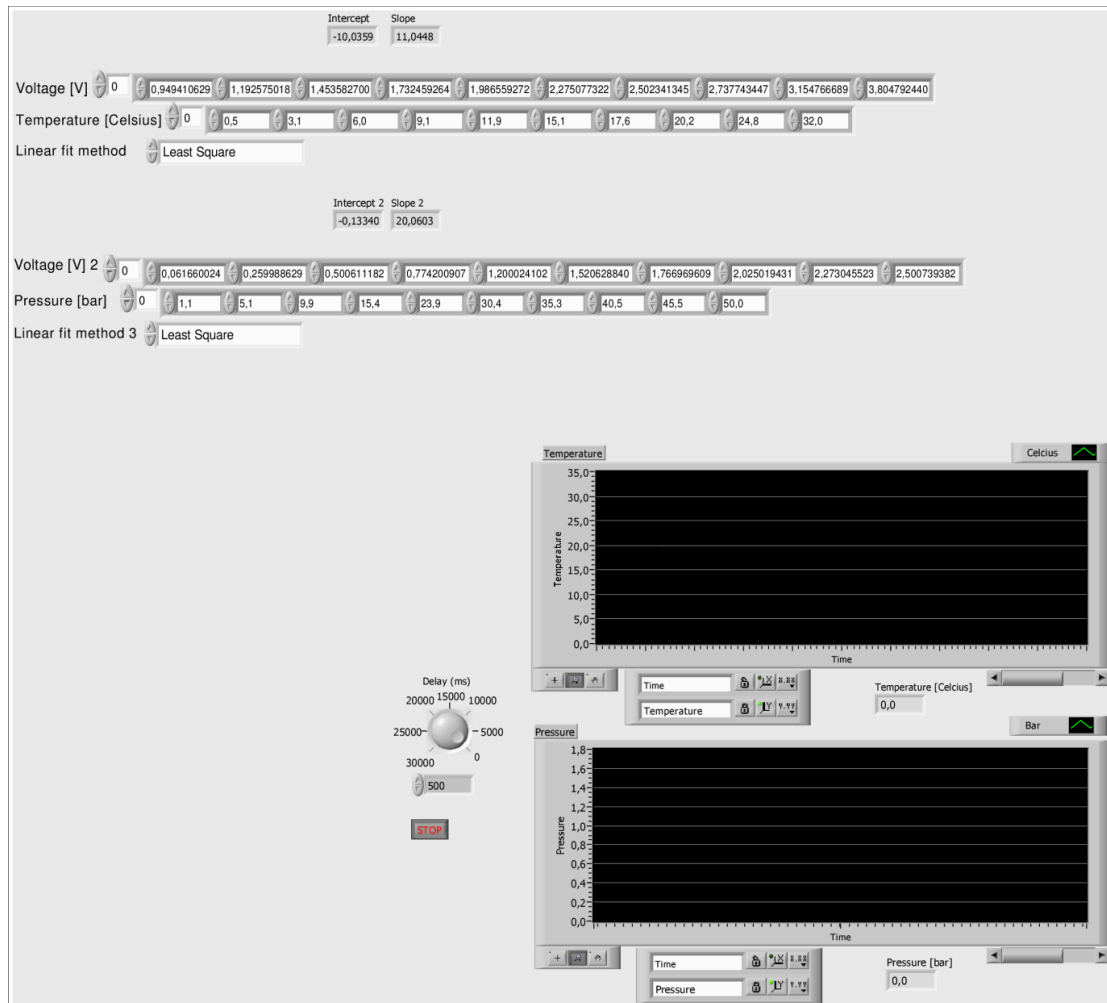


Figure B.11: Front panel of the logging program utilized to acquire data from hydrate experiments.

The front panel in the VI constructed in this thesis contains two graphs and two numeric indicators. The graphs display pressure and temperature changes as a function of time, i.e. as the experiment is running. The graphs are interactive as it is possible to zoom in or out of specific parts of the graph (graph palette). The numeric indicator displays the last logged data point (temperature or pressure).

When the graphs in the front panel display data it automatically zooms based on the last logged data. The “default full view” button in Fig.B.13 has to be clicked to view the entirety of the logged data.

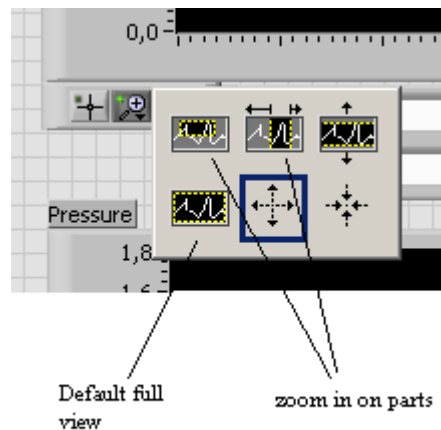


Figure B.12: The graph palette.

When starting a new experiment the graph should be cleared by right clicking the graph, data operations, and clear chart.

A set of numeric controls is visible at the top of the front panel. These are values that determine the calibration line and convert the voltage values from the sensors to actual temperature and pressure values. To add more calibration points to the program, the length of the row of the “numeric control” boxes may be increased. A new numeric indicator automatically appears, and a new calibration point may be added.

The delay knob in the front panel determines the sampling rate. The sampling rate can be adjusted during data acquisition. To adjust the sampling rate the user may turn the knob, or input a number in the numeric control below the knob. The input value is in milliseconds.

The block diagram for the datalogging VI is displayed in Fig.B.13. The save to measurements file in the block diagram defines where the data from the process is stored on the computer. The data is stored as an .lvm file, which can be converted to a .txt file by simply renaming the file. The .txt file may subsequently be read by programs such as Excel and MATLAB. The data is stored in three columns, time (seconds), temperature (°C) and pressure (bar).

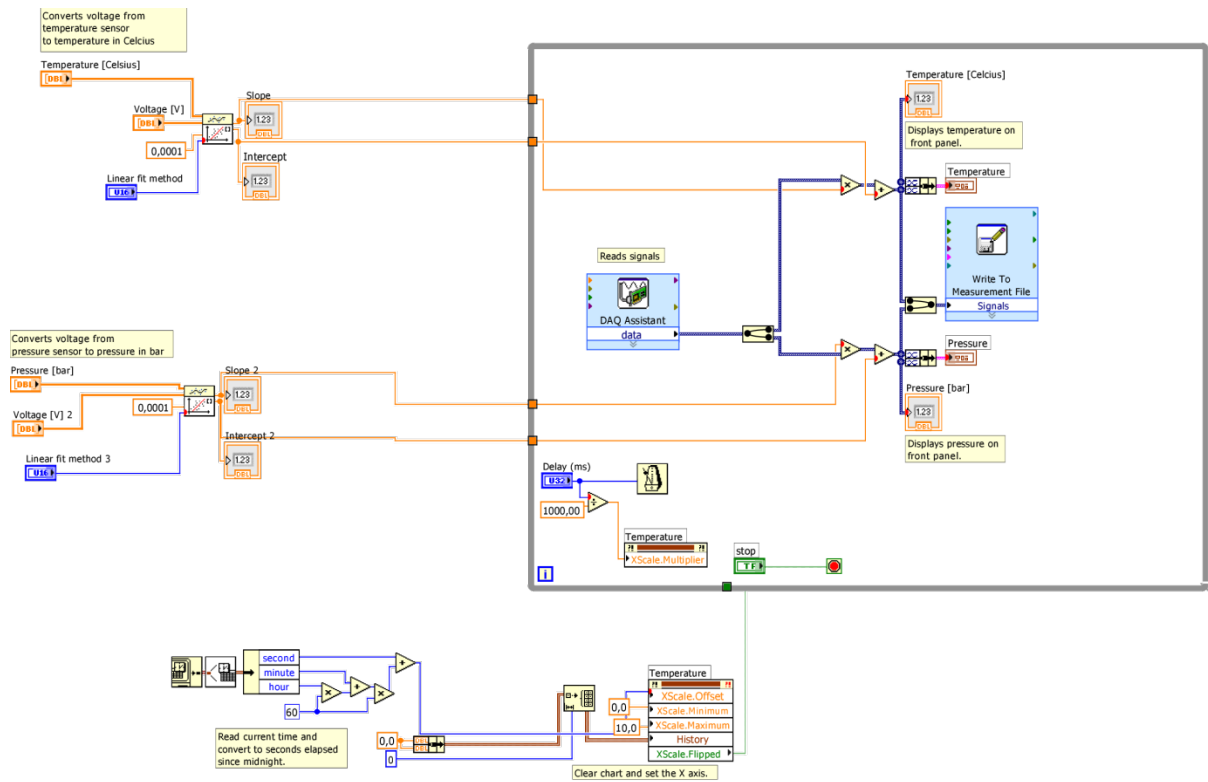


Figure B.13: Block diagram of the logging program utilized to acquire data from hydrate experiments.



### **B.3.3 Summarized procedure**

1. Start the computer. Administrator login information is written on a note taped to the computer cabinet.
2. Open LabVIEW. Open “MeasurementsOle” from the pop up menu of last used VI’s. The VI is saved in the following directory: D:\LABVIEW\Ole\MeasurementsOle.vi
3. The front panel of the VI should now be open. If the graphs contain data from previous experiments, right click the graph(s), select data operations, and clear the charts.
4. Set the desired sampling rate.
5. Open the block diagram by selecting Window, and Show Block Diagram.
6. Double click the Write to Measurements File VI. Select a directory on the hard drive where the data from the experiments are to be stored.
7. Start the VI by clicking the Run Arrow.
8. Inject gas.
9. Assuming full experimental run, and dissociation of hydrates. Stop the program by clicking the STOP button in the front panel. It may take some time before the VI stops running, and you may have to click the STOP button more than one time. Do not click the Abort Execution button.
10. Copy the saved .lvm file to a USB disk and transfer it to your computer.
11. The .lvm file may be renamed .txt and subsequently be read by MATLAB/Excel.

## REFERENCES

- [1] Kvenvolden, K.A., and Claypool G. E., *Gas Hydrates in Oceanic Sediment*, in *U.S. Geological Survey*. 1988.
- [2] IEA, *World Energy Outlook*. International Energy Agency. 2013.
- [3] Graue, A., et al., *Methane Production from Natural Gas Hydrates by CO<sub>2</sub> Replacement - Review of Lab Experiments and Field Trial*, in *SPE Bergen One Day Seminar*. 2014, Society of Petroleum Engineers.
- [4] Sloan, E.D. and C. Koh, *Clathrate Hydrates of Natural Gases*. 3 ed. 2008: CRC Press.
- [5] Ebinuma, T., *Method for dumping and disposing of carbon dioxide gas and apparatus therefor*. 1993.
- [6] NETL. *Ignik Skumi Gas Hydrate Field Trial*. 2012; Available from: [http://www.netl.doe.gov/research/oil-and-gas/methane-hydrates/co2\\_ch4exchange](http://www.netl.doe.gov/research/oil-and-gas/methane-hydrates/co2_ch4exchange).
- [7] Forskningsrådet. *Hydrates in petroleum production - Assessment of Plug Risk*. 2005; Available from: <http://www.forskningsradet.no/servlet/Satellite?c=Prosjekt&cid=1193731605922&pageName=ForskningsradetNorsk/Hovedsidemal&p=1181730334233>.
- [8] Talatori, S., *Kinetics of gas hydrate formation in the presence of crude oil*. 2009, University of Bergen.
- [9] Vaular, E., *Origin and character of gaseous hydrocarbons in the hydrate and non-hydrate charged sediments on the Norway - Svalbard margins* . 2011, University of Bergen.
- [10] Corak, D., *Physiochemical evaluation of gas hydrate formation for water desalination – formation rates, hydrate amounts and heats of crystallization*. . 2011, University of Bergen.
- [11] Calsep, *PVTsim*.
- [12] HWU. *What are gas hydrates?* Herriot-Watt University: Center for Gas Hydrate Research; Available from: [http://www.pet.hw.ac.uk/research/hydrate/images/hydrates/structures\\_large.jpg](http://www.pet.hw.ac.uk/research/hydrate/images/hydrates/structures_large.jpg).
- [13] Hester, K., Brewer, P. G., *Clathrate Hydrates in Nature*. Annual Reviews of Marine Science, 2009. 1: p. 303-327.
- [14] Franks, F., *Water: A Matrix of Life*. 2 ed. 2000: RSC Press.

- [15] Circone, S., et al., *CO<sub>2</sub> Hydrate: Synthesis, Composition, Structure, Dissociation Behavior, and a Comparison to Structure I CH<sub>4</sub> Hydrate*. Journal of Physical Chemistry B, 2003. **107**(23): p. 5529 - 5539.
- [16] Circone, S., Kirby, S. H., and L.A. Stern, *Direct Measurement of Methane Hydrate Composition along the Hydrate Equilibrium Boundary*. Journal of Physical Chemistry B, 2005. **109**(19): p. 9468-9475.
- [17] Janda, K.C. *Methane/Propane Double Hydrate*. Available from: <http://ps.uci.edu/scholar/kcjanda/research/methanepropane-double-hydrate>.
- [18] Atkins, P. and J. De Paula, *Physical Chemistry*. 9 ed. 2010: Oxford University Press.
- [19] Sloan, E.D., C. Koh, and A. Sum, *Natural Gas Hydrates in Flow Assurance*. 2010: Gulf Professional Publishing.
- [20] PetroWiki. *Preventing formation of hydrate plugs*. Available from: [http://petrowiki.spe.org/Preventing\\_formation\\_of\\_hydrate\\_plugs](http://petrowiki.spe.org/Preventing_formation_of_hydrate_plugs).
- [21] Mullin, J.W., Raven, K. D., *Nucleation in Agitated Solutions*. Nature, 1961. **190**: p. 251.
- [22] Speight, J.G., *Natural Gas: A Basic Handbook*. 2007: Gulf Publ. Company.
- [23] Speight, J.G., *The Chemistry and Technology of Coal*. 3 ed. 2013: CRC Press.
- [24] Ellis, H. and R.D. Harrison, *Book of data*. 1984, Harlow: Longman.
- [25] Max, M.D., A.H. Johnson, and W.P. Dillon, *Economic Geology of Natural Gas Hydrate*. Coastal Systems and Continental Margins. 2006: Springer.
- [26] Kvenvolden, K.A., *Gas hydrates—geological perspective and global change*. Reviews of Geophysics, 1993. **31**(2): p. 173-187.
- [27] Boswell, R. and T. Collett, *The Gas Hydrates Resource Pyramid*. Fire in the Ice Newsletter, 2006. **6**: p. 5-7.
- [28] U.S. Department of Energy NETL, *Japan completes first offshore methane hydrate production test...* Fire in the Ice Newsletter, 2013. **13**(2): p. 1.
- [29] Yamamoto, K., *Methane Hydrate Bearing Sediments: A New Subject of Geomechanics*, in *International Association for Computer Methods and Advances in Geomechanics (IACMAG)*. 2008: Goa, India.
- [30] Hyodo, M., et al., *A comparative analysis of the mechanical behavior of carbon dioxide and methane hydrate-bearing sediments*. American Mineralogist, 2014. **99**(1): p. 178-183.

- [31] Nago, A. and A. Nieto, *Natural Gas Production from Methane Hydrate Deposits Using CO<sub>2</sub> Clathrate Sequestration: State-of-the-Art Review and New Technical Approaches*. Journal of Geological Research, 2011. **2011**.
- [32] Schicks, J.M., M. Luzi, and B. Beeskow-Strauch, *The Conversion Process of Hydrocarbon Hydrates into CO<sub>2</sub> Hydrates and Vice Versa: Thermodynamic Considerations*. The Journal of Physical Chemistry A, 2011. **115**(46): p. 13324-13331.
- [33] Lee, H., et al., *Recovering Methane from Solid Methane Hydrate with Carbon Dioxide*. Angewandte Chemie International Edition, 2003. **42**(41): p. 5048-5051.
- [34] Ota, M., et al., *Replacement of CH<sub>4</sub> in the hydrate by use of liquid CO<sub>2</sub>*. Energy Conversion and Management, 2005. **46**(11-12): p. 1680-1691.
- [35] *SketchUp*. 2013, Trimble Navigation.
- [36] Sandrock, C. *Ternplot*. 2007; Available from: <http://www.mathworks.com/matlabcentral/fileexchange/2299-ternplot>.
- [37] Unruh, C.H. and D.L. Katz, *Gas Hydrates of Carbon Dioxide-Methane Mixtures*. Journal of Petroleum Technology, 1949. **1**(04): p. 83-86.
- [38] Adisasmito, S., R.J. Frank, and E.D. Sloan, *Hydrates of carbon dioxide and methane mixtures*. Journal of Chemical & Engineering Data, 1991. **36**(1): p. 68-71.
- [39] Dholabhai, P.D. and P.R. Bishnoi, *Hydrate equilibrium conditions in aqueous electrolyte solutions: Mixtures of methane and carbon dioxide*. Journal of Chemical and Engineering Data, 1994. **39**(1).
- [40] Ohgaki, K., et al., *Methane Exploitation by Carbon Dioxide from Gas Hydrates. Phase Equilibria for CO<sub>2</sub>-CH<sub>4</sub> Mixed Hydrate System*. Journal of Chemical Engineering of Japan, 1996. **29**(3): p. 478-483.
- [41] Servio, P., et al., *Gas hydrate phase equilibrium in the system methane-carbon dioxide-neohexane and water*. Fluid Phase Equilibria, 1999. **158**: p. 795-800.
- [42] Fan, S.-s. and T.-m. Guo, *Hydrate Formation of CO<sub>2</sub>-Rich Binary and Quaternary Gas Mixtures in Aqueous Sodium Chloride Solutions*. Journal of Chemical & Engineering Data, 1999. **44**(4): p. 829-832.
- [43] Seo, Y.-t., H. Lee, and J.-h. Yoon, *Hydrate Phase Equilibria of the Carbon Dioxide, Methane, and Water System*. Journal of Chemical & Engineering Data, 2001. **46**(2): p. 381-384.
- [44] Yu-Taek, S. and L. Huen, *Multiple-phase hydrate equilibria of the ternary carbon dioxide, methane, and water mixtures*. Journal of Physical Chemistry B, 2001. **105**(41): p. 10084.

- [45] Beltrán, J.G. and P. Servio, *Equilibrium Studies for the System Methane + Carbon Dioxide + Neohexane + Water*. Journal of Chemical & Engineering Data, 2008. **53**(8): p. 1745-1749.
- [46] Bruusgaard, H., J.G. Beltrán, and P. Servio, *Solubility measurements for the CH<sub>4</sub> + CO<sub>2</sub> + H<sub>2</sub>O system under hydrate–liquid–vapor equilibrium*. Fluid Phase Equilibria, 2010. **296**(2): p. 106-109.
- [47] Belandria, V., A.H. Mohammadi, and D. Richon, *Phase equilibria of clathrate hydrates of methane + carbon dioxide: New experimental data and predictions*. Fluid Phase Equilibria, 2010. **296**(1): p. 60-65.
- [48] Belandria, V., et al., *Compositional Analysis and Hydrate Dissociation Conditions Measurements for Carbon Dioxide + Methane + Water System*. Industrial & Engineering Chemistry Research, 2011. **50**(9): p. 5783-5794.
- [49] Herri, J.M., et al., *Gas hydrate equilibria for CO<sub>2</sub>–N<sub>2</sub> and CO<sub>2</sub>–CH<sub>4</sub> gas mixtures—Experimental studies and thermodynamic modelling*. Fluid Phase Equilibria, 2011. **301**(2): p. 171-190.
- [50] Bi, Y., T. Yang, and K. Guo, *Determination of the upper-quadruple-phase equilibrium region for carbon dioxide and methane mixed gas hydrates*. Journal of Petroleum Science and Engineering, 2013. **101**: p. 62-67.
- [51] Berez, E. and M. Balla-Achs, *Gas Hydrates*. Studies in Inorganic Chemistry. 1983: Elsevier.
- [52] Seo, Y. and H. Lee, *Hydrate Phase Equilibria of the Ternary CH<sub>4</sub> + NaCl + Water, CO<sub>2</sub> + NaCl + Water and CH<sub>4</sub> + CO<sub>2</sub> + Water Mixtures in Silica Gel Pores*. The Journal of Physical Chemistry B, 2002. **107**(3): p. 889-894.
- [53] Akihiro, H., et al., *Formation and Dissociation Processes of Gas Hydrate Composed of Methane and Carbon Dioxide below Freezing*. Ocean and Polar Research, 2004: p. 515-521.
- [54] Calsep. *PVTsim method documentation*.
- [55] Calsep. *References*. Available from: <http://www.pvtsim.com/reference-list.aspx>.
- [56] Pedersen, K.S., Christensen, P. L., *Phase Behavior of Petroleum Reservoir Fluids*. 2007: CRC Press.
- [57] Munck, J., S. Skjold-Jørgensen, and P. Rasmussen, *Computations of the formation of gas hydrates*. Chemical Engineering Science, 1988. **43**(10): p. 2661-2672.
- [58] Calsep, *Hydrate predictions in PVTsim (Peng-Robinson Equation of State)*. 2012.
- [59] McCain, W.D., *The Properties of Petroleum Fluids*. 2 ed. 1990: PennWell Books.

- [60] Maron, S.H., *Principles of physical chemistry*, ed. C.F. Prutton. 1965, New York: Macmillan.
- [61] Abbot, S. *Phase Diagram Explorer*. 2013; Available from: <http://www.stevenabbott.co.uk/PracticalSurfactants/PDE.html>.
- [62] PetroWiki. *Ternary phase diagrams*. Available from: [http://petrowiki.org/Ternary\\_phase\\_diagrams](http://petrowiki.org/Ternary_phase_diagrams).
- [63] *Termaks Series 6000 Manual*. Available from: <http://www.geminibv.nl/labware/termaks-kbp6395ll-koelbroedstoof/termaks-kbp-6000-manual.pdf>.
- [64] Genov, G., *Personal Communication*. 2013.
- [65] *1/4, 1/8 and 1/16 DIN Plus Series Controllers & Indicators User Guide*. 2006, West Control Solutions.
- [66] *UPR700 Microprocessor-Based Pressure/Process Indicator Installation and Operation Manual*. Dynisco.
- [67] *LabVIEW*. 2013, National Instruments.
- [68] *Getting started with LabVIEW*. 2006, National Instruments.
- [69] Halvorsen, H.-P., *Introduction to LabVIEW*. 2012, Telemark University College.
- [70] Holman, J.P., *Experimental Methods for Engineers*. 8 ed. 2012: McGraw-Hill.
- [71] Gasson, J.R., *Gasphase GC HP 6890+ manual*. 2013.
- [72] *Chromeleon Chromatography Data System*. Thermo Scientific Dionex.
- [73] Fadnes, F.H., *Natural hydrate inhibiting components in crude oils*. Fluid Phase Equilibria, 1996. **117**(1–2): p. 186-192.
- [74] Fotland, P. and K.M. Askvik, *Some aspects of hydrate formation and wetting*. Journal of Colloid and Interface Science, 2008. **321**(1): p. 130-141.
- [75] Hester, K.C. and E.D. Sloan, *sII Structural Transitions from Binary Mixtures of Simple sI Formers*. International Journal of Thermophysics, 2005. **26**(1): p. 95-106.
- [76] Rovetto, L.J., et al., *NMR studies on CH<sub>4</sub>+CO<sub>2</sub> binary gas hydrates dissociation behavior*. Proceedings of the 6th International Conference on Gas Hydrates. 2008.
- [77] Lee, S., et al., *Thermodynamic and <sup>13</sup>C NMR spectroscopic verification of methane-carbon dioxide replacement in natural gas hydrates*. Chemical Engineering Journal, 2013. **225**: p. 636-640.
- [78] Schicks, J.M. and M. Luzi-Helbing, *Cage occupancy and structural changes during hydrate formation from initial stages to resulting hydrate phase*. Spectrochim Acta A Mol Biomol Spectrosc, 2013. **115**: p. 528-36.

- [79] Uchida, T., et al., *Kinetics and Stability of CH<sub>4</sub>–CO<sub>2</sub> Mixed Gas Hydrates during Formation and Long-Term Storage*. ChemPhysChem, 2005. **6**(4): p. 646-654.
- [80] Li, H. and J. Yan, *Evaluating cubic equations of state for calculation of vapor–liquid equilibrium of CO<sub>2</sub> and CO<sub>2</sub>-mixtures for CO<sub>2</sub> capture and storage processes*. Applied Energy, 2009. **86**(6): p. 826-836.
- [81] Diamantonis, N.I., et al., *Evaluation of Cubic, SAFT, and PC-SAFT Equations of State for the Vapor–Liquid Equilibrium Modeling of CO<sub>2</sub> Mixtures with Other Gases*. Industrial & Engineering Chemistry Research, 2013. **52**(10): p. 3933-3942.
- [82] Ballard, L. and E.D. Sloan, *The next generation of hydrate prediction IV: A comparison of available hydrate prediction programs*. Fluid Phase Equilibria, 2004. **216**(2): p. 257-270.
- [83] Calsep. *PVTsim from 21.2 to Nova 1*. 2014; Available from: <http://www.pvtsimnova.com/news/15/105/PVTsim-from-21-2-to-Nova-1.html>.
- [84] Hachikubo, A., et al. *Phase Equilibrium Studies on Gas Hydrates Formed from Various Guest Molecules and Powder Ice*. in *Proceedings in the Fourth International Conference on Gas Hydrates*. 2002. Yokohama, Japan.
- [85] Zeebe, R.E., Wolf-Gladrow. D., *CO<sub>2</sub> in Seawater: Equilibrium, Kinetics, Isotopes*. 1 ed. Elsevier Oceanography Series. 2001: Elsevier.
- [86] Tohidi, B., et al., *Improving the Accuracy of Gas Hydrate Dissociation Point Measurements*. Annals of the New York Academy of Sciences, 2000. **912**(1): p. 924-931.
- [87] Gjertsen, L.H. and F.H. Fadnes, *Measurements and Predictions of Hydrate Equilibrium Conditions*. Annals of the New York Academy of Sciences, 2000. **912**(1): p. 722-734.
- [88] Siemens. *MICROMASTER Vector Operating Instructions*. 1999; Available from: [http://cache.automation.siemens.com/dnl/TUxNzU3AAAA\\_16749533\\_HB/1751-U529-E\\_engl.pdf](http://cache.automation.siemens.com/dnl/TUxNzU3AAAA_16749533_HB/1751-U529-E_engl.pdf).